Low-pressure closed-loop MEMS accelerometers for automotive applications
Vasco António Lourenço Lima
UMinho | 2020

Universidade do Minho
Escola de Engenharia

Vasco António Lourenço Lima

Low-pressure closed-loop MEMS accelerometers for automotive applications

junho de 2020

CIÊNCIA, TECNOLOGIA E ENSINO SUPERIOR

FCT Fundação para a Ciência e a Tecnologia

NORTE2020 CENTRO2020 ALENTEJO 2020 POCH PORTUGAL 2020

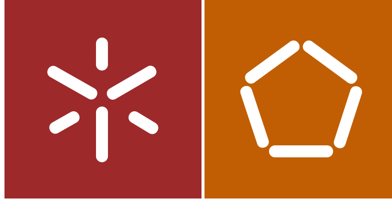

Universidade do Minho
Escola de Engenharia

Vasco António Lourenço Lima

Low-pressure closed-loop MEMS accelerometers for automotive applications

Tese de Doutoramento
Programa Doutoral em Sistemas Avançados de Engenharia para a Indústria

Trabalho efetuado sobre a orientação de
Professor Doutor Jorge Miguel Nunes dos Santos Cabral
Professor Doutor João Carlos Azevedo Gaspar
Professor Doutor Luís Alexandre Machado da Rocha (à memória de)

junho de 2020

DIREITOS DE AUTOR E CONDIÇÕES DE UTILIZAÇÃO DO TRABALHO POR TERCEIROS

Este é um trabalho académico que pode ser utilizado por terceiros desde que respeitadas as regras e boas práticas internacionalmente aceites, no que concerne aos direitos de autor e direitos conexos.

Assim, o presente trabalho pode ser utilizado nos termos previstos na licença abaixo indicada.

Caso o utilizador necessite de permissão para poder fazer um uso do trabalho em condições não previstas no licenciamento indicado, deverá contactar o autor, através do RepositóriUM da Universidade do Minho.

Atribuição-NãoComercial-SemDerivações
CC BY-NC-ND

https://creativecommons.org/licenses/by-nc-nd/4.0/

ACKNOWLEDGMENTS

During these past four years I was lucky to expand my knowledge and develop this work. However, this would not be possible without a vast group of people. To everyone that contributed to this accomplishment I would like to sincerely express my gratitude. Yet, several people deserve a special mention.

I must start by thanking my supervisor, the late Prof. Luís Alexandre Rocha, without whom I would never have worked on MEMS or even pursue an academic career. It was a true privilege to work alongside such a knowledgeable and thoughtful person. He will continue to inspire me in my future journeys. I would also like to express my gratitude to Professor Jorge Cabral for supervising this work, reviewing the thesis, and for always believing in me. To Dr. João Gaspar, who welcomed me at INL and accepted to supervise this work, my thanks.

My appreciation is also towards Burkhard Kuhlmann, from Bosch Automotive Electronics, who always was available to meet and discuss this work. This extends to his team, for their interest, feedback, and good times in Reutlingen.

I am grateful to my work colleagues, Eurico Moreira, Filipe Alves, Carlos Ferreira, Rui Machado, Fábio Leitão, Nuno Brito, Carlos Silva, Andreia Faria, Pedro Macedo, and Inês Garcia (to name a few), many of which I consider my friends, for the collaboration, discussions and enjoyable moments. I also want to thank my friends, that during all these years have been there to support me.

My special thanks to Ana Gomes, for the unconditional support, complicity, companionship, and the many laughs.

I would also like to acknowledge everyone that dispended time to help me revise this thesis.

Como não poderia deixar de ser, o meu maior obrigado vai para a minha família. Aos meus pais, António Lima e Teresa Lima, que sempre me apoiaram e tudo fizeram para que aqui chegasse, o meu muito obrigado. Obrigado também à minha irmã Joana e ao Fábio.

This thesis was supported by FCT– Fundação para a Ciência e Tecnologia through the grant PDE/BDE/114563/2016.

Vasco Lima
March 29th, 2020

STATEMENT OF INTEGRITY

I hereby declare having conducted this academic work with integrity. I confirm that I have not used plagiarism or any form of undue use of information or falsification of results along the process leading to its elaboration.

I further declare that I have fully acknowledged the Code of Ethical Conduct of the University of Minho.

RESUMO

As atuais tendências na indústria automóvel são a automação e a eletrificação. Atualmente, um veículo tem cerca de cem sensores, dos quais no mínimo trinta usam tecnologia MEMS, fazendo um valor anual de mercado de 11 mil milhões de dólares americanos. Um elevado número destes dispositivos são sensores inerciais, representando um valor anual de mercado de 1.6 mil milhões de dólares americanos.

Aplicações inerciais típicas, tais como unidades de medição inerciais, necessitam de mais de um tipo destes sensores, como por exemplo acelerómetros e giroscópios. Contudo, giroscópios MEMS baseados na força de Coriolis necessitam de operar em vácuo, enquanto os acelerómetros são tipicamente operados à pressão atmosférica. Assim, o encapsulamento em vácuo de acelerómetros MEMS pode ser vantajoso, uma vez que possibilita a integração num substrato comum de silício com outros sensores MEMS inerciais, levando a reduções de tamanho e de custo de fabrico e encapsulamento. No entanto, o alto fator de qualidade resultante do encapsulamento em vácuo dificulta a operação do acelerómetro.

Moduladores sigma-delta eletromecânicos fornecem o amortecimento elétrico necessário para operar acelerómetros em vácuo, enquanto providenciam alta resolução e linearidade, e baixa dependência térmica e suscetibilidade ao processo de fabrico, sendo um dos métodos mais atrativos para alcançar sensores MEMS inerciais de alta performance. Acelerómetros MEMS encapsulados em vácuo que usam modulação sigma-delta podem ser encontrados na literatura, mas todos têm um problema comum: uma massa sísmica grande. Isto tem diversas desvantagens, tais como gama dinâmica reduzida, aumento da complexidade do processo de fabrico e limitações na integração, levando ao aumento do custo.

Nesta tese é apresentado um acelerómetro MEMS com tamanho reduzido, encapsulado em vácuo e operado com um modulador sigma-delta. O modulador sigma-delta foi implementado em FPGA, permitindo a sintonização rápida e eficaz dos seus parâmetros para os dispositivos finais. Isto visa alcançar a estabilidade do sistema (mais difícil em vácuo) e melhorar a performance do sensor.

O acelerómetro realizado alcançou um ruido de 173 $\mu g/\sqrt{Hz}$, uma largura de banda de 400 Hz, um intervalo de medição de ±5 g e uma não linearidade inferior a 0.66 %. Valores mais baixos de ruído (123 $\mu g/\sqrt{Hz}$) foram obtidos à custa de um menor intervalo de medição (±1.5 g), atestando a flexibilidade do sistema. No conhecimento do autor, este trabalho apresenta a melhor relação entre ruido, tamanho e largura de banda, quando comparando com dispositivos idênticos apresentados na literatura até à data.

Palavras-chave: acelerómetro; encapsulamento a vácuo; MEMS; modulação sigma-delta.

ABSTRACT

The current trends in the automotive industry are automation and electrification. Nowadays, a typical vehicle has around one hundred sensors, from which at least thirty use MEMS technology, amounting to an annual market value of 11 billion US dollars. A large number of these devices are inertial sensors, representing an annual market value of 1.6 billion US dollars.

Typical inertial applications, like inertial measurement units (IMU), require more than one type of inertial sensor, such as accelerometers and gyroscopes. Yet, MEMS gyroscopes based on the Coriolis force must operate in low-pressure, while accelerometers are typically operated at atmospheric pressure since they must be critically damped. Thus, vacuum encapsulation of MEMS accelerometers can be advantageous since it enables integration in a single common silicon substrate with other MEMS inertial sensors, leading to size reduction and to a decrease in fabrication and packaging costs. However, the high quality factor resultant from vacuum encapsulation causes undesirable high settling times for accelerometers.

Electromechanical sigma-delta modulators can provide the electrical damping necessary for low-pressure accelerometers while delivering high resolution and linearity, and low thermal dependency and susceptibility to process variations, representing one of the most attractive architectures for achieving high-performance MEMS inertial sensors. Vacuum encapsulated MEMS accelerometers using sigma-delta modulation can be found in the literature, but all present a common issue: large proof-mass. This has several drawbacks, such as reduced full-scale, added complexity of the manufacturing process, and integration limitations, ultimately leading to cost increase.

In this thesis, a small-size and low-pressure MEMS accelerometer operated in a closed-loop sigma-delta modulator is presented. The sigma-delta modulator loop was digitally implemented in a FPGA, enabling a fast and accurate tuning of the loop parameters at the final trim of the devices. This aims to achieve loop stability, more difficult for low-damping devices, and to improve the sensor overall performance.

The implemented accelerometer achieved a noise figure of 173 µg/√Hz, for a bandwidth of 400 Hz, a measurement range of at least ±5 g, and a nonlinearity lower than 0.66 %. Lower noise values (123 µg/√Hz) are also attainable at the expense of lower dynamic range (±1.5 g), verifying the flexibility of the accelerometer. To the best of the author's knowledge, this work shows the best relation between noise, device size, and bandwidth, when comparing similar devices presented in the literature to date.

Keywords: accelerometer; MEMS; sigma-delta modulation; vacuum encapsulation.

INDEX

Acknowledgments iii
Resumo v
Abstract vi
1. Introduction 1
1.1. Microelectromechanical systems 2
1.1.1. MEMS in the automotive industry 2
1.2. Accelerometers 3
1.2.1. Traditional versus MEMS accelerometers 5
1.2.2. Microfabrication processes 6
1.2.3. Vacuum encapsulation 8
1.2.4. Closed-loop operation 9
1.3. State-of-the-art 10
1.4. Motivation and goals 14
1.5. Organization of the thesis 15
References 16
2. Electromechanical sigma-delta modulator 23
2.1. One degree of freedom MEMS device 24
2.1.1. Low-pressure model 27
2.1.2. Differential operation 28
2.2. Closed-loop operation 29
2.2.1. Sigma-delta modulation 31
2.2.2. Electromechanical sigma-delta modulation 35
2.3. Nonlinearities 39
2.3.1. Pull-in effect 41
2.3.2. Temperature dependence 42
2.4. Conclusions 43
References 44
3. Integrated system implementation 47
3.1. High-level simulation model 48
3.2. MEMS sensor 51
3.2.1. Microfabrication process 53
3.2.2. Microfabricated devices 54
3.3. Analog circuit 56
3.3.1. Capacitive to voltage converter 57
3.3.2. Signal acquisition 60
3.3.3. Electrostatic force voltage 61

3.4. FPFA programable logic ... 62
3.4.1. Control and acquisition of the ADC data ... 63
3.4.2. Low-pass filter ... 63
3.4.3. Phase compensator ... 65
3.4.4. Higher-order modulator loop ... 66
3.4.5. Quantizer ... 67
3.4.6. Decimation filter ... 67
3.5. FPGA processing system - software application ... 68
3.6. Conclusions ... 70
References ... 70
4. Sensor characterization ... 73
4.1. Mechanical characterization of the MEMS accelerometer ... 74
4.2. Overall accelerometer system characterization ... 76
4.2.1. Experimental setups ... 76
4.2.2. High-order loop gains ... 78
4.2.3. Sensitivity and nonlinearity ... 79
4.2.4. Noise figure ... 80
4.2.5. Cross-axis sensitivity ... 81
4.2.6. Temperature dependency ... 82
4.2.7. Frequency response ... 86
4.2.8. Vibration robustness ... 87
4.3. Low-noise optimization ... 88
4.3.1. Long-term stability ... 89
4.4. Conclusions ... 90
References ... 91
5. Conclusions and future work ... 93
5.1. Conclusions ... 94
5.2. Future work ... 99
References ... 100
Annex A: Analog circuit schematics ... 102
Annex B: Analog circuit PCB layers ... 103
Annex C: FPGA block diagram ... 104
Annex D: IIR block diagram ... 105
Annex E: Phase compensator block diagram ... 106
Annex F: High-order loop block diagram ... 107
List of publications ... 108
About the author ... 109

INDEX OF FIGURES

Figure 1.1: Simplified diagram of an acceleration sensor. 4
Figure 1.2: Typical surface micromachining process. 7
Figure 1.3: Typical bulk micromachining process using a SOI wafer.................... 8
Figure 1.4: Electromechanical sigma-delta modulator architecture proposed by F. Chen et al............. 11
Figure 1.5: Sensor proposed by H. Xu et al. [1.36]. 12
Figure 2.1: Schematic of a capacitive MEMS accelerometer with one degree of freedom.................... 24
Figure 2.2: System Bode plot for different quality factors. 26
Figure 2.3: System step response for different quality factors. 27
Figure 2.4: Plates architecture. 27
Figure 2.5: Schematic of an ideal differential capacitive MEMS accelerometer. 29
Figure 2.6: Schematic of an ideal differential capacitive MEMS accelerometer with electrostatic actuation. 30
Figure 2.7: Oversampling effects on the quantization noise power density.................... 31
Figure 2.8: Noise shaping of low frequency noise to high frequencies. 32
Figure 2.9: Generic model of sigma-delta noise shaping loop. 32
Figure 2.10: a) Block diagram of a sigma-delta modulator used as an ADC; b) Z-domain linear model of a sigma-delta modulator used as an ADC. 33
Figure 2.11: a) Block diagram of a second-order sigma-delta modulator used as an ADC; b) Z-domain linear model of a second-order sigma-delta modulator used as an ADC.................... 35
Figure 2.12: Generic block diagram of an electromechanical sigma-delta modulator. 35
Figure 2.13: Model of a second-order electromechanical sigma-delta modulator. 37
Figure 2.14: Model of a third-order electromechanical sigma-delta modulator with cascade integrator with distributed feedback architecture. 38
Figure 2.15: Relation between capacitance and proof-mass displacement.................... 40
Figure 2.16: Relation between electrostatic force and proof-mass displacement. 40
Figure 2.17: Relation between the damping coefficient and proof-mass displacement. 41
Figure 2.18: Representation of the pull-in phenomenon. 42
Figure 2.19: Parallel-plate dimensions changing with thermal expansion.................... 42
Figure 3.1: Block diagram of the system. 48
Figure 3.2: Simulink model of the electromechanical sigma-delta modulator. 49
Figure 3.3: Simulink model of the MEMS accelerometer. 50
Figure 3.4: Simulink model of the readout circuit. 50
Figure 3.5: Simulink model of the decimation filter. 51
Figure 3.6: Simulink model of the 1-bit DAC. 51
Figure 3.7: CAD layout of the designed MEMS accelerometer. 52
Figure 3.8: FEA structural simulation of the movable part of the sensor element. 52
Figure 3.9: Working principle of Bosch's DRIE process, based on [3.17]. 53
Figure 3.10. SEM images of the microfabricated MEMS accelerometer. 55

Figure 3.11: MEMS sensor in a CLCC-44 package. 56
Figure 3.12: Simplified schematic of the analog circuit implementing the readout circuit and the one-bit DAC. 57
Figure 3.13: Implemented PCB, including the MEMS sensor, the C/V ASIC, the readout circuit, and the one-bit DAC. 57
Figure 3.14: Sensing capacitance variation with proof-mass displacement. 58
Figure 3.15: Fully differential switched capacitor capacitance to voltage converter [3.10]. a) Schematic; b) Control clock signals. 58
Figure 3.16: a) SEM picture of the fabricated ASIC. b) C/V ASIC in a DIP-24 chip carrier. 59
Figure 3.17: Capacitance to voltage converter output as a function of the sensed differential capacitance. 59
Figure 3.18: ADS5560 functional block diagram [3.20]. 60
Figure 3.19: ZedBoard development board. 62
Figure 3.20: Block diagram of the implemented FPGA architecture. 63
Figure 3.21: Second-order stage of the implemented discrete-time IIR filter. 64
Figure 3.22: Bode plot of the implemented low-pass filter. 64
Figure 3.23: Implemented phase compensator. 65
Figure 3.24: Bode plot of the implemented phase compensator. 66
Figure 3.25: Block diagram of the high-order loop. 66
Figure 3.26: Bode plot of the implemented low-pass filter. 67
Figure 3.27: Software flowcharts. a) Thread “main”; b) Thread “run”. 69
Figure 4.1: Bode plot of the three tested devices. 74
Figure 4.2: Pull-in voltage measurement. 75
Figure 4.3: Experimental setup used to measure the sensitivity and nonlinearity of the accelerometer. 77
Figure 4.4: Experimental setup used to measure the frequency response of the accelerometer. 77
Figure 4.5: Optimization of phase compensator parameters. 78
Figure 4.6: Experimental and simulated sensitivity and nonlinearity results. 79
Figure 4.7: Experimental and simulated Allan deviation measurements. 80
Figure 4.8: Comparison of the raw acceleration values between open-loop and closed-loop configurations. 81
Figure 4.9: Experimental cross-axis sensitivity measurements. 82
Figure 4.10: Temperature coefficient measurements for approximately 0 g acceleration. 83
Figure 4.11: Temperature coefficient measurements for approximately 1 g acceleration. 84
Figure 4.12: Compensation of the temperature effects. 85
Figure 4.13: Frequency response of the accelerometer. 87
Figure 4.14: Experimental and simulated results of the vibration robustness test. 88
Figure 4.15: Allan deviation measurements for the low-noise optimization. 89
Figure 4.16: Long-term measurement results. 90

INDEX OF TABLES

Table 1.1: Acceleration sensor application grades [1.41]. 5
Table 1.2: State-of-the-art comparison of vacuum encapsulated MEMS accelerometers using sigma-delta modulation. 13
Table 3.1: Main design parameters of the fabricated device. 56
Table 3.2: Capacitor values to define the capacitance to voltage converter gain. 59
Table 3.3: Filter coefficients of the readout IIR filter for a cutoff frequency of 80 kHz. 64
Table 3.4: Phase compensator coefficients. 65
Table 3.5: Filter coefficients of the decimation IIR filter for a cutoff frequency of 400 Hz. 67
Table 4.1: Theoretical and experimental values of the resonant frequency and quality factor. 75
Table 4.2: Theoretical and experimentally measured nominal pull-in voltage. 76
Table 4.3: Cross-axis sensitivity calculations. 82
Table 4.4: Temperature dependency of the sensitivity of the accelerometer. 86
Table 5.1: Comparison of the research objectives with the achieved performance. 96
Table 5.2: Comparison of this work to the state-of-the-art. 98
Table 5.3: Device size comparison. 98

LIST OF ABBREVIATIONS AND ACRONYMS

1-DOF	One Degree Of Freedom
ABS	Anti-lock Brake System
ADC	Analog-to-Digital Converter
ASIC	Application Specific Integrated Circuit
AXI	Advanced eXtensible Interface
BOX	Buried OXide
CAD	Computer Aided Design
CCLD	Constant Charge Line Drive
CMOS	Complementary Metal-Oxide-Semiconductor
DAC	Digital-to-Analog Converter
DRIO	Deep Reactive Ion Etch
EMΣΔM	ElectroMechanical Sigma-Delta Modulator
ESA	European Space Agency
FEA	Finite Element Analysis
FOM	Figure Of Merit
FPGA	Field-Programmable Gate Array
FS	Full-Scale
GPS	Global Positioning System
IC	Integrated Circuit
IIR	Infinite Impulse Response
IMU	Inertial Measurement Unit
MAP	Manifold Air Pressure
MAT	Manifold Air Temperature
MEMS	MicroElectroMechanical System
OSR	OverSampling Ratio
PCB	Printed Circuit Board
PID	Proportional-Integral-Derivative
PL	Programming Logic
PS	Processing System
PSD	Power Spectrum Density
RTOS	Real Time Operating System
SEM	Scanning Electron Microscope
SI	International System of units
SNR	Signal-to-Noise Ratio
SOI	Silicon On Insulator

1. Introduction

Miniaturization has been a key goal of humankind since the beginning of the so-called information age. On December 29, 1959, Richard Feynman presented the now-famous "There's Plenty of Room at the Bottom: An Invitation to Enter a New Field of Physics", where he asked, "*Why cannot we write the entire 24 volumes of the Encyclopedia Britannica on the head of a pin?*" [1.1], laying the foundations to what we know nowadays as micro/nanotechnology. Since those days, the scientific community realized that miniaturizing mechanical parts ("*small but movable machines*" [1.1]), was useful and enabled a growing number of applications, empowering a new engineering field: Microengineering.

Microengineering is the field where multiple physical domains, such as electrical, mechanical, magnetic, optical, thermal, among others, meet each other in the microscale range [1.2]. The genesis of this technology is related to the semiconductor industry, and researchers hoped to obtain the potential benefits of batch fabrication processes and the subsequent cost reduction. Consequently, the invention of the bulk micromachining process occurred in 1956, just eight years after the creation of the transistor [1.2]. One of the first revolutionary devices achieved with this technology was the first resonant gate transistor in 1967 [1.3], integrating the mechanical and electrical physical domains in just one device. Later, in the late 1970's, one of the first commercial products for the consumer market were released, with Hewlett Packard inkjet nozzles [1.4]–[1.6]. Nowadays, the automotive, medical, and aerospace industries started to take advantage of the smaller size, lower cost and high reliability offered by these devices when compared with traditional ones.

1.1. Microelectromechanical systems

The acronym MEMS stands for microelectromechanical systems and it was first introduced in the late 1980s in the United States of America [1.7]. However, the origins of what we now know as MEMS technology can be traced back to 1954, when C. Smith, at the time at the Bell Telephone Laboratories, published the paper “Piezoresistance Effect in Germanium and Silicon” [1.8].

The common definition refers to a system with dimensions between 1 μm and 1 mm that incorporates the electrical and mechanical physical domains. Nevertheless, MEMS can incorporate other domains such as optical, thermal, chemical, among others. For example, microfluidic channels may not have any electrical components [1.9]. Nowadays, the term MEMS has a broader scope and is used to indicate several miniaturized devices that can vary from simple microstructures fabricated on a silicon wafer to complex systems containing sensors, actuators, and electronic circuits [1.7].

Pressure sensors were the first MEMS devices to be economically and technically successful, produced by bulk micromachining, being responsible for a major leap forward in the MEMS field [1.10]. These were based on the piezo-resistive effect to measure the pressure-induced strain on membranes etched from the wafer’s backside [1.2]. Today, alongside bulk acoustic wave filters, microphones, gyroscopes, and accelerometers, they still represent a major percentage of the MEMS devices market share, which by 2015 had become a 10 billion US dollar market with a projected growth rate of 8% [1.11]. The key companies in this field are Texas Instruments (US$616M in 2018), STMicroelectronics (US$776M in 2018), Broadcom (US$1510M in 2018) and Bosch (US$1405M in 2018), and the major application fields are consumer electronics (US$4B in 2015) and automotive (US$2.5B in 2015) [1.12].

1.1.1. MEMS in the automotive industry

Back in 1886, Karl Benz submitted the patent number 37435 for his “vehicle with gas engine operation”, a three-wheeler powered by a rear-mounted single-cylinder four-stroke gas engine that produced 0.75 hp (0.55 kW) [1.13]. Later, in 1908, Henry Ford introduced the Ford Model T, a simple, affordable, and reliable automobile [1.14]. This was the first mass-produced automobile, and the history of the automotive industry as we know it can be traced back to it. In 1979, aiming to reduce tailpipe emissions, and consequently bring vehicles into compliance with environmental regulations, the microprocessor-based automotive engine control module was introduced, to control the engine air-to-fuel ratio. With this came the need for manifold absolute pressure (MAP) and manifold air temperature (MAT) sensors that are used to calculate the density of the air entering the engine. Traditional sensor technologies were able to satisfy

MAP sensor requirements, nonetheless, the low cost and small size of MEMS MAP sensors made them desirable for this application, introducing MEMS devices to the automotive industry in high volume units [1.15]. A similar situation occurred in the mid-1990s when airbag systems were introduced. At first, non-MEMS acceleration sensors were used, however the need for smaller and less expensive devices became apparent, and micromachined accelerometers were able to fulfill this gap [1.15]–[1.17].

In the automotive industry, sensors can be grouped into three main categories: engine management (oil pressure, MAP, MAT, turbo boost, exhaust gas recirculation, etc.), comfort (air conditioning, parking assist, 3D gesture recognition, etc.) and safety (dynamic brake, airbags, pedestrian protection, rollover, etc.). Safety applications always were and will continue to be the pillar of the automotive sensing market, and great improvements were demonstrated in [1.18], where one can see that the traffic density increased with time, but the number of people killed or injured in car accidents is decreasing continuously. These improvements are the result of the enhancement in electronic systems that depend on the input from sensors. Nowadays, a modern vehicle can have around 100 sensors, from which at least 30 are fabricated using MEMS technology, amounting to a market value of US$11 billion of the total US$2.3 trillion of the entire automotive industry [1.19], [1.20]. Regarding sensor manufacturers, Bosch leads with a market value of almost 800 million US dollars, from which inertial sensors amount to approximately half of it.

Inertial sensors play a key role in safety. Accelerometers are used to detect frontal and side impacts triggering the deployment of airbags and can be used to compensate for vibration impacts on other systems. When combined with angular rate sensors, they can be used to prevent undesired vehicle yaw rates, the anti-lock brake system (ABS) and traction control system use their input to prevent loss of vehicle control, and navigational assisted modules use inertial data to assist the calculation of position coordinates when global positioning system (GPS) satellites are out of range [1.21]. These applications make the development and improvement of inertial sensors desirable for the automotive industry, and their market value was 1.6 billion dollars in 2016 [1.19].

1.2. Accelerometers

Accelerometers are devices that measure acceleration forces, which can be static, such as the gravity acceleration, or dynamic, caused by vibrations. The SI (International System of Units) unit for acceleration is m/s^2, however in the accelerometer market and research field g (“gee”) is typically used (1 g = 9.80665 m/s^2 [1.22]).

Acceleration sensors can detect the effect of accelerations in many different ways, however, the majority relies on monitoring the displacement of a proof-mass *(m)*, that is suspended by anchored mechanical springs *(k)*, and the resultant displacement *(x)* is proportional to the applied acceleration *(F)* (Figure 1.1) [1.23]. During the displacement of the proof-mass, a damping force proportional to the velocity is created, and the damping coefficient *(b)* is typically dominated by air damping.

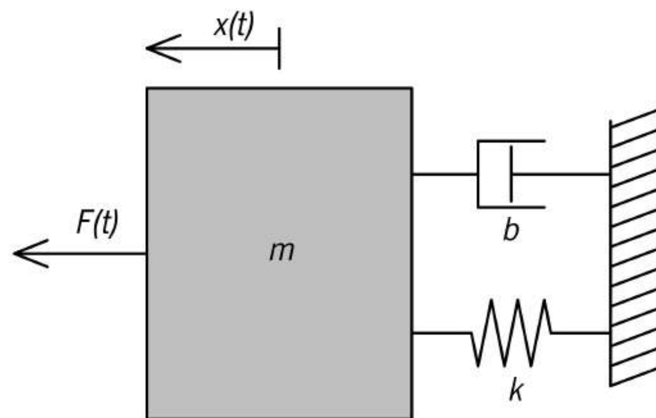

Figure 1.1: Simplified diagram of an acceleration sensor.

To detect the displacement, several transduction mechanisms can be used. Piezoresistive methods are quite common [1.24]–[1.28], where the material changes its resistance with deformation. These are typically simple devices, simplifying the fabrication process and the electronic circuitry needed [1.29] yet, they have a significant temperature dependency. Piezoelectric transduction [1.1.34]–[1.1.36] is similar to piezoresistive, but their self-generation (deformation is converted into electrical energy) eliminates the need for a power supply. Nonetheless, this advantage leads to a significant limitation: these devices can only measure dynamic accelerations, and static ones (such as gravity) cannot be detected.

Capacitive transduction is one of the most used techniques and relies on a variation of area or distance between electrodes, resulting in a capacitance change proportional to the excitation acceleration [1.33]–[1.37]. The capacitive readout circuit is typically more complex because of parasitic capacitances and low signal values, but temperature dependency can be up to two orders of magnitude smaller when compared to piezoresistive transduction [1.29]. Capacitive devices can also measure static accelerations, meaning that they can be used on a broader range of applications, justifying the large number of research works on this field.

Optical accelerometers have also been presented in literature [1.38]–[1.40], using an optical readout of a mechanical structure. Even though these devices show high sensitivity, other limitations, such as complex and expensive packaging, prevent them from reaching commercial success [1.41].

Thermal accelerometers have an operating principle that does not need a proof-mass, making them more robust and suitable for high g applications [1.42]. These only require an ambient gas, a micro-heater, and a method to measure the temperature difference caused by thermal convection. When the device is not subjected to accelerations, there is a temperature symmetry within the device, but when an acceleration is applied, the symmetry is lost [1.43], [1.44]. The main disadvantage of this transduction mechanism is low bandwidth since thermal convection is a slow process.

More recently, magnetic transduction mechanisms were also tested for accelerometers by adding permanent magnets to the moving parts and magnetic sensors or pick-up coils to the static ones [1.45]–[1.47]. Because of the limitations of the achievable magnetic fields, the sensitivity is typically low, and the materials used for permanent magnets are not commonly used on the MEMS industry, limiting mass production applications.

Regarding applications, accelerometers can be used in a variety of fields for many different purposes [1.29]. In consumer applications, accelerometers are used in smartphones for determining picture orientation, and in laptops, for hard-drive damage prevention. They are similarly used for vibration monitoring of building and bridges in civil engineering applications. Biomedical applications are also possible for activity monitoring. High-performance accelerometers are critical components in navigation and guidance systems for the automotive industry and seismometry for oil exploration and earthquake prediction. These accelerometers can be classified into four categories presented in Table 1.1, according to their performance [1.41].

Table 1.1: Acceleration sensor application grades [1.41].

Application	**Accelerometer performance**
Consumer	> 50 mg
Tactical	~ 1 mg
Navigation	25 μg
Strategic	~ 1 μg

1.2.1. Traditional versus MEMS accelerometers

Currently, the accelerometers with better noise performance are non-MEMS devices. These are used for space applications and can resolve accelerations bellow the nano *g* range. The European Space Agency (ESA) GOCE mission, launched in 2009, was equipped with six electrostatic accelerometers, named GRADIO, which have a resolution better than 0.2 pg/√Hz [1.48], [1.49]. These accelerometers are based

on the electrostatic suspension of a proof-mass, which is controlled to remain still via precise actuation voltages on control electrodes, and the control voltages are proportional to the measured acceleration. Additionally, three pairs of these accelerometers were used on a tri-axis orthogonal structure, to measure common and differential accelerations along the three-dimensional space. Despite the good results (in orbit demonstrated resolution of 0.3 pg/√Hz), these accelerometers have several drawbacks. The measurement range is restricted to ± 650 ng, and each proof-mass weighs 320 grams. Moreover, the proof masses are made out of platinum and rhodium, making them large and expensive. Furthermore, the bandwidth of the sensor is quite low (below 0.1 Hz).

Later, for ESA's GRACE follow-on missions, the GRACE-FO accelerometer was developed [1.49]. It addressed some of the drawbacks of GRADIO, by using a 72-gram Titanium alloy proof-mass and it improved the measurement range to ± 5 µg in the Y and Z axis and ±50 µg in the X axis. However, its resolution decreased to 100 pg/√Hz. This accelerometer applies a similar operational principle as GRADIO, using analog to digital sigma-delta converters to measure and control the proof-mass movement.

Several MEMS accelerometers with noise performance on the nano g range have been demonstrated [1.50]–[1.52], yet these cannot compete with the state of the art conventional macro-scale ones. The intrinsic size reduction on MEMS devices creates performance challenges, since smaller inertial masses directly translate to higher thermal-mechanical noises. Nonetheless, MEMS technology offers several benefits, such as size reduction, batch fabrication, cost reduction, and robustness. It has been demonstrated that after one year of storage, temperatures up to 200 °C and shock tolerances larger than 20000 g, the silicon proof-mass returns to the original position within 0.03 nm [1.53]. During the last decades, MEMS accelerometers have enabled new applications, and with its increased popularity and number of people dedicated to research and study them, they will keep replacing traditional accelerometers, as higher performance ones become available.

1.2.2. Microfabrication processes

Microfabrication has strong relations to integrated circuit (IC) fabrication, and many of the processing steps and tools were adopted from IC manufacturing. Yet, some specific MEMS design challenges are difficult to master, such as the packaging of movable mechanical structures and the manufacturing of thick mechanical layers. To overcome these challenges, several MEMS fabrication techniques have been developed over the years, and they are typically categorized into two groups: surface micromachining and bulk micromachining [1.9].

The surface micromachining processes are based on the process of thin films on a silicon wafer, similarly to the traditional IC manufacture [1.9]. Because of this, it is relatively easy to integrate surface micromachined devices with electrical components in the same chip, potentially achieving better performance and reducing packaging costs. Typically, a surface micromachining process starts with a silicon substrate wafer (Figure 1.2 a)), where a sacrificial layer of silicon dioxide is deposited (Figure 1.2 b)). After, the sacrificial layer is patterned and etched (Figure 1.2 c)) and the structural layer, typically made of polycrystalline silicon, is deposited on top of it (Figure 1.2 d)). In later process steps, the structural layer is defined to the desired shape using lithography and etching (Figure 1.2 e)). To finalize, the sacrificial layer is removed thus releasing the movable structural layer (Figure 1.2 f)).

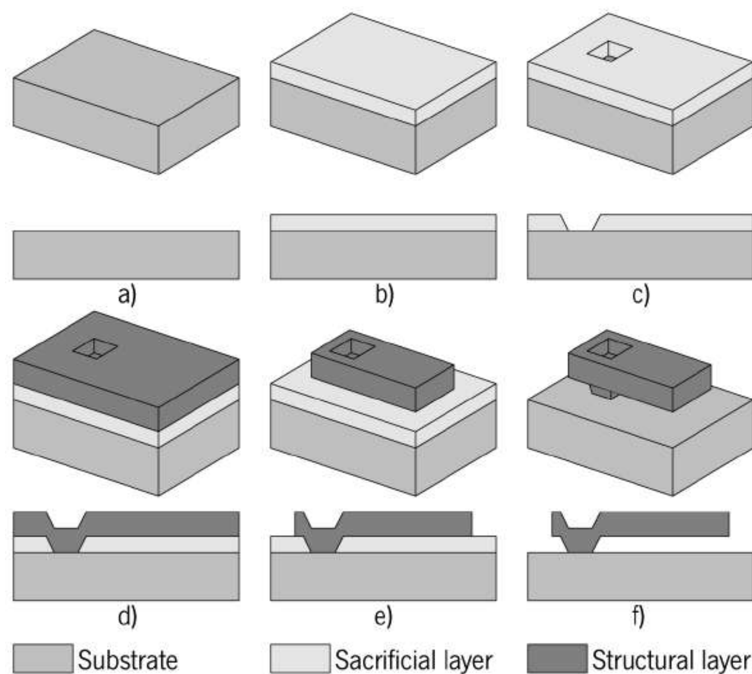

Figure 1.2: Typical surface micromachining process.

By contrast, bulk micromachining defines structures by selectively etching the substrate, resulting in relatively thick structures (the typical thickness of a wafer is 500-700 µm, about 100 times larger than the typical thickness for surface micromachined devices) [1.9]. This characteristic is of great value when designing inertial sensors, such as accelerometers and gyroscopes, since they benefit from a large proof-mass. Additionally, these devices can be made of single-crystalline silicon (instead of amorphous or polycrystalline), having more stable and predictable characteristics that are more desirable when designing mechanical sensors.

The bulk micromachining process was greatly simplified with the combination of silicon on insulator (SOI) and deep reactive ion etch (DRIE) technologies, leading to smaller and thicker devices [1.54], [1.55]. SOI

wafers are fabricated by bonding two silicon wafers together with a silicon dioxide layer between them. The handle wafer, also known as substrate, has a typical thickness of 700 µm, the buried oxide (BOX) has 1-2 µm and the structural layer is available in a range of thicknesses (from few nanometers to hundreds of micrometers). Because of this, SOI wafers are more expensive, however, this cost increase can be compensated by large process cost savings [1.9]. DRIE is a technique invented by Bosch that allows etching narrow channels through the entire wafer, resulting in almost vertical walls [1.56], [1.57].

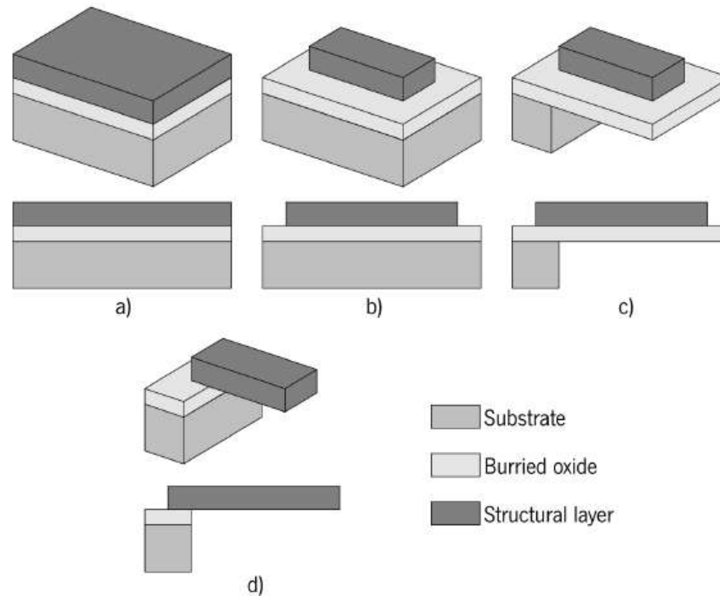

Figure 1.3: Typical bulk micromachining process using a SOI wafer.

Silicon is the material used. It has negligible fatigue and its lack of mechanical memory makes it ideal for structural elements, and its high purity and crystalline structure guarantees reproducibility and reliability of its mechanical and electrical properties [1.58], [1.59]. Additionally, silicon is abundant in nature with high purity, making it an inexpensive material.

1.2.3. Vacuum encapsulation

One major limitation in MEMS inertial sensors is the thermal-mechanical Brownian noise due to mechanical damping [1.60], however, this noise can be reduced by lowering the air damping through vacuum encapsulation. Additionally, vacuum encapsulation allows for the integration of MEMS accelerometers with other types of MEMS sensors, such as gyroscopes, resonators, and magnetometers, in a single common substrate, reducing size, fabrication and packaging cost, and potentially enabling new applications [1.61]. Nevertheless, the vacuum requirements for MEMS gyroscopes and resonators based on the Coriolis force are contradictory with the packaging requirements for MEMS accelerometers, which must be critically damped. The high quality factor resultant from vacuum encapsulation delivers

lower mechanical noise and higher sensitivity for gyroscopes and resonators but causes undesirable high settling times for accelerometers [1.36]. To contradict this phenomenon, a high quality factor transducer must be electrically damped, to be useful for sensor applications.

Furthermore, vacuum packaging protects the sensor from contaminations during fabrication processes, such as dicing, and from the external environment, allowing easy handling [1.62], [1.63]. Traditionally there are two ways of implementing vacuum packaging [1.63]. One method consists of depositing a thin film to package the devices that need vacuum. This is done after the process of making the desired devices, and then they are released as a whole. The other way of achieving vacuum encapsulation consists of bonding a cap wafer (traditionally made of silicon or glass) on top of the already defined devices. Additionally, the encapsulation gas also has a role in the performance of the devices [1.64]. When encapsulated with air, the moisture can change the material properties, causing corrosion and increasing stiction. To mitigate this problem and ensure stability, the devices can be encapsulated using noble gases, such as helium, argon, or neon.

1.2.4. Closed-loop operation

Capacitive MEMS accelerometers have gained considerable interest among the academic community and sensor manufacturers because of their good thermal stability, high sensitivity, and relatively simple batch fabrication [1.7], [1.29], [1.65]. If these devices are operated in an open-loop configuration, the mechanical deflection of the proof-mass is measured via the associated capacitance change, resulting in a relatively simple and stable sensor with low power consumption, suitable for low to medium performance applications. However, open-loop operation can limit the sensor’s performance, since it becomes sensitive to fabrication process deviations, the sensitivity and bandwidth are related to the natural frequency of the mechanical mass-spring-damper system, and the readout circuitry may need to satisfy challenging dynamic range and linearity requirements [1.53], [1.66]–[1.68]. Also, open-loop devices are not suitable for low-pressure applications, since the proper damping of all resonant modes cannot be achieved [1.69].

In contrast, operating the accelerometer in a negative feedback closed-loop has several advantages, such as better linearity, lower susceptibility to process variations, lower thermal dependency, more independence of the sensitivity-bandwidth tradeoff, higher and tunable dynamic range and relaxed readout circuit requirements [1.70]–[1.72]. Nevertheless, for a MEMS device, the feedback design can be challenging, because of sensor dynamics, relatively high-frequency system dynamics and

requirements for close integration of the control system with the actual MEMS element. Typically, for capacitive accelerometers, the feedback signal is used to control the position of the proof-mass, which has to compensate the inertial forces applied to the sensor, providing an accurate acceleration measurement [1.66]. Conventional analog control loop systems rely on derivations of the proportional-integral-derivative (PID) controller, but this method has inherent disadvantages, such as a non-linear relation between the feedback voltage and the electrostatic force [1.73], [1.74]. A linear electrostatic feedback force can only occur under the assumption of small proof-mass displacement, and additionally, if the displacement becomes large, the electrostatic pull-in phenomenon can occur, leading to stiction and possible device failure [1.75].

An excellent solution to overcome these disadvantages is to use a digital control strategy based on sigma-delta modulation. When operating a sensor with this technique, one can maintain all advantages of the traditional closed-loop control techniques, and since the feedback voltage can only have discrete levels, the feedback signal has high linearity. Sigma-delta modulation is a technique commonly used to achieve high-resolution analog-to-digital converters (ADC), but some authors have successfully embedded the inertial sensing element within a sigma-delta modulator force feedback loop [1.66]. Here, the sensing element serves not only to detect the inertial input signal but also takes a role on the loop filter itself, forming an electromechanical sigma-delta modulator (EMΣΔM). The typical blocks on this kind of system include a capacitance to voltage converter, a phase compensator, a single or multi-bit quantizer, and optional filtering blocks. In addition of providing an inherently digital output, electromechanical sigma-delta modulators can provide the electrical damping necessary for low-pressure devices, avoid electrostatic instabilities due to pull-in effects, and can realize high resolutions, representing one of the most attractive architectures for achieving high-performance MEMS inertial sensors [1.67], [1.68], [1.76].

1.3. State-of-the-art

The reviewing of the available literature is an advantageous process, mainly due to 2 reasons. First, a proper literature review helps the researcher to generate and refine its research ideas. The second reason is related to the critical literature review. The work performed by a researcher is not alone in the universe, instead, it is based on work made by others that studied the same or similar phenomena. This requires the performance of a critical literature review, where relevant work must be described and analyzed critically [1.77].

The topic of MEMS accelerometers is widely studied in the scientific community. Likewise, sigma-delta converters are also a popular subject. However, the application of sigma-delta modulation techniques on vacuum encapsulated MEMS accelerometers, commonly known as electromechanical sigma-delta modulators, although research by some authors, is a lesser studied field. The first study where a vacuum encapsulated MEMS accelerometer was operated using a sigma-delta modulator was published in 1990 by W. Henrion et al., entitled “Wide dynamic range direct digital accelerometer” [1.78]. In this study, the authors operate a vacuum encapsulated MEMS accelerometer using a second-order EMΣΔM, achieving a noise figure of 10 μg/√Hz for a bandwidth of 200 Hz. These results a quite good for the time, though, the input range was limited to 0.1 g, restricting the possible applications, and the size of the proof-mass is quite big (1×1×0.5 mm^3).

Later, in 2014, F. Chen et al. published a paper addressing a MEMS accelerometer using a sixth-order sigma-delta modulator [1.61] (Figure 1.4). The MEMS accelerometer was encapsulated in vacuum, with a pressure of 66.7 Pa, and the authors were able to achieve a noise figure of 1.2 μg/√Hz for a bandwidth of 500 Hz and a measurement range of ±6 g. The obtained results are very good, however, to achieve them, the vacuum pressure is very low, which is hard and expensive to make, and the size of the MEMS structure is considerably large (4×7×0.05 mm^3).

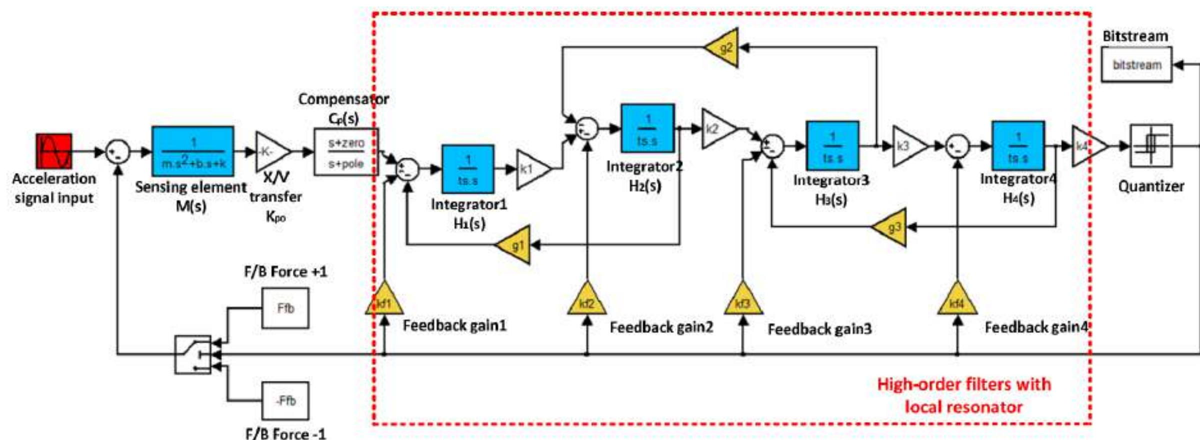

Figure 1.4: Electromechanical sigma-delta modulator architecture proposed by F. Chen et al..

In 2015, H. Xu et al., published a paper showcasing a circuit interface for a vacuum encapsulated MEMS accelerometer. The circuit realized a fifth-order electromechanical sigma-delta modulator, that was implemented in an application specific integrated circuit (ASIC). With this approach, the authors claim a noise value of 200 ng/√Hz for a 300 Hz bandwidth and 1,2g of measurement range [1.36]. These results showcase excellent noise performance, however, they are only valid when the accelerometer is being operated at 100 Hz, invalidating the 300 Hz bandwidth. Moreover, although the authors do not specify sensor size, from Figure 1.5 it is possible to have a sense for its scale, and it seems quite big.

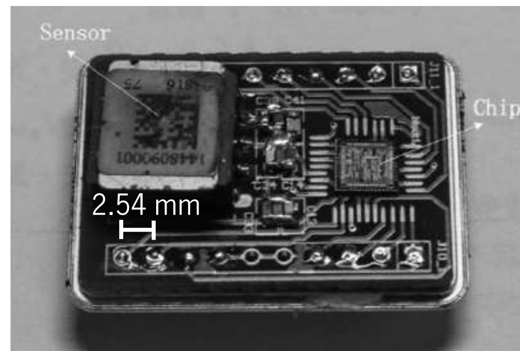

Figure 1.5: Sensor proposed by H. Xu et al. [1.36].

The article entitled "A High-Performance Digital Interface Circuit for a High-Q Micro-Electromechanical System Accelerometer" was presented by X. Li et al. in 2018 [1.79]. Here, the authors use a commercially available accelerometer (from Colibrys) and incorporate it in an analog sixth-order EMΣΔM, realizing a noise figure of 0.48 μg/√Hz for a bandwidth of 300 Hz and a range of ± 1 g. However, once again, the proof-mass size needed to achieve these results is substantial (620 μg).

Also, in 2018, Y. Wang et al. presented "A method to reduce harmonic distortion of MEMS accelerometers, proposing a fifth-order electromechanical sigma-delta architecture with feedforward and feedback loops, aiming to improve the system's performance. The noise figure achieved was 0.2 μg/√Hz for a bandwidth of 300 Hz and a range of ± 1.5 g. These are the best results reported in the literature, however, the seismic mass of this device is also the biggest registered, with a massive 14.3 mg.

Because of the mature state of these kind of devices, many non-researching institutions have been adventuring themselves into this field, such as Safran Colibrys, a Swiss company that focuses on manufacturing MEMS accelerometers. Over the years, Colibrys has been developing and improving its accelerometers, and as a result, they have some of the best high-performance MEMS accelerometers commercially available. Along the way, many scientific publications have been published, focusing on the design of the loop architecture, readout circuit, and system test [1.53], [1.80], [1.81]. In these papers, the authors propose a fifth-order electromechanical sigma-delta modulator, implemented in FPGA, and a vacuum encapsulated MEMS accelerometer, resulting in a system capable of reading accelerations up to 300 Hz of bandwidth and 15 g range, with a noise figure of 1.7 μg/√Hz. Nevertheless, the proof-mass used also has big size (3 mm^2 with a thickness of 500 μm).

Fairchild Semiconductor, a company owned by ON semiconductor, also has MEMS accelerometers products. In the context of this thesis, the FIS1100 device has particular relevance, even if it is not vacuum encapsulated or uses sigma-delta modulation. This device is a 6-axis MEMS inertial sensor, composed by

a 3-axis accelerometer and a 3-axis gyroscope, integrated into the same die [1.82]. This is advantageous because it enables the fabrication of both sensors using the same fabrication process, ultimately leading to cost and size reduction. However, it is stated that each sensor has an individual hermetic cavity, hinting at different encapsulation pressures. This increases the manufacturing complexity and cost, and it does not fully explore the benefits of same die integration. Nonetheless, the accelerometer can achieve a noise density of 50 μg/√Hz for a measurement range of ±8 g.

As stated, vacuum encapsulated accelerometers can have several advantages and potentially enable new applications. One of the significant benefits identified is the possibility of integration with other sensors, reducing in this way the overall size of the system and the fabrication and packaging cost. However, all accelerometers presented aim to achieve high-performance, exhibiting a common problem: a big size proof-mass. An accelerometer with a big proof-mass, in addition to reduce the size advantages of integration with other sensors, may present some additional problems, such as reduced full-scale range and added complexity in the manufacturing process, since the manufacturing tolerances must be smaller to ensure the stability of the sigma-delta modulator [1.83]. In the end, the bigger size and complex fabrication processes are translated in a cost increase, which is never desired.

In Table 1.2, a comparison between the identified vacuum encapsulated MEMS accelerometers operated using a sigma-delta modulation is presented. Only fabricated devices and experimental results are presented, and simulation studies were not compared.

Table 1.2: State-of-the-art comparison of vacuum encapsulated MEMS accelerometers using sigma-delta modulation.

Work	**Pressure**	**Proof-mass**	**Noise figure**	**Bandwidth**	**Dynamic range**	**Architecture**
Henrion et al. (1990) [1.78]	Vacuum	1630 μg 0.5 mm^3	10 μg/√Hz	200 Hz	0.1 g	2nd order EMΣΔM
Chen et al. (2014) [1.61]	66.7 Pa	1620 μg 1.4 mm^3	1.2 μg/√Hz	500 Hz	± 6.0 g	6th order EMΣΔM
Xu et al. (2015) [1.36]	Vacuum	Nondisclosed Seems huge	0.2 μg/√Hz	300 Hz	± 1.2 g	5th order EMΣΔM
Wang et al. (2018) [1.84]	Vacuum	14300 μg -	0.2 μg/√Hz	300 Hz	± 1.5 g	5th order EMΣΔM
Li et al. (2018) [1.79]	Vacuum	620 μg -	0.48 μg/√Hz	300 Hz	± 1.0 g	6th order EMΣΔM
Colibrys S.A [1.53], [1.80], [1.81]	Vacuum	- 1.5 mm^3	1.7 μg/√Hz	300 Hz	15 g	5th order EMΣΔM

1.4. Motivation and goals

The present thesis was developed within the scope of the doctoral program of Advanced Engineering Systems for Industry, which is promoted by the ALGORITMI Center of the University of Minho in cooperation with Bosch Car Multimedia Portugal. This doctoral program has as key characteristic a strong industry cooperation and affinity with real industry needs, with a focus on interdisciplinary, multidisciplinary, and multicultural collaboration skills. Considering that Robert Bosch GmbH is one of the leaders on MEMS technology and on the automotive industry, the opportunity for the development of a MEMS accelerometer for the automotive industry arose. Taking into consideration the previously explained characteristics of this field, **the main objective of this thesis is the development of a vacuum encapsulated MEMS accelerometer, using sigma-delta modulation, that is appropriate to integrate with other low-pressure encapsulated sensors used in the automotive industry. Additionally, the developed sensor must have a relatively small size,** eliminating the limitations explained before.

The development of a vacuum encapsulated MEMS accelerometer that uses sigma-delta modulation as the measuring technique raises several challenges and requires a multidisciplinary approach. Furthermore, its utilization on the automotive industry increases the challenge level, since this is one of the most restricted sectors, with several inflexible constraints. Thus, an additional partner, Bosch Automotive Electronics, in Reutlingen, Germany, was included in this project, providing experience in the field and facilities to fabricate the designed MEMS devices. Therefore, all resultant MEMS devices must be compliant with the Bosch microfabrication process, and the final sensor performance must align with Bosch's performance guidelines:

- The encapsulation pressure should be 140 Pa, since this is the typical encapsulation pressure of other MEMS inertial sensors.
- The device core size should be inferior to 400×400 μm^2, eliminating the previously described limitations, and enabling further cost reductions associated with the small footprint.
- The voltages levels should be inferior to 3.3 V, facilitating the ASIC integration using standard fabrication technologies.
- The performance of the sensor should comply with the typical automotive industry requirements:
  - Temperature range: [-40, +125] °C;
  - Offset stability in the temperature range: 20 mg;
  - Measurement range: ±5 g;

- Bandwidth: 400 Hz;
- Noise level: 100 μg/√Hz;
- Nonlinearity: 1% of the full-scale (FS);
- Vibration robustness: 2 g sinusoidal acceleration from 400 Hz to 50 kHz.

To achieve such a device, several intermediate objectives must be realized:

1. Investigation of the low-pressure effects on the system. High-order sigma-delta modulators can realize unstable systems if not properly tuned, which can compromise the device's feasibility, and ultimately lead to the physical destruction of the sensor element. The vacuum encapsulation of the device aggravates this phenomenon, since it drastically decreases the damping coefficient of the system. However, the decrease of the damping coefficient also leads to a decrease in the MEMS Brownian noise, which reduces the system total noise. All these effects were studied and understood.

2. Design and fabrication of the MEMS sensor element. This step must take into consideration the results from the investigation of the low-pressure effects, as well as comply with the previously defined requirements. It should be noted that the sensor will be fabricated using Bosch's fabrication process, and the proposed design must comply with all its rules.

3. Implementation of the readout, control, and actuation circuits. The MEMS accelerometer designed has a capacitive transduction mechanism, which requires a readout circuit capable of converting the changes in capacitance, caused by external accelerations, into voltage. This circuit, as well as the actuation one (responsible for the excitation voltage required in sigma-delta modulation), were implemented using analog electronic components, while the sigma-delta modulation loop was implemented in FPGA. This approach enables a novel digital sigma-delta modulator, which can perform the fine-tuning of the loop parameters, matching each specific sensor.

4. Test and characterization of the developed accelerometer. A battery of experiments was performed to fully characterize the accelerometer and validate its performance.

1.5. Organization of the thesis

Following this first chapter, where the thesis topic was introduced and state-of-the-art review was performed, the present document has four additional chapters. They are organized as follows:

Chapter 2 provides the theoretical background on electromechanical sigma-delta modulators. The mechanics of capacitive MEMS accelerometer, and details about the low-pressure damping model are provided. The theoretical concepts about oversampling and noise shaping are also presented, since they are essential to sigma-delta modulation.

The implementation of the sensor is described in chapter 3. The design and fabrication of the MEMS accelerometer are shown. The analog circuitry to read the capacitive changes and to electrostatically actuate the sensor is explained, and the digital blocks implemented in FPGA, that lead to the sensor realization, are presented. Additionally, the simulation model of the entire architecture of the system is also described.

The sensor characterization is presented in chapter 4. The main sensor characteristics, such as sensitivity, nonlinearity, noise, measurement range, thermal dependency, and cross-axis sensitivity, were experimentally evaluated, and the results are shown and compared with simulated data.

Lastly, chapter 5 concludes this work. The obtained results are discussed and compared with similar devices in the state-of-the-art. The main contributions are also presented and some recommendations for future improvements are provided.

References

[1.1] R. P. Feynman, "There's Plenty of Room at the Bottom: An Invitation to Enter a New Field of Physics," *Eng. Sci.*, 1960.

[1.2] M. R. Haskard, A. Hariz, and A. J. Marriage, "Micro engineering-a brief overview," in *Proceedings Electronic Technology Directions to the Year 2000*, pp. 242–245, doi: 10.1109/ETD.1995.403467.

[1.3] H. C. Nathanson, W. E. Newell, R. A. Wickstrom, and J. R. Davis, "The resonant gate transistor," *IEEE Trans. Electron Devices*, vol. 14, no. 3, pp. 117–133, Mar. 1967, doi: 10.1109/T-ED.1967.15912.

[1.4] E. Bassous, H. H. Taub, and L. Kuhn, "Ink jet printing nozzle arrays etched in silicon," *Appl. Phys. Lett.*, vol. 31, no. 2, pp. 135–137, Jul. 1977, doi: 10.1063/1.89587.

[1.5] L. Kuhn, E. Bassous, and R. Lane, "Silicon charge electrode array for ink jet printing," *IEEE Trans. Electron Devices*, vol. 25, no. 10, pp. 1257–1260, Oct. 1978, doi: 10.1109/T-ED.1978.19261.

[1.6] K. E. Petersen, "Fabrication of an integrated, planar silicon ink-jet structure," *IEEE Trans. Electron Devices*, vol. 26, no. 12, pp. 1918–1920, Dec. 1979, doi: 10.1109/T-ED.1979.19796.

[1.7] S. Beeby, G. Ensell, M. Kraft, and N. White, *MEMS Mechanical Sensors*. Artech House, Inc., 2004.

[1.8] C. S. Smith, "Piezoresistance Effect in Germanium and Silicon," *Phys. Rev.*, vol. 94, no. 1, pp. 42–49, Apr. 1954, doi: 10.1103/PhysRev.94.42.

[1.9] V. Kaajakari, *Practical MEMS*. Small Gear Pub., 2009.

[1.10] S. D. Senturia, *Microsystem Design*. Springer US, 2000.

[1.11] IHS Markit, "The Up and Downs of the MEMS and Sensor Market," 2016.

[1.12] Yole Développement, "Status of the MEMS Industry," 2019.

[1.13] K. Benz, "Fahrzeug mit Gasmotorenbetrieb," 37435, 1886.

[1.14] L. Brook, *Ford Model T: The Car That Put the World on Wheels*. Motorbooks, 2008.

[1.15] D. S. Eddy and D. R. Sparks, "Application of MEMS technology in automotive sensors and actuators," *Proc. IEEE*, vol. 86, no. 8, pp. 1747–1755, 1998, doi: 10.1109/5.704280.

[1.16] D. B. Rich, W. K. Kosiak, G. J. Manlove, and D. L. Schwarz, "A Remotely Mounted Crash Detection System," 1997, doi: 10.4271/973240.

[1.17] L. Spangler and C. J. Kemp, "A smart automotive accelerometer with on-chip airbag deployment circuits," in *Tech. Dig. IEEE Solid-State Sensor and Actuator Workshop*, 1996, pp. 211–214.

[1.18] P. Ernest, "MEMS@Bosch: Automotive Application and beyond," 2010.

[1.19] Yole Développement, "MEMS & Sensors for Automotive," 2017.

[1.20] A. Piltan, M. Piltan, and R. Ghodsi, "MEMS Technology in Automotive Industry: Trends and Applications," in *2011 International Conference on Management of Technology*, 2011.

[1.21] D. Sparks and L. Sala, "MEMS Inertial Sensors for Automotive and Consumer Applications," *Equip. Electron. Prod. Manuf.*, 2016.

[1.22] Bureau International des Poids et Mesures, "The International System of Units." 2019.

[1.23] J. G. Korvink and O. Paul, *MEMS: A Practical Guide to Design, Analysis, and Applications*. Berlin, Heidelberg: Springer Berlin Heidelberg, 2006.

[1.24] J. Y. Wang, T. T. Wang, and H. Guo, "A New Design of a Piezoelectric Triaxial Micro-Accelerometer," *Key Eng. Mater.*, vol. 645–646, pp. 841–846, May 2015, doi: 10.4028/www.scientific.net/KEM.645-646.841.

[1.25] K. Hari, S. K. Verma, I. R. Praveen Krishna, and V. Seena, "Out-of-plane dual flexure MEMS piezoresistive accelerometer with low cross axis sensitivity," *Microsyst. Technol.*, vol. 24, no. 5, pp. 2437–2444, May 2018, doi: 10.1007/s00542-017-3679-z.

[1.26] Y. Xu, L. Zhao, Z. Jiang, J. Ding, T. Xu, and Y. Zhao, "Analysis and design of a novel piezoresistive accelerometer with axially stressed self-supporting sensing beams," *Sensors Actuators A Phys.*, vol. 247, pp. 1–11, Aug. 2016, doi: 10.1016/j.sna.2016.04.053.

[1.27] P. Wang *et al.*, "A piezoresistive micro-accelerometer with high frequency response and low transverse effect," *Meas. Sci. Technol.*, vol. 28, no. 1, p. 015103, Jan. 2017, doi: 10.1088/1361-6501/28/1/015103.

[1.28] V. Seena, K. Hari, S. Prajakta, R. Pratap, and V. Ramgopal Rao, "A novel piezoresistive polymer nanocomposite MEMS accelerometer," *J. Micromechanics Microengineering*, vol. 27, no. 1, p. 015014, Jan. 2017, doi: 10.1088/0960-1317/27/1/015014.

[1.29] N. Yazdi, F. Ayazi, and K. Najafi, "Micromachined inertial sensors," *Proc. IEEE*, vol. 86, no. 8, pp. 1640–1659, 1998, doi: 10.1109/5.704269.

[1.30] Z. Shen, C. Y. Tan, K. Yao, L. Zhang, and Y. F. Chen, "A miniaturized wireless accelerometer with micromachined piezoelectric sensing element," *Sensors Actuators A Phys.*, vol. 241, pp. 113–119, Apr. 2016, doi: 10.1016/j.sna.2016.02.022.

[1.31] B. Tian, H. Liu, N. Yang, Y. Zhao, and Z. Jiang, "Design of a Piezoelectric Accelerometer with High Sensitivity and Low Transverse Effect," *Sensors*, vol. 16, no. 10, p. 1587, Sep. 2016, doi: 10.3390/s16101587.

[1.32] Y.-H. Wang *et al.*, "A Paper-Based Piezoelectric Accelerometer," *Micromachines*, vol. 9, no. 1, p. 19, Jan. 2018, doi: 10.3390/mi9010019.

[1.33] X. Zhou, L. Che, S. Liang, Y. Lin, X. Li, and Y. Wang, "Design and fabrication of a MEMS capacitive accelerometer with fully symmetrical double-sided H-shaped beam structure," *Microelectron. Eng.*, vol. 131, pp. 51–57, Jan. 2015, doi: 10.1016/j.mee.2014.10.005.

[1.34] S. Kavitha, R. Joseph Daniel, and K. Sumangala, "Design and Analysis of MEMS Comb Drive Capacitive Accelerometer for SHM and Seismic Applications," *Measurement*, vol. 93, pp. 327–339, Nov. 2016, doi: 10.1016/j.measurement.2016.07.029.

[1.35] A. Aydemir, Y. Terzioglu, and T. Akin, "A new design and a fabrication approach to realize a high performance three axes capacitive MEMS accelerometer," *Sensors Actuators A Phys.*, vol. 244, pp. 324–333, Jun. 2016, doi: 10.1016/j.sna.2016.04.007.

[1.36] H. Xu, X. Liu, and L. Yin, "A closed-loop $\Sigma\Delta$ interface for a high-Q micromechanical capacitive accelerometer with 200 ng/$\sqrt{}$Hz input noise density," *IEEE J. Solid-State Circuits*, vol. 50, no. 9, pp. 2101–2112, Sep. 2015, doi: 10.1109/JSSC.2015.2428278.

[1.37] M. G. Guney, X. Li, V. P. J. Chung, J. Paramesh, T. Mukherjee, and G. K. Fedder, "High dynamic range CMOS-MEMS capacitive accelerometer array," in *2018 IEEE Micro Electro Mechanical Systems (MEMS)*, 2018, pp. 992–995, doi: 10.1109/MEMSYS.2018.8346725.

[1.38] K. Huang, M. Yu, L. Cheng, J. Liu, and L. Cao, "A Proposal for an Optical MEMS Accelerometer With High Sensitivity Based on Wavelength Modulation System," *J. Light. Technol.*, vol. 37, no. 21, pp. 5474–5478, Nov. 2019, doi: 10.1109/JLT.2019.2934776.

[1.39] T. Wang and S. Zhang, "Silicon micromechanical accelerometer using an optical fiber," 2002, p. 264, doi: 10.1117/12.483183.

[1.40] R. L. Waters and T. E. Jones, "MEMS Navigation-Grade Electro-Optical Accelerometer," *Mil.*

Capab. Enabled by Adv. Navig. Sensors, 2007.

[1.41] N. M. Barbour, "Inertial Navigation Sensors," in *RTO-ENSET-116*, 2011.

[1.42] C. L. M. Everhart *et al.*, "High stability thermal accelerometer based on ultrathin platinum ALD nanostructures," in *2018 IEEE Micro Electro Mechanical Systems (MEMS)*, 2018, pp. 976–979, doi: 10.1109/MEMSYS.2018.8346721.

[1.43] Z. Li, W. Chang, S. Sun, C. Gao, and Y. Hao, "A Novel Mems 3-Axis Thermal Accelerometer with 5-Wire Structure Using Planar Stacking Method," in *2019 20th International Conference on Solid-State Sensors, Actuators and Microsystems & Eurosensors XXXIII (TRANSDUCERS & EUROSENSORS XXXIII)*, 2019, pp. 1819–1822, doi: 10.1109/TRANSDUCERS.2019.8808669.

[1.44] J. Kim, M. Han, S.-W. Kang, S. Kong, and D. Jung, "Multi-axis Response of a Thermal Convection-based Accelerometer," *Micromachines*, vol. 9, no. 7, p. 329, Jun. 2018, doi: 10.3390/mi9070329.

[1.45] B. Ando, S. Baglio, V. Marletta, A. Valastro, A. Pistorio, and C. Trigona, "A friction less accelerometer exploiting a magnetic levitating mechanism and an inductive readout strategy," in *2017 IEEE International Instrumentation and Measurement Technology Conference (I2MTC)*, 2017, pp. 1–5, doi: 10.1109/I2MTC.2017.7969961.

[1.46] O. Ergeneman *et al.*, "An in-plane cobalt–nickel microresonator sensor with magnetic actuation and readout," *Sensors Actuators A Phys.*, vol. 188, pp. 120–126, Dec. 2012, doi: 10.1016/j.sna.2012.05.035.

[1.47] R. A. Dias *et al.*, "Novel magnetic readout for hybrid spintronic MEMS devices," in *2017 19th International Conference on Solid-State Sensors, Actuators and Microsystems (TRANSDUCERS)*, 2017, pp. 818–821, doi: 10.1109/TRANSDUCERS.2017.7994174.

[1.48] J.-P. Marque *et al.*, "The ultra sensitive accelerometers of the ESA GOCE mission," in *59th International Astronautical Congress*, 2008.

[1.49] B. Christophe *et al.*, "A new generation of ultra-sensitive electrostatic accelerometers for GRACE Follow-on and towards the next generation gravity missions," *Acta Astronaut.*, vol. 117, pp. 1–7, Dec. 2015, doi: 10.1016/j.actaastro.2015.06.021.

[1.50] W. Wu, Z. Li, J. Liu, J. Fan, and L. Tu, "A nano-g MEMS accelerometer for earthquake monitoring," in *2017 19th International Conference on Solid-State Sensors, Actuators and Microsystems (TRANSDUCERS)*, 2017, pp. 599–602, doi: 10.1109/TRANSDUCERS.2017.7994120.

[1.51] U. Krishnamoorthy *et al.*, "In-plane MEMS-based nano-g accelerometer with sub-wavelength optical resonant sensor," *Sensors Actuators A Phys.*, vol. 145–146, pp. 283–290, Jul. 2008, doi: 10.1016/j.sna.2008.03.017.

[1.52] J. Laine and D. Mougenot, "A high-sensitivity MEMS-based accelerometer," *Lead. Edge*, vol. 33, no. 11, pp. 1234–1242, Nov. 2014, doi: 10.1190/tle33111234.1.

[1.53] Y. Dong, P. Zwahlen, A. M. Nguyen, R. Frosio, and F. Rudolf, "Ultra-high precision MEMS accelerometer," in *16th International Solid-State Sensors, Actuators and Microsystems*

Conference, 2011, pp. 695–698, doi: 10.1109/TRANSDUCERS.2011.5969218.

[1.54] T. J. Brosnihan, J. M. Bustillo, A. P. Pisano, and R. T. Howe, “Embedded interconnect and electrical isolation for high-aspect-ratio, SOI inertial instruments,” in *Proceedings of International Solid State Sensors and Actuators Conference (Transducers ’97)*, vol. 1, pp. 637–640, doi: 10.1109/SENSOR.1997.613732.

[1.55] F. Ayazi and K. Najafi, “High aspect-ratio combined poly and single-crystal silicon (HARPSS) MEMS technology,” *J. Microelectromechanical Syst.*, vol. 9, no. 3, pp. 288–294, Sep. 2000, doi: 10.1109/84.870053.

[1.56] F. Laermer and A. Urban, “Milestones in deep reactive ion etching,” in *The 13th International Conference on Solid-State Sensors, Actuators and Microsystems, 2005. Digest of Technical Papers. TRANSDUCERS ’05.*, vol. 2, pp. 1118–1121, doi: 10.1109/SENSOR.2005.1497272.

[1.57] C. Liu, *Foundations of MEMS*, 2 edition. Pearson, 2011.

[1.58] B. E. Boser and R. T. Howe, “Surface micromachined accelerometers,” *IEEE J. Solid-State Circuits*, vol. 31, no. 3, pp. 366–375, Mar. 1996, doi: 10.1109/4.494198.

[1.59] K. E. Petersen, “Silicon as a mechanical material,” *Proc. IEEE*, vol. 70, no. 5, pp. 420–457, May 1982, doi: 10.1109/PROC.1982.12331.

[1.60] T. B. Gabrielson, “Mechanical-thermal noise in micromachined acoustic and vibration sensors,” *IEEE Trans. Electron Devices*, vol. 40, no. 5, pp. 903–909, May 1993, doi: 10.1109/16.210197.

[1.61] F. Chen, W. Yuan, H. Chang, I. Zeimpekis, and M. Kraft, “Low noise vacuum MEMS closed-loop accelerometer using sixth-order multi-feedback loops and local resonator sigma delta modulator,” in *IEEE 27th International Conference on Micro Electro Mechanical Systems (MEMS)*, 2014, pp. 761–764, doi: 10.1109/MEMSYS.2014.6765752.

[1.62] E. Esashi, “Wafer level packaging of MEMS,” in *TRANSDUCERS 2009 - 2009 International Solid-State Sensors, Actuators and Microsystems Conference*, 2009, pp. 9–16, doi: 10.1109/SENSOR.2009.5285574.

[1.63] B. Lee, S. Seok, and K. Chun, “A study on wafer level vacuum packaging for MEMS devices,” *J. Micromechanics Microengineering*, vol. 13, no. 5, pp. 663–669, Sep. 2003, doi: 10.1088/0960-1317/13/5/318.

[1.64] Y. C. Lee, Y.-T. Cheng, and R. Ramadoss, *MEMS Packaging*, vol. 05. WORLD SCIENTIFIC, 2018.

[1.65] H. Xie and G. K. Fedder, “Integrated Microelectromechanical Gyroscopes,” *J. Aerosp. Eng.*, vol. 16, no. 2, pp. 65–75, Apr. 2003, doi: 10.1061/(ASCE)0893-1321(2003)16:2(65).

[1.66] F. Chen, X. Li, and M. Kraft, “Electromechanical Sigma-Delta Modulators (ΣΔM) Force Feedback Interfaces for Capacitive MEMS Inertial Sensors: A Review,” *IEEE Sens. J.*, vol. 16, no. 17, pp. 6476–6495, Sep. 2016, doi: 10.1109/JSEN.2016.2582198.

[1.67] Jiangfeng Wu and L. R. Carley, “Electromechanical ΔΣ modulation with high-Q micromechanical accelerometers and pulse density modulated force feedback,” *IEEE Trans. Circuits Syst. I Regul.*

Pap., vol. 53, no. 2, pp. 274–287, Feb. 2006, doi: 10.1109/TCSI.2005.857084.

[1.68] R. Wilcock and M. Kraft, “Genetic Algorithm for the Design of Electro-Mechanical Sigma Delta Modulator MEMS Sensors,” *Sensors*, vol. 11, no. 12, pp. 9217–9232, Sep. 2011, doi: 10.3390/s111009217.

[1.69] L. Aaltonen and K. Halonen, “Continuous-time interface for a micromachined capacitive accelerometer with NEA of 4g and bandwidth of 300Hz,” *Sensors Actuators A Phys.*, vol. 154, no. 1, pp. 46–56, Aug. 2009, doi: 10.1016/j.sna.2009.07.011.

[1.70] M. Kraft, R. Wilcock, and B. Almutairi, “Innovative control systems for MEMS inertial sensors,” in *Frequency Control Symposium, IEEE International*, 2012.

[1.71] J. Soen, A. Voda, and C. Condemine, “Controller design for a closed-loop micromachined accelerometer,” *Control Eng. Pract.*, vol. 15, no. 1, pp. 57–68, 2006, doi: 10.1016/j.conengprac.2006.03.001.

[1.72] B. Borovic, A. Q. Liu, D. Popa, H. Cai, and F. L. Lewis, “Open-loop versus closed-loop control of MEMS devices: choices and issues,” *J. Micromechanics Microengineering*, vol. 15, no. 10, pp. 1917–1924, 2005, doi: 10.1088/0960-1317/15/10/018.

[1.73] A. Fargas-Marques, J. Casals-Terre, and A. M. Shkel, “Resonant Pull-In Condition in Parallel-Plate Electrostatic Actuators,” *J. Microelectromechanical Syst.*, vol. 16, no. 5, pp. 1044–1053, Oct. 2007, doi: 10.1109/JMEMS.2007.900893.

[1.74] J. I. Seeger and B. E. Boser, “Parallel-plate driven oscillations and resonant pull-in,” in *Solid-State Sensor, Actuator and Microsystems Worksho*, 2002, pp. 313–316.

[1.75] M. Kraft, C. P. Lewis, and T. G. Hesketh, “Closed-loop silicon accelerometers,” *IEE Proc. - Circuits, Devices Syst.*, vol. 145, no. 5, p. 325, 1998, doi: 10.1049/ip-cds:19982275.

[1.76] Z. Meimei, Q. Haiyang, and Z. Fuqiang, “Comparisons of Feed-Forward and Multiple-Feedback Sigma-Delta Modulators for MEMS Accelerometers,” *MATEC Web Conf.*, vol. 56, p. 08003, Apr. 2016, doi: 10.1051/matecconf/20165608003.

[1.77] M. Saunders, P. Lewis, and A. Thornhill, *Research Methods for Business Students*, 5th ed. Pearson Education, 2009.

[1.78] W. Henrion, L. DiSanza, M. Ip, S. Terry, and H. Jerman, “Wide dynamic range direct digital accelerometer,” in *IEEE 4th Technical Digest. on Solid-State Sensor and Actuator Workshop*, 1990, pp. 153–157, doi: 10.1109/SOLSEN.1990.109842.

[1.79] X. Li, J. Hu, and X. Liu, “A High-Performance Digital Interface Circuit for a High-Q Micro-Electromechanical System Accelerometer,” *Micromachines*, vol. 9, no. 12, 2018, doi: 10.3390/mi9120675.

[1.80] P. Zwahlen, A.-M. Nguyen, Y. Dong, F. Rudolf, M. Pastre, and H. Schmid, “Navigation grade MEMS accelerometer,” in *IEEE 23rd International Conference on Micro Electro Mechanical Systems (MEMS)*, 2010, pp. 631–634, doi: 10.1109/MEMSYS.2010.5442327.

[1.81] P. Zwahlen *et al.*, “Breakthrough in high performance inertial navigation grade Sigma-Delta MEMS accelerometer,” in *IEEE/ION Position, Location and Navigation Symposium*, 2012, pp. 15–19, doi: 10.1109/PLANS.2012.6236858.

[1.82] C. Acar, “High-Performance 6-Axis MEMS Inertial Sensor Based on Through-Silicon Via Technology,” in *2016 IEEE International Symposium on Inertial Sensors and Systems*, 2016, pp. 62–65, doi: 10.1109/ISISS.2016.7435545.

[1.83] U. Sonmez, H. Kulah, and T. Akin, “A fourth order unconstrained ΔΣ capacitive accelerometer,” in *16th International Solid-State Sensors, Actuators and Microsystems Conference*, 2011, no. 1, pp. 707–710, doi: 10.1109/TRANSDUCERS.2011.5969214.

[1.84] Y. H. Wang, L. Yin, D. L. Chen, L. Li, and X. W. Liu, “A method to reduce harmonic distortion of MEMS accelerometer,” *Mod. Phys. Lett. B*, vol. 32, no. 21, 2018, doi: 10.1142/S0217984918502469.

2. Electromechanical sigma-delta modulator

To design a vacuum encapsulated MEMS accelerometer that uses sigma-delta modulation, comprehensive knowledge of the theoretical background on the mechanics and electrostatic coupling for MEMS devices is required. Additionally, a broad understanding of the sigma-delta modulation technique is paramount. Thus, this chapter is structured into three main sections.

The first section is dedicated to the mechanics of capacitive MEMS accelerometers, explaining the one degree of freedom (1-DOF) model, as well as the differential operation. Additionally, details about the low-pressure damping model are also provided.

The second section focus on the closed-loop operation. This section starts by the study of the electrostatic force needed for the feedback. Following, the origins of the sigma-delta modulation technique are discussed, and the theoretical background is addressed. After, the inclusion of the sensor element in the loop is studied, achieving an electromechanical sigma-delta modulator, and all components of the system are explained in detail.

Finally, the last section describes the nonlinearities of the system. The capacitance, electrostatic force, and damping coefficient nonlinearities are addressed, and the pull-in phenomenon is explained. The temperature dependence of silicon and the consequent effects are also analyzed.

2.1. One degree of freedom MEMS device

The sensor element considered for this thesis is a MEMS accelerometer with a gap varying parallel-plate capacitor, with one movable plate and one fixed plate. The movable plate has one degree of freedom, and when the device is subjected to an external acceleration, the inter-plate distance changes, as illustrated in Figure 2.1. The capacitance between two parallel-plates can be defined as [2.1]:

$$C_0 = \varepsilon \frac{A}{d_0}. \quad (2.1)$$

where ε is the dielectric constant of the material between plates, A is the overlapping area between plates, and d_0 is the distance between plates. If one plate moves towards the other, decreasing the gap between them, the capacitance increases. Consequently, if the plates move away from each other, the capacitance will decrease. Including the displacement *(x)* as part of the system, the capacitance is given by:

$$C_x = \varepsilon \frac{A}{d_0 - x}. \quad (2.2)$$

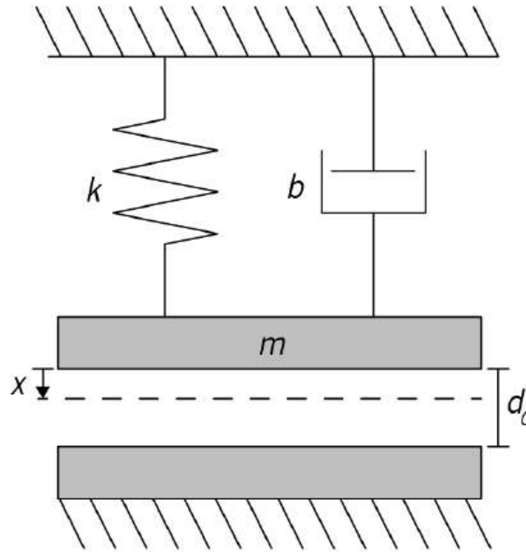

Figure 2.1: Schematic of a capacitive MEMS accelerometer with one degree of freedom.

The movable plate is anchored to a mechanical spring with stiffness k, and the consequent elastic force increases for a decreasing gap, contrary to the movement direction. Therefore, the elastic force is given by:

$$F_{elast} = -kx. \quad (2.3)$$

Many spring shapes and architectures can be made using silicon. Nonetheless, for simplicity's sake, only guided beams (one end fixed and one end guided) are analyzed. For this type of mechanical springs, the linear elastic coefficient, perpendicular to its length, can be calculated using:

$$k = \frac{12EI}{l^3}, \tag{2.4}$$

where E is the Young modulus of the material (silicon in this case), l is the length of the beam, and I is the second moment of inertia, defined by:

$$I = \frac{1}{12} w^3 t, \tag{2.5}$$

where w and t are the width and thickness of the beam, respectively.

As the plate moves with a certain velocity, a damping force is generated. This force is caused by the viscosity of the fluid that fills the gap between plates. In this case, because the gap distance is typically only a few micrometers, and relatively small when compared with the width and length of the plates, a damping mechanism called squeeze-film damping is created. This force is contrary to the movement of the plate and directly proportional to the plate velocity, being expressed as:

$$F_{damp} = -b\frac{dx}{dt}. \tag{2.6}$$

where b is the damping coefficient, dependent on the fluid properties and physical dimensions of the plates. Since the sensor will be encapsulated in vacuum, the details about the damping coefficient will be discussed in section 2.1.1.

When an object moves through a fluid, pressure and friction drag forces can also be created, which are also dependent on the fluid properties, the geometry of the object, and the Reynolds number. However, squeeze-film damping forces (when present) are several orders of magnitude higher than drag forces. Since the devices considered for this research work are based on parallel-plate geometry with a movement normal to the plates, creating squeeze-film damping, drag forces were not considered.

As a consequence of the moving plate mass, another force contributes to the system's dynamics: the moment of inertia, given by:

$$F_i = -m\frac{d^2x}{dt^2}. \tag{2.7}$$

Additionally, the device can be subjected to external forces such as acceleration. These forces are defined by (2.8), where a symbolizes the external acceleration applied to the device.

$$F_{acc} = ma \tag{2.8}$$

Since all the forces present on the system are in equilibrium:

$$F_{elast} + F_{damp} + F_i + F_{acc} = 0\,. \tag{2.9}$$

which can be rewritten as (2.10), demonstrating that the system can be represented as a second-order mechanical system.

$$-kx - b\frac{dx}{dt} - m\frac{d^2x}{dt^2} + ma = 0 \Leftrightarrow m\frac{d^2x}{dt^2} + b\frac{dx}{dt} + kx = ma \tag{2.10}$$

In a second-order mechanical system, the natural frequency *(ω_0)* and quality factor *(Q)* can be defined by (2.11) and (2.12), respectively.

$$\omega_0 = \sqrt{\frac{k}{m}} \tag{2.11}$$

$$Q = \frac{\sqrt{km}}{b} \tag{2.12}$$

Reformulating (2.10), one can emphasize these parameters that characterize the system dynamics:

$$\frac{d^2x}{dt^2} + \frac{\omega_0}{Q}\frac{dx}{dt} + \omega_0^{\,2}x = a\,. \tag{2.13}$$

According to the quality factor, the system has different behaviors. The system is overdamped if Q<0.5, critically damped if Q=0.5, and underdamped if Q>0.5. An underdamped system presents an oscillatory behavior, while in an overdamped system no oscillations are present. This behavior can be seen in Figure 2.2 and Figure 2.3, where typical Bode plots and step response graphics for these type of systems are presented.

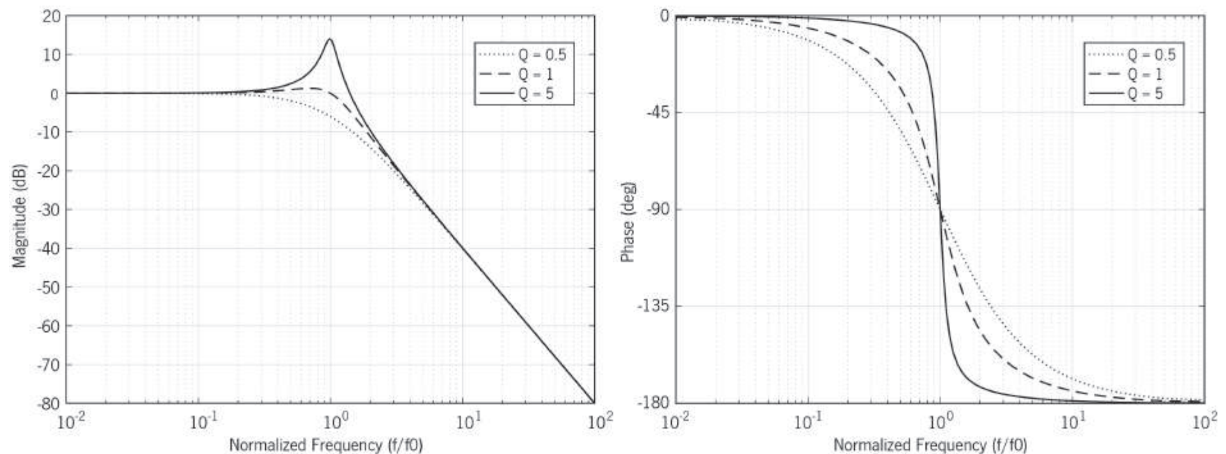

Figure 2.2: System Bode plot for different quality factors.

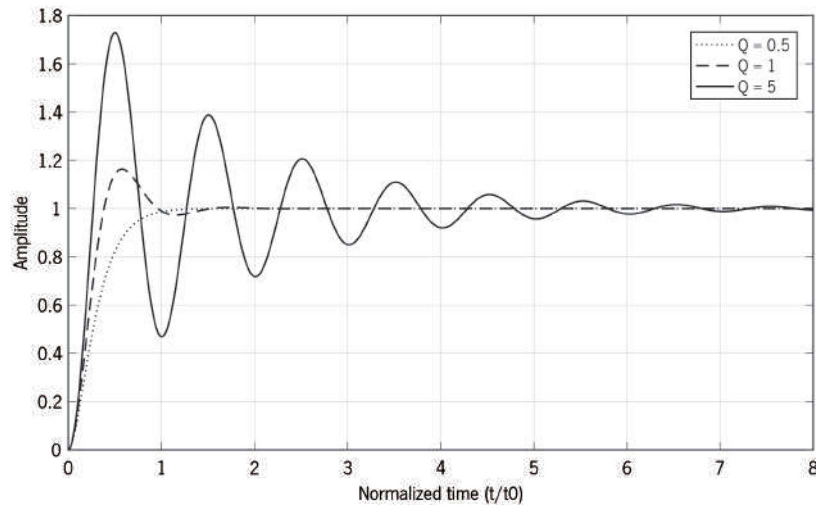

Figure 2.3: System step response for different quality factors.

2.1.1. Low-pressure model

Current research mainly focuses on the continuum regime of squeeze film damping. However, this regime is only valid for structures with large dimensions or operated at (or marginally below) atmospheric pressure [2.2]. For sub-micrometer gaps or vacuum operated devices, the interaction between individual gas molecules and the MEMS device becomes dominant over the internal viscous forces [2.3], and with the miniaturization trend and an increased number of applications where vacuum is required, an accurate model for the so-called free molecular regime is necessary. This is important to reliably predict the dynamic behavior of systems such as resonators, gyroscopes, and accelerometers.

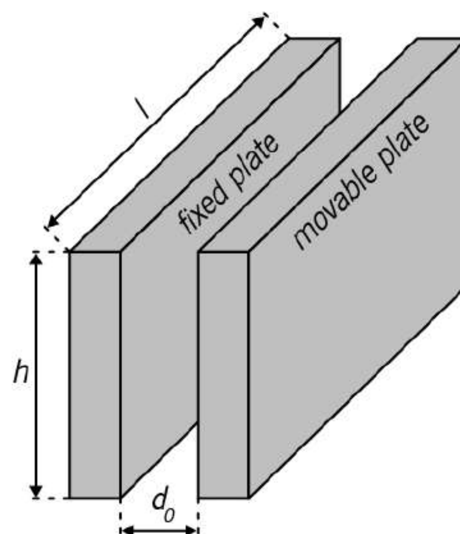

Figure 2.4: Plates architecture.

Some authors investigated this thematic, as is the case of Bao [2.4]. In 2002, he developed a model based on the energy transferred between gas molecules and a microstructure, centered on the changes

in the velocity of a molecule that collides with the movable structure [2.4]. According to the research, the damping coefficient can be represented by:

$$b_{Bao} = \frac{(l+h)\times l\times h\times P_0}{4\pi\times d_0}\times\sqrt{\frac{2\times m_m}{\pi\times k_B\times T}}, \tag{2.14}$$

where l and h are the length and height of the plates, P_0 is the device's pressure, m_m is the molar mass of the gas between plates, k_B is the Boltzmann constant, and T is the temperature (plates architecture illustrated in Figure 2.4). Nevertheless, to obtain this expression, three assumptions were made: constant particle velocity, constant change in particle velocity, and constant beam position. Later, in 2004, Hutcherson discovered that the constant particle velocity assumption was incorrect [2.5]. He developed a molecular dynamics algorithm, based on Bao's energy transfer model, that tracked the interaction of each molecule in the gap between plates, and the results show that Bao's model underestimates the damping force by a factor of 2.23:

$$b_{Hutcherson} = 2.23\times b_{Bao} = 2.23\times\frac{(l+h)\times l\times h\times P_0}{4\pi\times d_0}\times\sqrt{\frac{2\times m_m}{\pi\times k_B\times T}}. \tag{2.15}$$

The expression (2.15) would be later corroborated by Mol through experimental measurements [2.3]. The results showed that Hutcherson's estimation, despite not following the trend of the measurement results for higher pressures, fits the experimental data within a 5% error in the free molecular regime. Since the devices of this thesis will be operated with a pressure of 140 Pa, an order of magnitude below the limit of the free molecular regime (according to Mol experiments [2.3]), substituting (2.15) in (2.6), the damping force model for the low-pressure devices used is:

$$F_{damp} = -\frac{2.23\times N\times(l+h)\times l\times h\times P_0}{4\pi\times d_0}\times\sqrt{\frac{2\times m_m}{\pi\times k_B\times T}}\times\frac{dx}{dt}, \tag{2.16}$$

where N symbolizes the number of parallel-plate electrodes.

2.1.2. Differential operation

At the beginning of this chapter, a simplistic representation of a MEMS accelerometer using parallel-plate capacitors was presented (Figure 2.1). However, the aforementioned architecture only has one capacitor, which is sensitive to several effects, such as temperature variations, fabrication process deviations, charge effects, among others. A differential architecture would help mitigate these problems, greatly reducing (or even eliminating) all the common-mode effects present. In Figure 2.5, a differential sensor is proposed, where one movable plate shifts between two fixed ones.

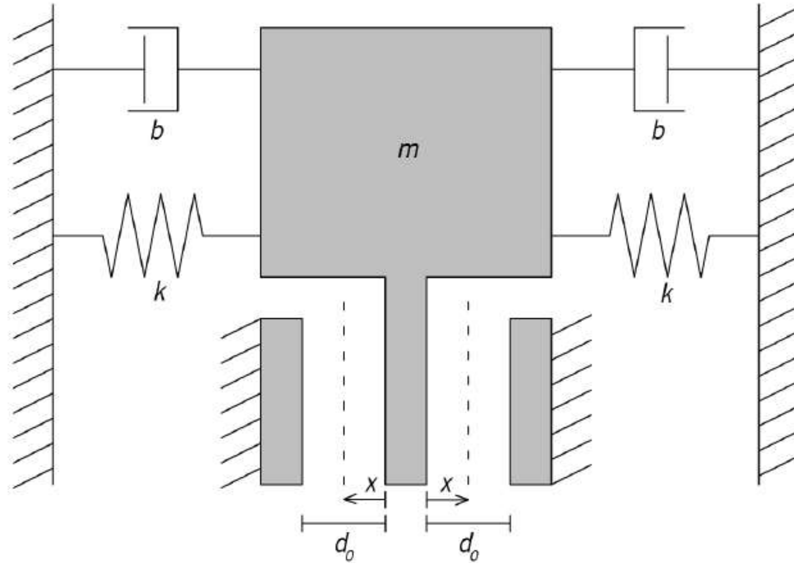

Figure 2.5: Schematic of an ideal differential capacitive MEMS accelerometer.

Assuming that there is an acceleration from left to right, the seismic mass, and consequently, the movable electrode, will shift to the left, increasing the capacitance of the left capacitor and decreasing the capacitance of the right capacitor. If we subtract one capacitance from the other, all common effects (such as temperature dependency) are significantly reduced. Assuming that both fixed plates have the same dimensions and that they are equally distant from the movable one at rest position, the resultant capacitance of the sensor is given by:

$$C_x = C_{left} - C_{right} = \varepsilon \frac{A}{d_0 - x} - \varepsilon \frac{A}{d_0 + x}. \quad (2.17)$$

2.2. Closed-loop operation

The main objective of this thesis is to develop a MEMS accelerometer that can be integrated at die level with other inertial sensors used in the automotive industry, such as gyroscopes. To achieve this, the accelerometer must be encapsulated at low-pressure, enabling for gyroscopes and accelerometers to operate in the same hermetic cavity. Additionally, the use of vacuum helps to reduce the thermal-mechanical Brownian noise [2.6], improving the accelerometer's noise performance. However, the high quality factor resultant from vacuum encapsulation causes undesirable high settling times for accelerometers [2.7]–[2.10], as depicted in Figure 2.3. To mitigate this problem, the system must be electrically damped to be useful for sensor applications.

From the many closed-loop techniques available, electromechanical sigma-delta modulation can provide the electrical damping necessary for low-pressure accelerometers while enabling high resolution and linearity, and low thermal dependency and susceptibility to process variations, representing one of the

most attractive architectures for achieving high-performance MEMS inertial sensors [2.11]–[2.13]. Additionally, including the MEMS sensor element into a sigma-delta modulating loop enables the realization of a digital sensor interface.

The fundamental operation of an electromechanical sigma-delta modulator consists of maintaining the proof-mass at the rest position using differential electrostatic electrodes, which only have two levels – ON, where a voltage (V_A) is applied, and OFF, where no voltage is applied. The resultant electrostatic force can be calculated using (2.18), where C_{A0} is the actuation capacitance for rest position of the proof-mass.

$$F_{el} = \frac{V_A^{\,2} C_{A0} d_0}{2(d_0 - x)^2} \tag{2.18}$$

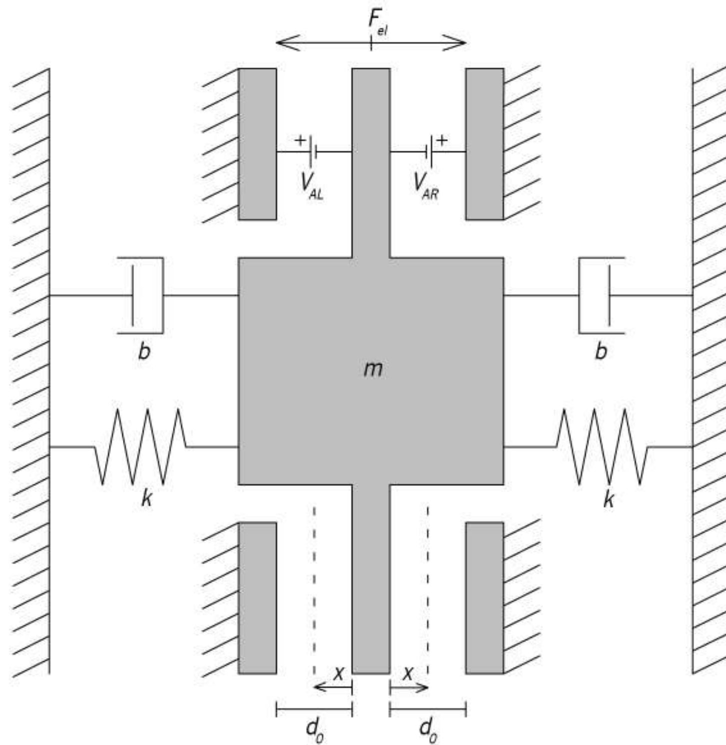

Figure 2.6: Schematic of an ideal differential capacitive MEMS accelerometer with electrostatic actuation.

In a simplistic way, if the seismic mass is shifted to the left side, V_A is applied to the right actuator, and the system outputs a zero. Likewise, if the seismic mass is shifted to the right side, V_A is applied to the left actuator and the system outputs a one. These zeros and ones are named bitstream and are the system's output. So, if the sensor is subjected to an external acceleration from the left to the right direction, the output (bitstream) will have more zeros than ones, and vice-versa. The bitstream is filtered and decimated in a latter stage in order to achieve the desired result. To implement electrostatic actuation and thus enable the use of sigma-delta modulation, two additional electrodes can be added to the device illustrated in Figure 2.5. The overall schematic of the device is depicted in Figure 2.6.

2.2.1. Sigma-delta modulation

Nowadays, sigma-delta modulation is widely used, however, its development had a long time span. Delta modulation was simultaneously developed by three companies, Bell Telephone Labs [2.14], ITT Laboratories [2.15], and Philips Research Laboratories [2.16], in 1952. Later, in 1954, the concept of oversampling and noise shaping was introduced and patented by Cutler [2.17], with the objective to achieve higher signal-to-noise ratio (SNR) in a defined frequency band, instead of the traditional goal of reducing the data rate of a given signal. At this point in time, all elements of a modern sigma-delta modulator were invented, with the exception of the digital decimation filter required to achieve a Nyquist rate signal whilst minimizing modulated high-frequency noise. Nevertheless, the name delta-sigma modulator was only introduced in 1962 by Inose et al. [2.18]. In 1969 the digital decimator filter became feasible, and it was described for the first time [2.19]. Finally, in 1974, Candy published the first multi-bit sigma-delta modulator [2.20]. Around the same time, the name sigma-delta modulation was introduced as an alternative to delta-sigma modulation, and both names are still in use [2.21].

Because of the poor initial performance, during the '70s, sigma-delta modulators were mainly used to encode low-frequency audio signals (analog-to-digital conversion) and to create black and white images for printing [2.21]. Nowadays, after all the research and improvements on sigma-delta modulators, this technique is used to achieve state-of-the-art ADCs, using multi-bit quantizers capable of converting 10's of MHz bandwidth with high dynamic range.

The sigma-delta modulation technique is based on two basic principles: oversampling and noise shaping [2.21]. Oversampling relies on an acquisition rate superior to the Nyquist rate. Increasing the sampling rate does not affect the signal power and the total quantization noise, and consequently, the signal to quantization noise ratio stays the same. However, the quantization noise is distributed over a broader frequency range, decreasing its spectral density. Considering that the interest is only on the original band of the sampled signal (based band or Nyquist band/2), the quantization noise power is halved for every doubling of the sampling ratio, improving the signal to quantization ratio. This effect is depicted in Figure 2.7, for an oversampling ratio (OSR) of 1, 2, and 4.

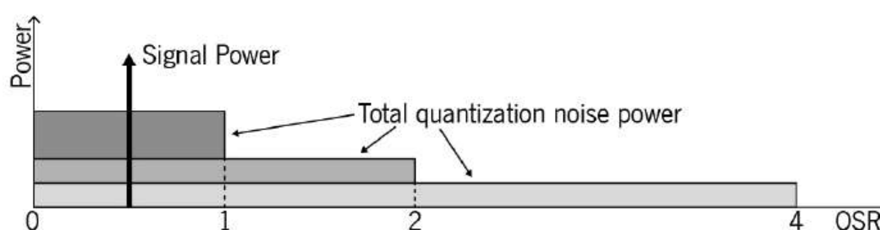

Figure 2.7: Oversampling effects on the quantization noise power density.

In a second stage, noise shaping is used to further improve the signal to quantization noise ratio [2.21]. Here, the frequency distribution of the quantization noise is shaped in a way that the quantization noise density reduces in the base band and increases exponentially at higher frequencies, where the noise is less harmful (Figure 2.8). By using this noise shaping, the total quantization noise stays the same, but the signal-to-noise ratio in the base band is increased.

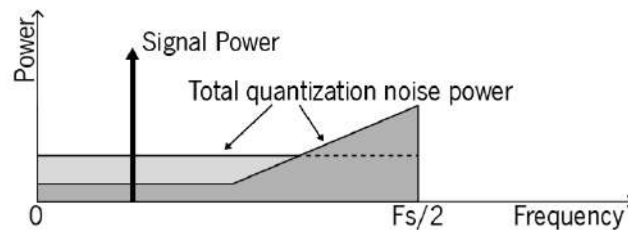

Figure 2.8: Noise shaping of low frequency noise to high frequencies.

To achieve the shaping of the noise, sigma-delta modulators use an error minimizing feedback loop, where the input signal *(u)* is compared with the quantized output signal *(y)*, and the difference between the signals is frequency weighted [2.21]. Differences within the signal band are carried to the output without attenuation, while the loop filter suppresses differences at other frequencies, and its resulting output is fed to the quantizer where the next output value *(y)* is generated (Figure 2.9). This results in a close match between the input and quantized output signals within the filter pass-band, and the shaping of the quantization noise to frequencies that are outside of the interest band of the signal.

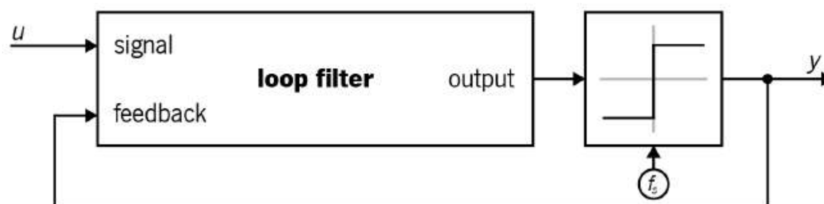

Figure 2.9: Generic model of sigma-delta noise shaping loop.

As previously stated, one of the main applications of sigma-delta modulation is to implement high-performance ADCs. In Figure 2.10 a) a basic sigma-delta modulator used for this purpose is depicted. It is a feedback loop with an integrator in the feedforward path (acting as the loop filter), an ADC used as the quantizer, and a digital-to-analog converter (DAC) used in the feedback path. This results in a nonlinear system, due to the quantizing effect of the ADC, and on a dynamic system, due to the memory properties of the integrator, making its mathematical analysis a difficult task. However, a simplified analysis can be performed by linearizing the ADC (unity gain and an additive quantization noise *e*), and assuming a perfect operation of the DAC with a reference voltage of 1 V and a sampling rate *(fs)*

of 1 Hz, resulting on the discrete-time linear system presented in Figure 2.10 b). Thus, it can be shown that the output signal at a time n ($t = n/f_s$) is:

$$y(n) = u(n-1) + e(n) - e(n-1) . \tag{2.19}$$

This means that the output signal y has a delayed, yet unaltered, replica of the analog input signal u, and a differentiated version of the quantization noise e. It is known that the modulation does not affect the signal and that the differentiation of the error reduces it for smaller frequencies when compared with the sampling ratio [2.22]. Additionally, the loop filter typically has a high gain in the signal band, strongly attenuating the in-band quantization noise, creating the noise shaping. Furthermore, the ADC nonlinearity is merged with the quantization error, being suppressed along with the quantization noise for the signal band. However, the nonlinearity of the DAC affects the output signal, limiting the performance of the system. The simplest way of mitigating this issue is to use single-bit quantization, transforming the input/output of the DAC in only two levels, thus making it inherently linear. Digital correction or dynamic techniques can also be used for multi-bit quantization.

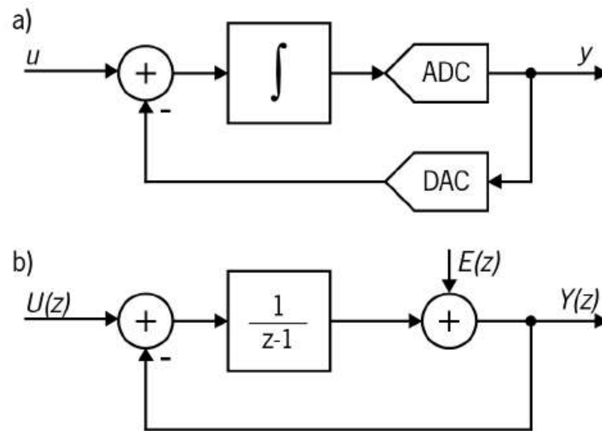

Figure 2.10: a) Block diagram of a sigma-delta modulator used as an ADC; b) Z-domain linear model of a sigma-delta modulator used as an ADC.

The quantization noise in the sigma-delta modulator is:

$$q(n) = e(n) - e(n-1) , \tag{2.20}$$

and in the z domain it becomes:

$$Q(z) = (1 - z^{-1})E(z) . \tag{2.21}$$

In the frequency domain, after replacing z by $e^{j2\pi fT}$, the power spectral density (PSD) of the output noise is given by:

$$S_q(f) = (2\sin(\pi fT))^2 S_e(f) , \tag{2.22}$$

where T is the sampling period $(T = 1/f_s)$, and $S_e(f)$ is the 1-sided PSD of the quantization noise of the ADC. For rapidly and randomly varying input signals, e may be approximated to white noise of mean-square value $e_{rms}^2 = \Delta^2 / 12$, where Δ is the step size of the quantizer. Thus:

$$S_e(f) = \frac{\Delta^2}{6f_s}. \tag{2.23}$$

The OSR defines the ratio between the sampling frequency of the signal and the Nyquist frequency, and is given by:

$$OSR = \frac{f_s}{2f_B}, \tag{2.24}$$

where f_B is the signal maximum frequency (bandwidth upper limit). Integrating $S_q(f)$ between 0 and f_B, the in-band noise power can be determined. Assuming OSR>>1, a good approximation is:

$$q_{rms}^2 = \frac{\pi^2 e_{rms}^2}{3(OSR)^3}. \tag{2.25}$$

As expected, the in-band noise power reduces as the OSR is increased. Nevertheless, the reduction is slow: doubling the oversampling ratio only reduces the noise by 9 dB, increasing the resolution by only approximately 1.5 bits [2.22]. If single-bit quantization is used, for an OSR of 256, the resolution will be less than 13 bits.

One method to increase the resolution of the sigma-delta modulator is to increase the order of the loop filter by adding another integrator and feedback path to the circuit of Figure 2.10, resulting in the circuit shown in Figure 2.11. Linearizing, one gets:

$$Y(z) = z^{-1}U(z) + (1 - z^{-1})^2 E(z). \tag{2.26}$$

Following the same method as previously, the in-band noise power is (to a good approximation for OSR>>1):

$$q_{rms}^2 = \frac{\pi^4 e_{rms}^2}{5(OSR)^5}. \tag{2.27}$$

For the same conditions of the first-order sigma-delta modulator, a 19-bit resolution can be achieved, increasing 2.5 bits when OSR is doubled [2.22].

Theoretically, higher-order modulators can be achieved by adding more integrators and feedback paths. For an Lth-order loop, the in-band noise power can approximately be defined by (2.28), and doubling the OSR increases the resolution by L+0.5 bits [2.22]. However, for high-order loops, stability issues (ignored until now) reduce significantly the achievable resolution.

$$q_{rms}^2 = \frac{\pi^{2L} e_{rms}^2}{(2L+1)(OSR)^{2L+1}}. \tag{2.28}$$

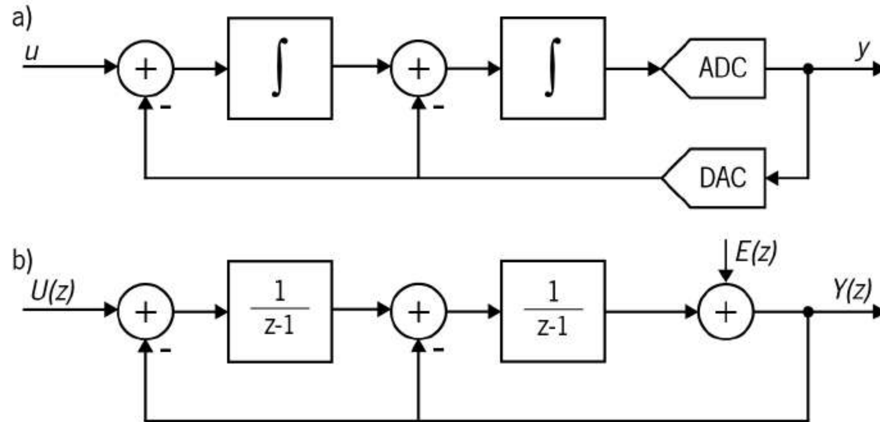

Figure 2.11: a) Block diagram of a second-order sigma-delta modulator used as an ADC; b) Z-domain linear model of a second-order sigma-delta modulator used as an ADC.

2.2.2. Electromechanical sigma-delta modulation

Including a MEMS sensor element (an accelerometer in this case) in a sigma-delta modulator realizes an electromechanical sigma-delta modulator, where the second-order mechanical integrators provide the desired noise shaping. The typical architecture, presented in Figure 2.12, is composed of several blocks: i) the sensor element; ii) the readout circuit; iii) a phase compensator; iv) the loop filter; v) a sampled 1-bit quantizer; and vi) electrostatic force feedback [2.23].

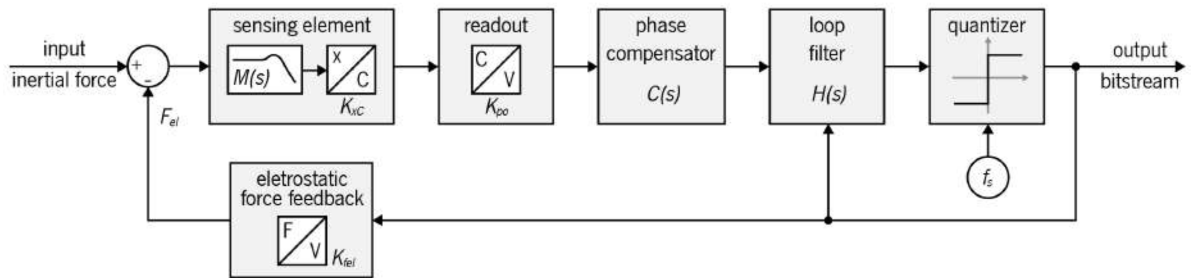

Figure 2.12: Generic block diagram of an electromechanical sigma-delta modulator.

The sensor element consists of a suspended proof-mass, which is displaced by an external acceleration, and it can be modeled as a mass-spring-damper system (behavior was explained in section 2.1). As stated, the sensor can be approximated as a second-order system with the transfer function *M(s)* (equation (2.29)). Additionally, the displacement change of the sensor is translated into a capacitance variation, and the K_{xc} gain can be determined by (2.2). For a more comprehensive model, the mechanical Brownian noise *(N_b)* of the sensor element should also be considered.

$$M(s) = \frac{1}{ms^2 + bs + k}. \tag{2.29}$$

The readout circuit is responsible for reading the capacitance variation due to external acceleration forces and converting it into a voltage. A simplistic yet effective way of modeling this consists of using the capacitance to voltage gain *(K_{po})* and adding a white noise block *(N_e)*, which models the thermal noise of the readout electronics [2.23].

The sensing element, and possibly the readout circuitry, will introduce a phase delay in the signal, so a phase compensator is necessary (it may not be needed for overdamped sensors) [2.23]. This circuit will enable a phase lead at lower frequencies, which will compensate the signal phase. A simple phase compensator can be described by:

$$C(s) = \frac{s+z}{s+p}, \tag{2.30}$$

where z and p can be defined by (2.31) and (2.32), respectively. Additionally, ω_m represents the frequency of maximum phase lead, and ϕ_m is the phase lead at that frequency [2.24].

$$z = \omega_m \frac{1-\sin(\phi_m)}{\cos(\phi_m)}, \tag{2.31}$$

$$p = \omega_m \frac{1+\sin(\phi_m)}{\cos(\phi_m)}. \tag{2.32}$$

To quantize the signal, a discrete-time quantizer is used. Typically, to address nonlinearity issues, an one-bit quantizer is preferred. This can be implemented using a common comparator, which digitalizes the signal and outputs a ±1 "digital" signal, called bitstream. In the z domain, the linear model (assuming a small proof-mass deflection) can be represented as the quantizer equivalent gain *(K_q)*, and once it introduces quantization error, an additional noise source *(N_q)* should be added.

The feedback consists of a one-bit DAC, which is continuously electrostatically actuating the MEMS element either with a positive or negative electrostatic force *(F_{el})*, depending on the comparator output. The feedback gain *(K_{fel})* can be derived from (2.18), and is given by:

$$K_{fel} = \frac{V_A^{\,2} C_{A0} d_0}{2 d_0^{\,2}}. \tag{2.33}$$

Additionally, the choice of actuation voltage is important since it limits the dynamic range of the sensor [2.23]. This can be seen as an advantage of closed-loop operation since the dynamic range is not limited by the spring constant and mass of the sensor element, as it is with open-loop operation. To extend the dynamic range, the electrostatic force needs to be at least equal to the inertial force *(F_{acc})*. Using the steady

state force balance equation (2.34), it is possible to obtain the minimum actuation voltage required for a maximum acceleration of a_{max}.

$$F_{el} = F_{acc} \Leftrightarrow \frac{V_A^{\,2} C_{A0} d_0}{2 d_0^{\,2}} = m a_{max} \Leftrightarrow V_A = \sqrt{\frac{2 d_0^{\,2} m a_{max}}{C_{A0} d_0}} . \tag{2.34}$$

Finally, the loop filter can be implemented using several integrators and feedback or feedforward loops. As stated, this block will perform the desired noise shaping, and its transfer function *H(s)* will vary accordingly to the filter's architecture. Since the MEMS sensor acts as a second-order mechanical integrator, it can also provide limited noise shaping. Thus, the simplest system architecture is a second-order electromechanical sigma-delta modulator, where *H(s)* is simplified to the unity, and its feedback loop is not present [2.23], [2.25]. The model of a second-order electromechanical sigma-delta modulator is depicted in Figure 2.13.

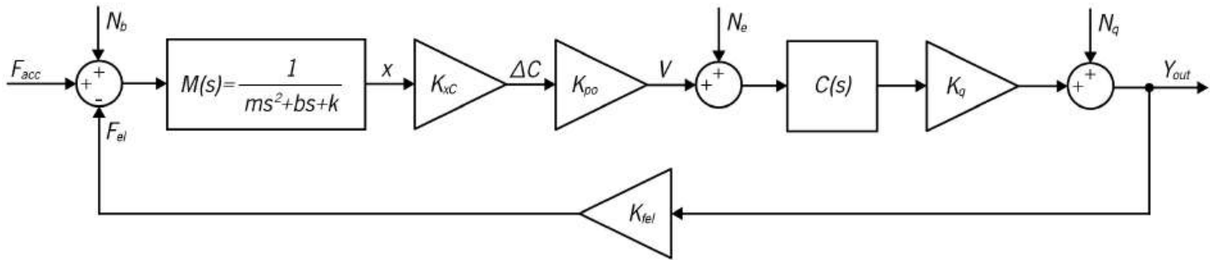

Figure 2.13: Model of a second-order electromechanical sigma-delta modulator.

The resultant signal transfer function *(STF)*, quantization noise transfer function *(NTF_Q)*, electronic readout noise transfer function *(NTF_E)*, and Brownian noise transfer function *(NTF_B)* are given by (2.35), (2.36), (2.37), and (2.38), respectively. Since the signal transfer function is flat in the interest band, the signal can pass through unchanged. Additionally, the quantization noise transfer function has low gain in the signal band and high gain at higher frequencies, providing the desired noise shaping [2.26].

$$STF = \frac{Y_{out}}{F_{acc}} = \frac{K_{xC} K_{po} K_q C(s)}{ms^2 + bs + (k - K_{xC} K_{po} K_q K_{fel} C(s))} , \tag{2.35}$$

$$NTF_Q = \frac{Y_{out}}{N_q} = \frac{1}{1 + K_{fel} M(s) K_{xC} K_{po} C(s) K_q} , \tag{2.36}$$

$$NTF_E = \frac{Y_{out}}{N_E} = \frac{C(s) K_q}{1 + K_{fel} M(s) K_{xC} K_{po} C(s) K_q} , \tag{2.37}$$

$$NTF_B = \frac{Y_{out}}{N_B} = \frac{M(s) K_{xC} K_{po} C(s) K_q}{1 + K_{fel} M(s) K_{xC} K_{po} C(s) K_q} . \tag{2.38}$$

In order to improve system performance, a high signal-to-noise ratio is desirable. To achieve this, the quantization noise *(N_q)* should be, at least, one order of magnitude lower than the Brownian noise *(N_b)* and electronic noise *(N_e)* levels [2.27]. To realize high quantization noise suppression in the signal band, high low-frequency gain is required. On pure electronic sigma-delta modulators, because the loop is composed of near-ideal integrators, the low frequency gain is high, resulting in good noise shaping attributes. However, on an electromechanical sigma-delta modulator, the low-frequency gain is equal to the inverse of the spring constant of the MEMS element, limiting the noise shaping behavior. Moreover, the noise introduced by the readout circuit will not be subjected to any noise shaping, further limiting the achievable performance of the second-order electromechanical sigma-delta modulator. Thus, to improve the SNR, one can use higher-order electromechanical sigma-delta modulators by adding additional electronic filters in the loop leading to higher-order noise shaping in the signal band [2.25], [2.26].

One of the most common architectures for higher-order electromechanical sigma-delta modulators is the cascade integrator with distributed feedback. It is composed of one or more cascaded delaying integrators with feedback loops, both scaled by coefficients (K_{io} for the integrators and K_{fio} for the feedback signal, where *io* stands for integration order). This feedback topology bypasses the mechanical sensing element, consequently contributing with compensating zeros (dependent on gain values and sensor parameters). Such architecture enables a larger SNR, since the noise shaping is determined not only by the sensor element but also by the electronic filter, and noise shaping of electronic noise is also possible. However, some challenges are still present, such as the impossibility to access the internal nodes of the sensing element and the need to optimize the electronic loop filter gains to achieve stability and improve the performance of the system. Figure 2.14 depicts the model for a third-order electromechanical sigma-delta modulator with a cascade integrator with distributed feedback architecture.

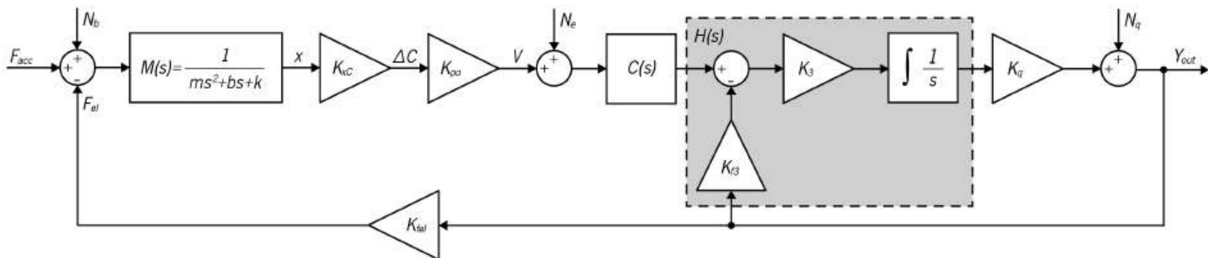

Figure 2.14: Model of a third-order electromechanical sigma-delta modulator with cascade integrator with distributed feedback architecture.

To achieve higher-modulation orders (4th, 5th, etc.), it is possible to keep cascading integrators and distributed feedback signals to achieve the desired order. The signal transfer function *(STF)*, quantization noise transfer function *(NTF_Q)*, electronic readout noise transfer function *(NTF_E)*, and Brownian noise

transfer function *(NTF_B)* for this cascade architecture are given by (2.39), (2.40), (2.41), and (2.42), respectively:

$$STF = \frac{Y_{out}}{F_{acc}} = \frac{K_{xC}K_{po}K_qC(s)H(s)}{ms^2 + bs + (k - K_{xC}K_{po}K_qK_{fel}C(s)H(s))}, \tag{2.39}$$

$$NTF_Q = \frac{Y_{out}}{N_q} = \frac{1}{1 + K_{fel}M(s)K_{xC}K_{po}C(s)H(s)K_q}, \tag{2.40}$$

$$NTF_E = \frac{Y_{out}}{N_E} = \frac{C(s)H(s)K_q}{1 + K_{fel}M(s)K_{xC}K_{po}C(s)H(s)K_q}, \tag{2.41}$$

$$NTF_B = \frac{Y_{out}}{N_B} = \frac{M(s)K_{xC}K_{po}C(s)H(s)K_q}{1 + K_{fel}M(s)K_{xC}K_{po}C(s)H(s)K_q}, \tag{2.42}$$

where, for the third-order electromechanical sigma-delta modulator, the loop-filter transfer function is:

$$H(s) = \frac{K_3}{s + K_{f3}K_3K_q} \tag{2.43}$$

More complex architectures, including extra feedback and feedforward loops, are also possible, aiming for improvement of the SNR. A comparative study between sigma-delta modulator architectures was performed and presented in [2.28] and [2.29]. However, the more complex architectures exhibit no significative improvements over the cascading modulators, but introduce additional complexity to the system, making it more difficult to obtain a stability. Thus, on the context of this thesis, only cascading modulators are addressed.

2.3. Nonlinearities

Capacitive MEMS accelerometers have some inherent nonlinearities due to their physical properties. An example of this is the relation between the capacitance and the displacement of the proof-mass, which is not linear. According to (2.17), one can determine the left, right, and differential capacitances for a given displacement. In Figure 2.15, the resulting capacitance of a capacitor with a plate length of 100 μm, a width of 20 μm, and a gap of 2 μm, using air as the dielectric, for displacement values ranging from 0 to 1.5 μm, is depicted. As illustrated, a linear relation can only be assumed for small proof-mass displacements.

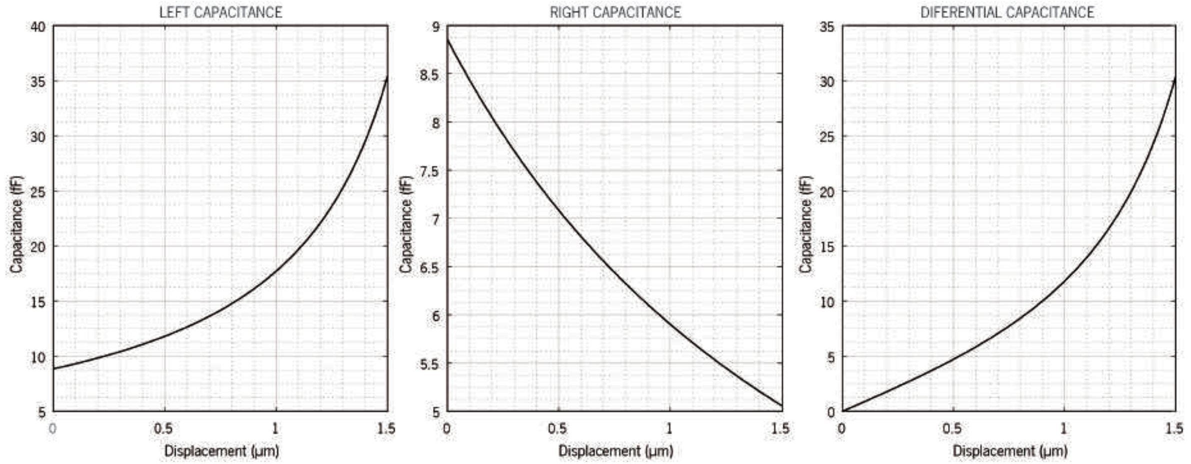

Figure 2.15: Relation between capacitance and proof-mass displacement.

Additionally, the electrostatic force also has a nonlinear relation with the proof-mass displacement. By using (2.18), the electrostatic force was determined for the previous electrode dimensions, using $V_A = 3.3$ V, and the result is depicted in Figure 2.16. Once again, a linear relation can only be assumed for small proof-mass displacements. In an electromechanical sigma-delta modulator, these nonlinearities can be easily mitigated by using a one-bit quantization schema. This means that both the capacitance and the electrostatic force will only assume two discrete values, inherently eliminating these nonlinearities [2.22].

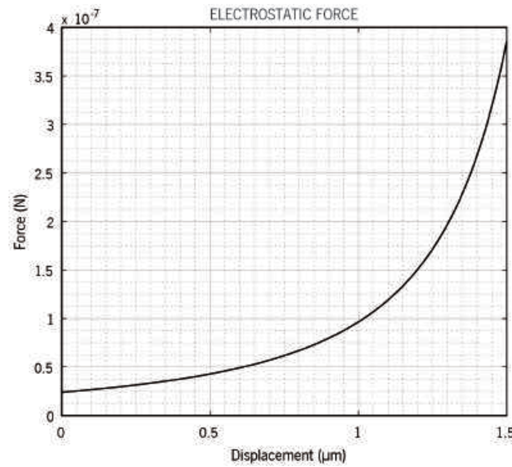

Figure 2.16: Relation between electrostatic force and proof-mass displacement.

MEMS devices have typical features of only a few micrometers in size separated by gaps of the same scale. At this scale, the squeeze film damping is one of the dominating factors of the devices' dynamic response. Using expression (2.15), previously established for determining the damping coefficient, and applying the electrodes defined before with an air pressure *(P_0)* of 140 Pa at 25 °C, one can obtain the damping coefficient as a function of displacement, depicted in Figure 2.17, showing that *b* is not a constant and can only be assumed linear for small proof-mass displacement.

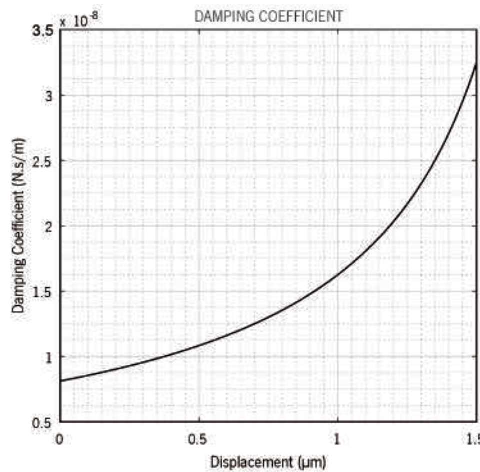

Figure 2.17: Relation between the damping coefficient and proof-mass displacement.

However, the MEMS accelerometer will be operated in an electromechanical sigma-delta modulator. It is known that this technique provides the desired small proof-mass displacement [2.25], which significantly reduces the effect of this nonlinearity.

Additional nonlinear effects, namely the pull-in effect and the temperature dependency, are also present in the system. These nonlinearities are explained in more detail in sections 2.3.1 and 2.3.2, respectively.

2.3.1. Pull-in effect

The pull-in effect is known since 1967 when the resonant gate transistor was introduced [2.30]. While dealing with MEMS devices with parallel-plate electrostatic actuation, this nonlinearity must always be considered since it is one of the most significant phenomena of this type of actuators [2.31]. Taking into consideration the typical design of parallel-plate electrostatic actuators, where there are two electrodes, one fixed and one movable (anchored by a mechanical spring), when a voltage is applied between them, an electrostatic force is created (according to (2.18)), attracting the electrodes. This force is counteracted by the elastic force of the mechanical spring, which is linear with deflection (equation (2.3)). For low actuation voltage (V_A) values, the mechanical spring is able to counteract the electrostatic force, resulting in an equilibrium, being this condition typically valid for displacements until 1/3 of the gap between electrodes at rest position (d_0). For higher actuation voltages, where the displacement is larger than this critical point, the electrostatic force is such that the mechanical spring elastic force cannot counteract it, leading to system instability. When this happens, the capacitor electrodes snap together, being this known as the pull-in effect [2.32]. The voltage needed to reach this critical deflection (x_{pi}) is called pull-in voltage (V_{pi}) and can be calculated using (2.44). A graphical representation of the pull-in phenomenon is presented in Figure 2.18, demonstrating the stable motion of the device until the critical point, and the instability beyond the critical deflection.

$$V_{pi} = \sqrt{\frac{8{d_0}^3 k}{27\varepsilon A}} \tag{2.44}$$

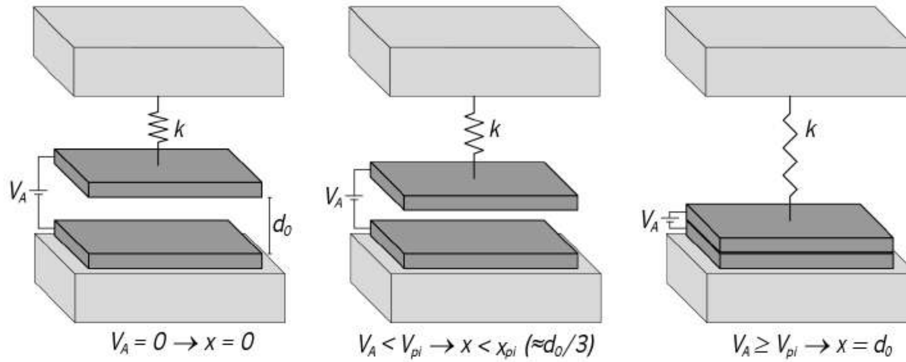

Figure 2.18: Representation of the pull-in phenomenon.

The pull-in phenomenon should be avoided for various reasons [2.33]. It leads to instability of the system, making the realization of a useful system hard to achieve. Additionally, the snapping of the electrodes together can lead to stiction, and in some cases, to device destruction. To avoid electrode snapping, mechanical stoppers should be added to the device, ensuring that the electrodes cannot touch each other, even in a pull-in event.

2.3.2. Temperature dependence

Capacitive MEMS devices exhibit a temperature dependence that can be explained by two main factors: silicon thermal expansion, and the variation of the Young modulus with temperature. Knowing that the thermal expansion coefficient of silicon (α) is positive (with a temperature rise the dimensions expand), increasing the temperature leads to an increase of the dimensions of the electrodes and a decrease in the gap between them (Figure 2.19). Thus, both the capacitance of the electrodes and the electrostatic force will vary with temperature.

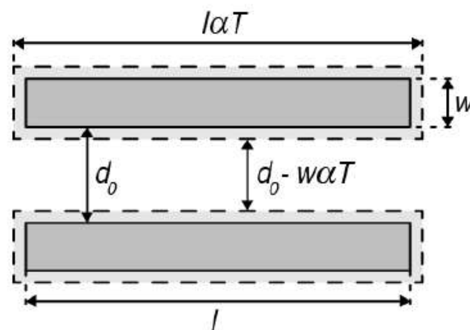

Figure 2.19: Parallel-plate dimensions changing with thermal expansion.

Accounting for the temperature effects, the capacitance of the electrodes is given by (2.45), while the electrostatic force can be obtained using (2.46).

$$C_0(T) = \varepsilon \frac{A(1 + 2\alpha T)}{d_0 - w\alpha T} \tag{2.45}$$

$$F_{elec}(T) = \frac{V^2 C_{A0}(d_0 - w\alpha T)}{2(d_0 - w\alpha T)^2} \tag{2.46}$$

Regarding the thermal dependence of the Young modulus, Hopcroft has demonstrated that silicon has a coefficient of -60 ppm/°C [2.34], and Cho measured a temperature coefficient of -78.8 kPa/°C, -97.8 kPa/°C, and -131 kPa/°C, for orientations (100), (010), and (110), respectively [2.35]. This means that with an increase of temperature, the silicon Young modulus will decrease, affecting the elastic coefficient of the mechanical springs, and consequently, the elastic force of the system. Additionally, the mechanical springs are also affected by thermal expansion, therefore considering that the Young modulus thermal coefficient is represented by β, the elastic coefficient becomes:

$$k(T) = k(1 + (\alpha + \beta)T)\,. \tag{2.47}$$

To reduce these effects, one can design a sensor with a symmetric layout and, by using a differential operation method, significantly reduce the undesired temperature dependence.

2.4. Conclusions

In this chapter, the theoretical background required to design and model an electromechanical sigma-delta modulator to achieve a MEMS accelerometer encapsulated in vacuum was described, and its major characteristics, advantages and drawbacks were identified. First, the one degree of freedom model for a capacitive MEMS accelerometer was explained, including its dynamics and electrical characteristics. The damping model, essential to comprehend the MEMS dynamics and challenging to obtain for low-pressure devices, was established through experimental data. Additionally, a proposal for differential operation was suggested.

The closed-loop operation was also described, starting with the fundamental principles of the sigma-delta modulation technique and its historical contextualization. The sigma-delta modulator used in state-of-the-art ADCs was presented, and the use of higher modulation orders was described. After, the integration of the MEMS element in the sigma-delta modulator loop was proposed. The fundamental

blocks to achieve an electromechanical sigma-delta modulator were introduced, and the model and transfer functions for second and higher-order modulators were presented and discussed.

It is known that electrostatically actuated MEMS devices suffer from several nonlinearities. Thus, the nonlinear relation between the proof-mass displacement and variations in capacitance, electrostatic force, and damping coefficient were addressed. Moreover, the pull-in effect and the thermal dependence of these devices were explained.

References

[2.1] L. K. Baxter, *Capacitive Sensors: Design and Applications*. Wiley-IEEE Press, 1996.

[2.2] M. Gad-el-Hak, “The Fluid Mechanics of Microdevices—The Freeman Scholar Lecture,” *J. Fluids Eng.*, vol. 121, no. 1, pp. 5–33, Mar. 1999.

[2.3] L. Mol, L. A. Rocha, E. Cretu, and R. F. Wolffenbuttel, “Squeezed film damping measurements on a parallel-plate MEMS in the free molecule regime,” *J. Micromechanics Microengineering*, vol. 19, no. 7, p. 074021, Jul. 2009.

[2.4] M. Bao, H. Yang, H. Yin, and Y. Sun, “Energy transfer model for squeeze-film air damping in low vacuum,” *J. Micromechanics Microengineering*, vol. 12, no. 3, p. 322, May 2002.

[2.5] S. Hutcherson and W. Ye, “On the squeeze-film damping of micro-resonators in the free-molecule regime,” *J. Micromechanics Microengineering*, vol. 14, no. 12, pp. 1726–1733, Dec. 2004.

[2.6] T. B. Gabrielson, “Mechanical-thermal noise in micromachined acoustic and vibration sensors,” *IEEE Trans. Electron Devices*, vol. 40, no. 5, pp. 903–909, May 1993.

[2.7] F. Chen, W. Yuan, H. Chang, I. Zeimpekis, and M. Kraft, “Low noise vacuum MEMS closed-loop accelerometer using sixth-order multi-feedback loops and local resonator sigma delta modulator,” in *IEEE 27th International Conference on Micro Electro Mechanical Systems (MEMS)*, 2014, pp. 761–764.

[2.8] H. Xu, X. Liu, and L. Yin, “A closed-loop ΣΔ interface for a high-Q micromechanical capacitive accelerometer with 200 ng/√Hz input noise density,” *IEEE J. Solid-State Circuits*, vol. 50, no. 9, pp. 2101–2112, Sep. 2015.

[2.9] Y. Dong, P. Zwahlen, A. M. Nguyen, R. Frosio, and F. Rudolf, “Ultra-high precision MEMS accelerometer,” in *16th International Solid-State Sensors, Actuators and Microsystems Conference*, 2011, pp. 695–698.

[2.10] P. Zwahlen, A.-M. Nguyen, Y. Dong, F. Rudolf, M. Pastre, and H. Schmid, “Navigation grade MEMS accelerometer,” in *IEEE 23rd International Conference on Micro Electro Mechanical Systems (MEMS)*, 2010, pp. 631–634.

[2.11] Jiangfeng Wu and L. R. Carley, “Electromechanical ΔΣ modulation with high-Q micromechanical accelerometers and pulse density modulated force feedback,” *IEEE Trans. Circuits Syst. I Regul.*

Pap., vol. 53, no. 2, pp. 274–287, Feb. 2006.

[2.12] R. Wilcock and M. Kraft, "Genetic Algorithm for the Design of Electro-Mechanical Sigma Delta Modulator MEMS Sensors," *Sensors*, vol. 11, no. 12, pp. 9217–9232, Sep. 2011.

[2.13] Z. Meimei, Q. Haiyang, and Z. Fuqiang, "Comparisons of Feed-Forward and Multiple-Feedback Sigma-Delta Modulators for MEMS Accelerometers," *MATEC Web Conf.*, vol. 56, p. 08003, Apr. 2016.

[2.14] C. C. Cutler, "Differential quantization of communication signals," US2605361A, 1952.

[2.15] D. E. Maurice and D. Boris, "Communication system utilizing constant amplitude pulses of opposite polarities," US2629857A, 1953.

[2.16] F. de Jager, "Delta modulation — a method of PCM transmission using the one unit code," *Philips Res. Reports*, vol. 7, pp. 442–466, 1952.

[2.17] C. C. Cutler, "Transmission systems employing quantization," US2927962A, 1954.

[2.18] H. Inose, Y. Yasuda, and J. Murakami, "A Telemetering System by Code Modulation - Δ-Σ Modulation," *IRE Trans. Sp. Electron. Telem.*, vol. SET-8, no. 3, pp. 204–209, Sep. 1962.

[2.19] D. J. Goodman, "The Application of Delta Modulation to Analog-to-PCM Encoding," *Bell Syst. Tech. J.*, vol. 48, no. 2, pp. 321–343, Feb. 1969.

[2.20] J. Candy, "A Use of Limit Cycle Oscillations to Obtain Robust Analog-to-Digital Converters," *IEEE Trans. Commun.*, vol. 22, no. 3, pp. 298–305, Mar. 1974.

[2.21] E. Janssen and A. van Roermund, *Look-Ahead Based Sigma-Delta Modulation*. Dordrecht: Springer Netherlands, 2011.

[2.22] R. Schreier and G. C. Temes, *Understanding Delta-Sigma Data Converters*, vol. 53, no. 9. Wiley-IEEE Press, 1997.

[2.23] T. Bechtold, G. Schrag, and L. Feng, *System-Level Modeling of MEMS*, vol. 10. Weinheim, Germany: Wiley-VCH Verlag GmbH & Co. KGaA, 2013.

[2.24] W. Messner, "Formulas for asymmetric lead and lag compensators," in *2009 American Control Conference*, 2009, pp. 3769–3774.

[2.25] F. Chen, X. Li, and M. Kraft, "Electromechanical Sigma-Delta Modulators (ΣΔM) Force Feedback Interfaces for Capacitive MEMS Inertial Sensors: A Review," *IEEE Sens. J.*, vol. 16, no. 17, pp. 6476–6495, Sep. 2016.

[2.26] M. Kraft and Y. Dong, "Higher Order Sigma-Delta Modulators Interfaces for Capacitive Inertial Sensors," in *NATO Science for Peace and Security Workshop*, 2007.

[2.27] H. Kulah, Junseok Chae, and K. Najafi, "Noise analysis and characterization of a sigma-delta capacitive silicon microaccelerometer," in *TRANSDUCERS '03. 12th International Conference on Solid-State Sensors, Actuators and Microsystems. Digest of Technical Papers (Cat. No.03TH8664)*, 2003, vol. 1, no. 2, pp. 95–98.

[2.28] V. Lima, N. Brito, F. S. Alves, J. Cabral, J. Gaspar, and L. A. L. A. Rocha, “Performance Comparison of Sigma-delta Modulator Architectures for MEMS Accelerometers Using a Fully-Digital Approach,” *Procedia Eng.*, vol. 168, no. C, pp. 814–817, 2016.

[2.29] V. Lima, N. Brito, J. Cabral, J. Monteiro, J. Gaspar, and L. A. Rocha, “Digital platform for Sigma-Delta accelerometer assessment and test,” *Microsyst. Technol.*, vol. 24, no. 5, pp. 2265–2276, May 2018.

[2.30] H. C. Nathanson, W. E. Newell, R. A. Wickstrom, and J. R. Davis, “The resonant gate transistor,” *IEEE Trans. Electron Devices*, vol. 14, no. 3, pp. 117–133, Mar. 1967.

[2.31] M. Rahaeifard and M. T. Ahmadian, “On pull-in instabilities of microcantilevers,” *Int. J. Eng. Sci.*, vol. 87, pp. 23–31, Feb. 2015.

[2.32] E. Cretu, L. A. Rocha, and R. F. Wolffenbuttel, “Using the Pull-In Voltage as Voltage Reference,” in *Transducers ’01 Eurosensors XV*, Berlin, Heidelberg: Springer Berlin Heidelberg, 2001, pp. 678–680.

[2.33] S. Rudra *et al.*, “Static and dynamic characterization of pull-in protected CMOS compatible poly-SiGe grating light valves,” *Sensors Actuators A Phys.*, vol. 179, pp. 283–290, Jun. 2012.

[2.34] M. A. Hopcroft, W. D. Nix, and T. W. Kenny, “What is the Young’s Modulus of Silicon?,” *J. Microelectromechanical Syst.*, vol. 19, no. 2, pp. 229–238, Apr. 2010.

[2.35] C.-H. Cho, “Characterization of Young’s modulus of silicon versus temperature using a ‘beam deflection’ method with a four-point bending fixture,” *Curr. Appl. Phys.*, vol. 9, no. 2, pp. 538–545, Mar. 2009.

3. Integrated system implementation

A prototype for the proposed accelerometer was designed and implemented in order to experimentally evaluate its behavior and performance. As stated, the planned approach is based on the inclusion of the sensor element within a sigma-delta modulator, providing the electrostatic damping required for low-pressure sensors, and enabling the realization of a high-performance MEMS accelerometer in low pressure. The typical method consists of implementing the additional blocks (when compared with an open-loop methodology) using discrete circuitry [3.1]–[3.5]. However, some authors propose a more flexible implementation, using field-programmable gate arrays (FPGAs) to realize the higher-order filters and phase compensator [3.6]–[3.8]. This approach is advantageous, since it allows an experimental fine-tuning of the loop parameters at the final trim of the devices, aiming to achieve stability of the loop, more difficult for low-damping devices, and to improve the performance of the system. Typically, this process is performed by simulation [3.9]. However, these simulations can be time consuming and are susceptible to errors due to fabrication process tolerances. Nonetheless, a simulation model of the complete system was also developed to enable a proper validation of the proposed system operation.

Taking into consideration the aforementioned characteristics, the proposed electromechanical sigma-delta modulator was implemented in FPGA, and Figure 3.1 presents its architecture and all the fundamental blocks.

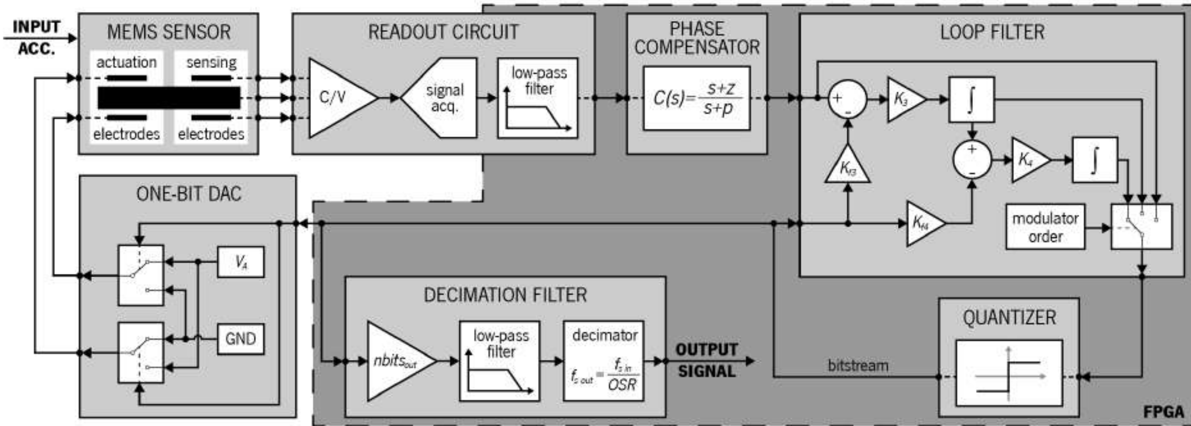

Figure 3.1: Block diagram of the system.

In this chapter, the implementation of all the blocks will be discussed and described in detail, starting with the features, characteristics, and microfabrication of the MEMS accelerometer. After, the analog readout circuitry, composed by a capacitance to voltage (C/V) converter (C/V ASIC [3.10]), a signal acquisition block, together with the digital low-pass filter, which was implemented in the FPGA Programmable Logic (PL), were examined. The phase compensation, required to reduce the delay introduced by the MEMS sensor and readout circuitry, was also implemented in Verilog in the target FPGA, as well as the loop filter. The filter architecture enables the selection of three different modulation orders (second, third, and fourth), and the details of their implementation are also described. The one-bit quantizer was also digitally implemented (in the FPGA) as a comparator without hysteresis that employs a switching circuit to provide left- and right-side actuation voltages to the MEMS sensor. The force feedback is handled by a one-bit DAC with a constant actuation voltage, and its control is similarly managed by the FPGA. Finally, to interpret the bitstream and obtain the readout signal in the baseband, the design and implementation of a decimation filter, composed by a low-pass filter and a decimation block, is discussed. Additionally, the architecture of the application software, implemented in the FPGA Processing System (PS) is also described in this chapter.

3.1. High-level simulation model

With the purpose of validating the implemented FPGA hardware and software design and assess the performance of the electromechanical sigma-delta modulator, a high-level simulation model was developed in Simulink. The model contemplates the MEMS accelerometer and its mechanical characteristics, the readout circuit and the 1-bit DAC using analog blocks, and the digital blocks to be implemented in the FPGA (IIR low-pass filter, phase compensator, high-order loop, 1-bit quantizer, and decimation filter). The model's high-level architecture is presented in Figure 3.2.

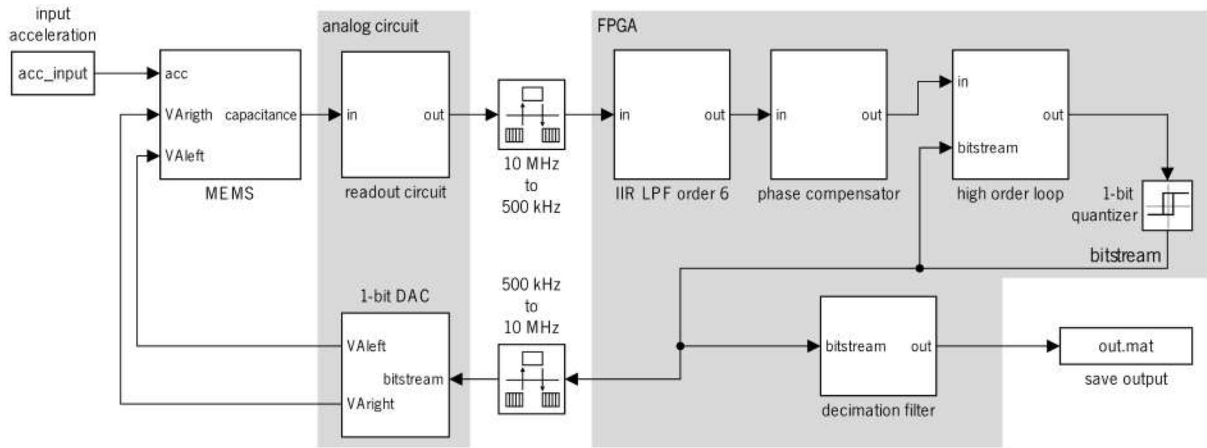

Figure 3.2: Simulink model of the electromechanical sigma-delta modulator.

The MEMS accelerometer model is composed of three components. First, the second-order mechanical system was implemented, where the acceleration force is added to the damping and elastic forces. The result is integrated two times, thus obtaining the displacement of the proof-mass. Regarding the damping model, the force was calculated using equation (2.16).

Another component of the MEMS sensor model is related to the electrostatic force feedback. The model implements the electrostatic force according to equation (2.18). However, due to the sensor layout, the applied force on the back gap (d_{02} = 11.6 µm) is subtracted from the force applied to the front gap (d_{01} = 1.6 µm). Thus, the resultant electrostatic force can be calculated by:

$$F_{el} = \frac{V_A^2 C_{A0} d_0}{2(d_{01} - x)^2} - \frac{V_A^2 C_{A0} d_0}{2(d_{02} + x)^2} \tag{3.1}$$

The third component of the MEMS element model implements the mechanical stopper. Here, the model verifies the proof-mass displacement, limiting its maximum value to the allowed by the mechanical stoppers, which was set to 1.2 µm.

Additionally, the MEMS accelerometer model adds the Brownian noise of the sensor to its displacement and converts the resultant value to capacitance. The complete MEMS accelerometer model is presented in Figure 3.3.

The readout circuit model is depicted in Figure 3.4. It is composed of the capacitance to voltage gain *(K_{P0})* of the C/V converter, the electrical noise of the converter (white noise source was used), and the ADC. This was implemented as a conversion gain (16-bit resolution using two's complement representation, and a voltage reference of 3.3 V), the 16 clock cycles of latency, and a rounding block at the output, which truncates the signal to 16-bit integer representation.

Figure 3.3: Simulink model of the MEMS accelerometer.

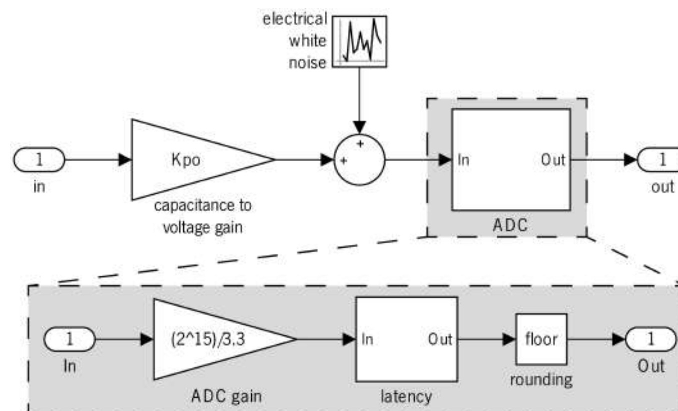

Figure 3.4: Simulink model of the readout circuit.

The digital blocks of the sixth-order IIR low-pass filter, phase compensator, and high-order loop were implemented according to the explanation given in the subsections 3.4.2, 3.4.3, and 3.4.4, respectively. Each model representation is also presented at each of the respective subsections.

The decimation filter is composed of the multiplication of the bitstream by the desired resolution, the low-pass filter, which has the same architecture as the signal low-pass filter, and a decimator to reduce the sampling frequency to the desired value (1 kHz). This model is depicted in Figure 3.5.

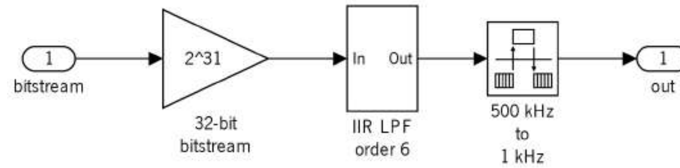

Figure 3.5: Simulink model of the decimation filter.

Finally, the 1-bit DAC model was implemented using the actuation voltage and two switches, in order to apply the voltage to the correct MEMS capacitor. The switches are controlled by the bitstream of the modulator. Additionally, the electrical noise of the actuation voltage was also incorporated into the system, using a white noise source. The correspondent model is depicted in Figure 3.6.

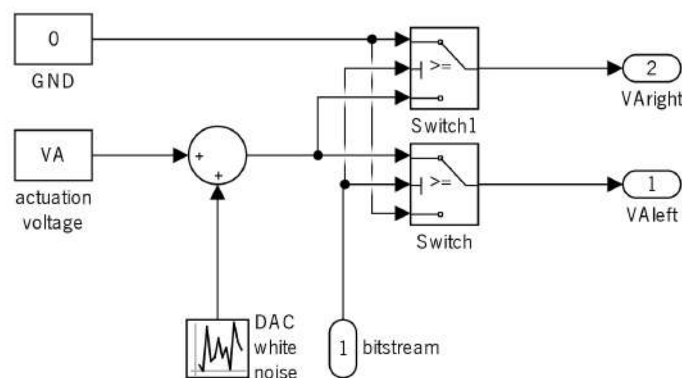

Figure 3.6: Simulink model of the 1-bit DAC.

3.2. MEMS sensor

To realize the proposed accelerometer, a MEMS sensor element must be designed and microfabricated. This is arguably one of the most important parts of the entire system, and its implementation is a nontrivial task, fortunately, the research group in which this thesis is inserted has a vast experience designing micromachined inertial sensors [3.11]–[3.15]. The typical approach is comprised of the design of the actual geometry of the sensor, using some computer aided design (CAD) tool (in this thesis Rhinoceros® and KLayout were used (Figure 3.7)) while simultaneously performing simulations of the device behavior, which can be high-level or finite element analysis (FEA).

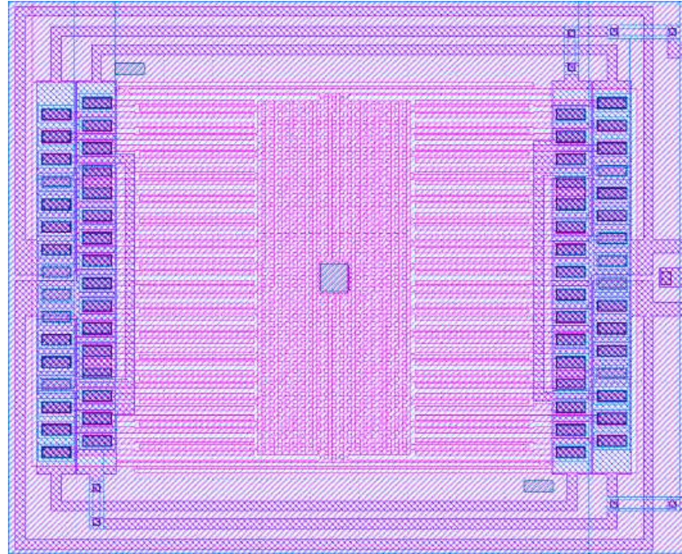

Figure 3.7: CAD layout of the designed MEMS accelerometer.

An analytical understanding of the system is essential, yet some aspects of the mechanical behavior of the MEMS element can pass undetected. To ensure that this does not happen, structural and modal finite element analysis were performed using ANSYS software. This enabled the verification of the correct behavior of the sensor element, as well as validating the analytical study. In Figure 3.8 is represented the performed structural analysis using this method.

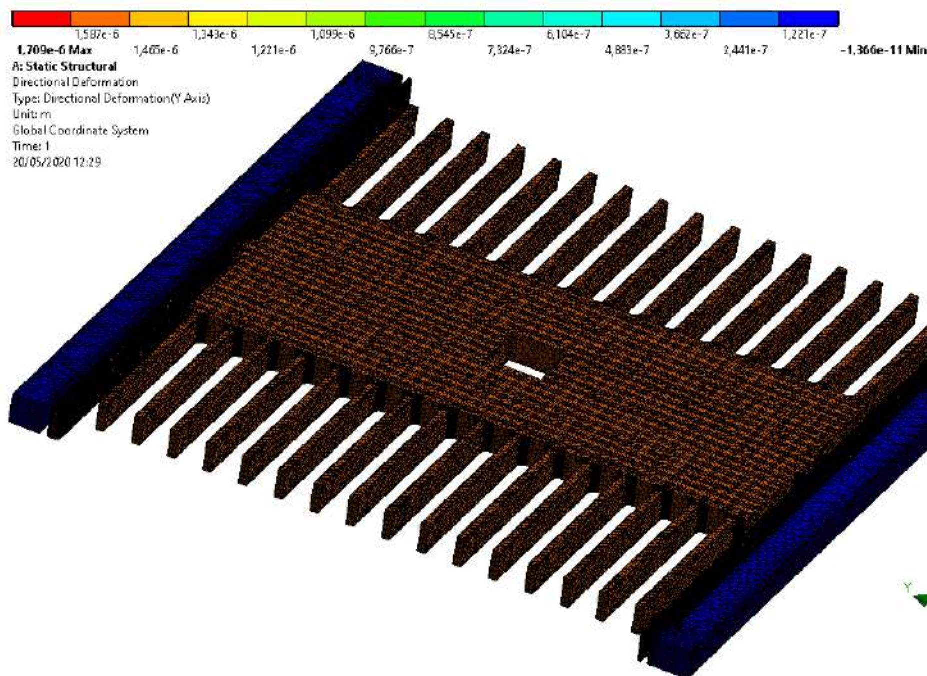

Figure 3.8: FEA structural simulation of the movable part of the sensor element.

The designed microstructures aim to maximize the sensitivity to external acceleration forces in one axis while suppressing the forces on the remaining axis, minimize the thermal-mechanical noise, and maximize the capacitance change due to proof-mass displacement. However, they must comply with all

the micromachining process rules, limitations, and characteristics. Additionally, a limit core size of approximately 400×400 μm² is required.

3.2.1. Microfabrication process

Since this work was performed in partnership with Bosch, the MEMS devices were fabricated using a Bosch standard silicon surface micromachining process available at Bosch Automotive Electronics, which enables a 19 μm thick active layer and two supplementary layers for electrical connections. Additionally, the micromachining process allows a wafer-level cap bonding, ensuring a stable encapsulation pressure of 140 Pa. The main fabrication steps are the typical ones for surface micromachining processes, previously explained in section 1.2.2. However, Bosch revolutionized the MEMS fabrication technology with the invention of silicon plasma etch, also known as the Bosch DRIE process (or just "the Bosch process"), which enables vertical etch of silicon with an aspect ratio of 1/20 [3.16]. The process consists of cycles of isotropic etching and deposition of a protection film, creating the desired vertical walls.

The working principle of Bosch's DRIE process is depicted in Figure 3.9, where the vertical walls are passivated by a Teflon-like layer (possibly octafluorocyclobutane (C_4F_8)), protecting the sidewalls during the etch cycle (Figure 3.9 c)); a low bias power is applied during an intermediate etch cycle in order to eliminate the passivation layer at the bottom of the trench by a vertical ion incidence (SF_x^+) (Figure 3.9 d)); and a cycle of isotropic etch is performed using sulfur hexafluoride (SF_6) (Figure 3.9 e)) [3.17]. By repetition of this cycle, the desired vertical walls are achieved (Figure 3.9 f)).

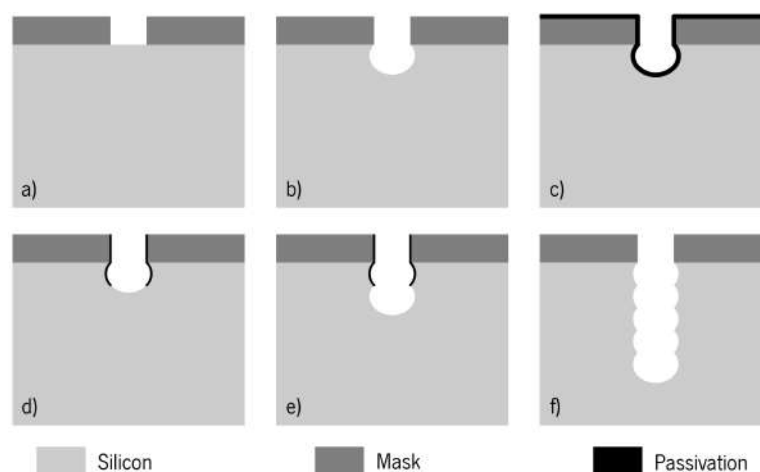

Figure 3.9: Working principle of Bosch's DRIE process, based on [3.17].

To achieve the desired high aspect ratio, both plasma cycles (SF_6 and C_4F_8) need to be optimized. One possible problem with this method is the breaking of the passivation layer. So, this layer needs to be thick enough to endure the SF_6 plasma cycle to achieve an anisotropic silicon etching. Another problem is related to the roughness of the sidewalls. A slow speed gas switching can result in rough sidewalls,

however, increasing the gas switching speed realizes smoother sidewalls. The Bosch DRIE process was invented in 1992 [3.18], and since then it has evolved and matured to a stable process, where these potential problems are very well controlled and mitigated.

3.2.2. Microfabricated devices

The microfabricated devices are in-plane capacitive movable structures, meaning that the direction of their movement is parallel to the die plane. The capacitive elements are composed of parallel-plate capacitors, formed by a group of comb-like features (electrodes) coupled to the movable proof-mass in conjunction with two fixed electrodes, one at each side of the movable one, thus enabling differential operation. The capacitance area is defined by the height of the beams (in this case is the thickness of the active layer), the overlapping length (117 µm), and the number of electrodes. Each device is composed of two sets of actuation electrodes in order to allow actuation on both directions (2×12), and two sets of sensing electrodes for differential sensing (2×20). Besides forming a capacitor, each set of two adjacent electrodes also creates a damper because of the small gap between them. This gap was designed to be 1.6 µm. In order to prevent contact between movable a fixed electrodes, one mechanical stopper was added in the center of the proof-mass, physically restricting its movement to 1.2 µm in each side (meaning that the gap between electrodes can vary from 0.4 µm to 2.8 µm), and thus protecting the device in case of pull-in or when the mass is subjected to high acceleration forces. To avoid large currents flowing through the device when the proof-mass contacts with the mechanical stopper, both elements have the same voltage potential.

The proof-mass is suspended by two flexible folded beams acting as springs. The beam design defines the dominant degree-of-freedom of the proof-mass, and in this case, was designed to be perpendicular to the plane of the parallel-plate capacitors. The layout of the springs is of paramount importance to maximize the displacement on the desired direction and minimize it to a negligible state on the other ones, transforming the movable structure in a 1-DOF device. To allow compliant enough springs, while respecting the minimum recommended feature size and maximum desired device size, a folded design was simulated and selected. Since the spring design contemplates rigid folding points (also known as elbows), its deflection is shared by the two beams, and the resultant elastic coefficient (k_s) is given by:

$$\frac{1}{k_s} = \frac{1}{k_{b1}} + \frac{1}{k_{b2}}, \tag{3.2}$$

where k_{b1} and k_{b2} represent the elastic coefficient of each beam and can be calculated using expression (2.4). Since the proof-mass is suspended by two equal mechanical springs, the total elastic coefficient is:

$$k = 2 \times k_s \tag{3.3}$$

Furthermore, the spring was designed taking into consideration the maximum proof-mass displacement of 1.2 µm, which is within the spring's natural range, thus ensuring that it is operating within the linear region (obeying Hooke's law).

It is essential to highlight that the microfabricated devices fully comply with the fabrication process rules, and no modifications are required to integrate them with commercially available Bosch inertial sensors.

Scanning electron microscope (SEM) images of the microfabricated MEMS devices are depicted in Figure 3.10, showing the complete design of the accelerometer and highlighting the mechanical stopper, capacitor electrodes, and mechanical spring with rigid elbows.

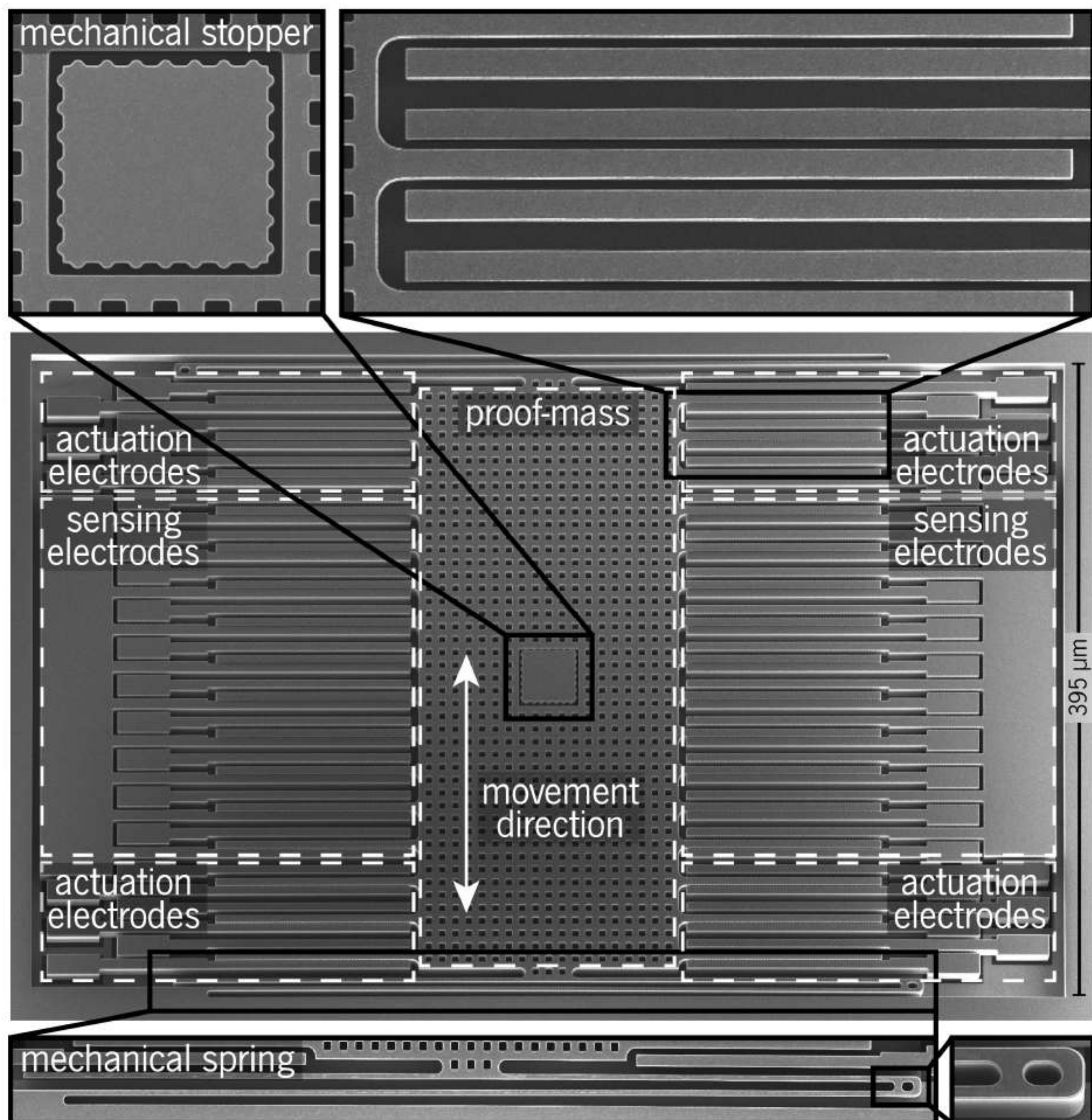

Figure 3.10. SEM images of the microfabricated MEMS accelerometer.

Table 3.1 presents a compilation of the main design parameters of the fabricated devices, obtained through analytical calculations and FEA simulations, for an encapsulation pressure of 140 Pa at 25 °C.

Table 3.1: Main design parameters of the fabricated device.

Design parameter	Value
Mass *(m)*	2.83 ug
Spring constant *(k)*	0.749 N/m
Natural resonance frequency (ω_0)	2591 Hz
Quality factor *(Q)*	58.6
Zero displacement gap (d_0)	1.60 μm
Damping coefficient *(b)* (gap = d_0)	0.818 μN.s/m
Sensing capacitance (C_{S0}) (gap = d_0)	246 fF
Actuation capacitance (C_{A0}) (gap = d_0)	148 fF
Pull-in voltage (V_{pi})	1.96 V
Thermal-mechanical noise	4.20 μg/√Hz
Active layer thickness	19 μm

After fabrication and wafer-level cap bonding, the sensor element was glued and wire-bonded to a 44-pin ceramic leadless chip carrier (CLCC-44), facilitating its electrical characterization (Figure 3.11).

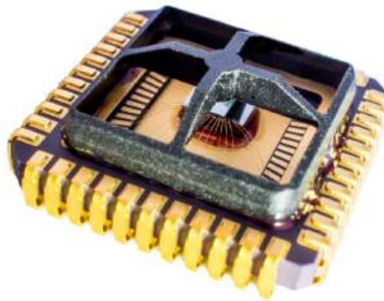

Figure 3.11: MEMS sensor in a CLCC-44 package.

3.3. Analog circuit

With the objective of interpreting the capacitance change of the MEMS sensor, a readout circuitry was designed. It is composed of a capacitance to voltage converter, a fully differential amplifier, and an analog-to-digital converter. Additionally, a one-bit DAC was implemented, enabling the electrostatic force feedback to the MEMS design. A simplified schematic is depicted in Figure 3.12, presenting the aforementioned components and the MEMS accelerometer. The sensor is illustrated by its electrical equivalent circuit: two actuation capacitances (top and bottom actuation capacitances: (C_{AT}) and (C_{AB}), respectively), two sensing capacitances (top and bottom sensing capacitances: (C_{ST}) and (C_{SB}), respectively), two parasitic capacitances (top and bottom parasitic capacitances: (C_{PT}) and (C_{PB}),

respectively), the common point between them, which in this case is the central mass *(CM)*, and the substrate *(SUB)*. The circuit was simulated and implemented in a printed circuit board (PCB) (Figure 3.13), and the complete schematics and layout are included in Annex A and Annex B, respectively. The remaining blocks are detailed in the following sections.

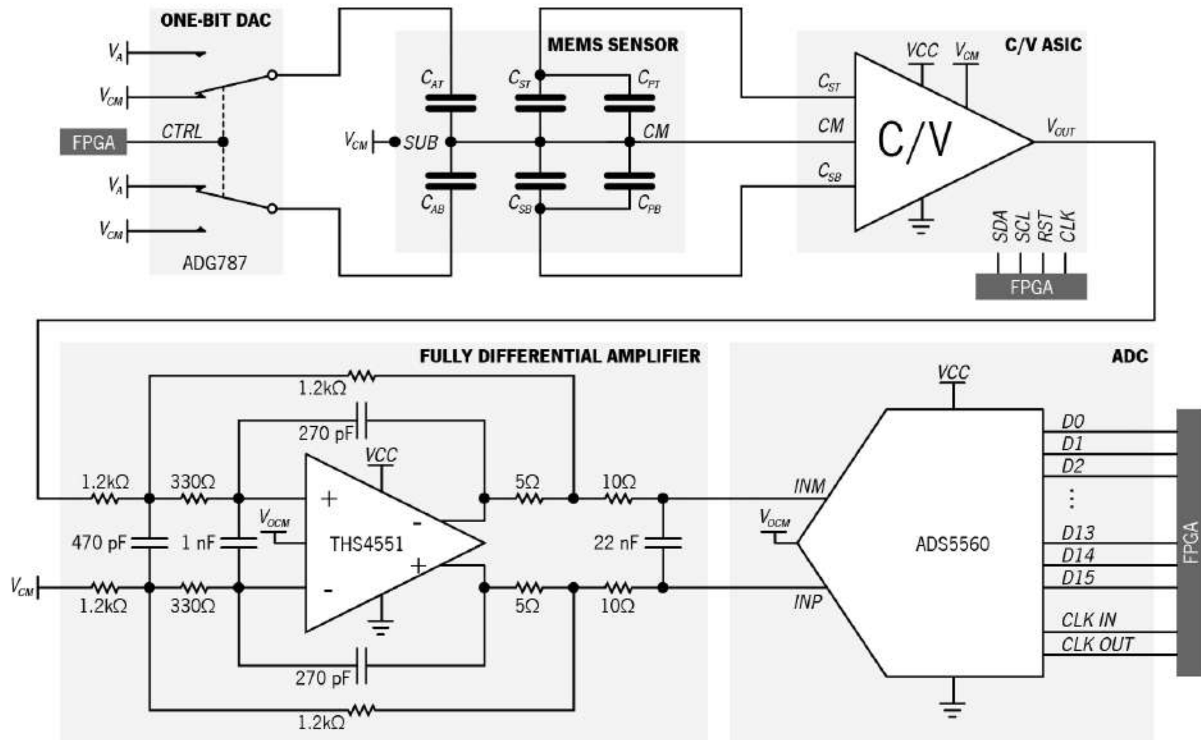

Figure 3.12: Simplified schematic of the analog circuit implementing the readout circuit and the one-bit DAC.

Figure 3.13: Implemented PCB, including the MEMS sensor, the C/V ASIC, the readout circuit, and the one-bit DAC.

3.3.1. Capacitive to voltage converter

The main goal of the C/V converter is to provide an output signal *(V_{OUT})* proportional to the capacitance variation of the MEMS element. To do this, it is necessary to understand the range of capacitances enabled by the sensor. At rest position, when the proof-mass is centered, both sensing capacitances (C_{ST}

and C_{SB}) have a value of 246 fF. As the proof-mass moves to the top side, C_{ST} increases, reaching 984 fF, while C_{SB} decreases to a minimum of 141 fF. If the proof-mass moves to the bottom side, the inverse behavior occurs, resulting in the differential capacitance *(C_{SD})* range of ±843 fF. This behavior is depicted in Figure 3.14.

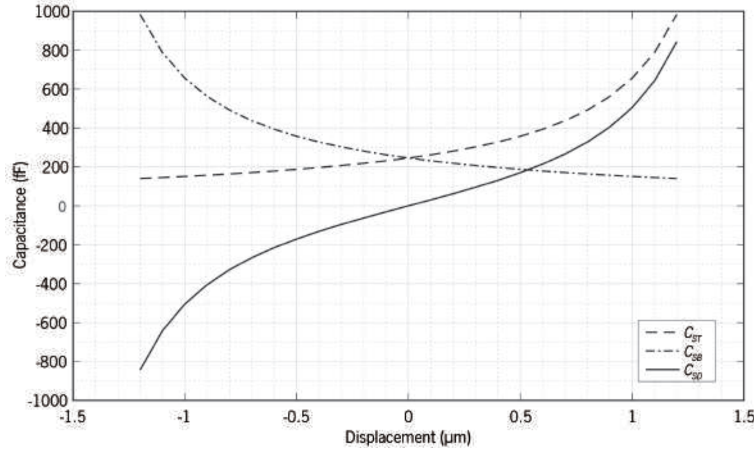

Figure 3.14: Sensing capacitance variation with proof-mass displacement.

The capacitance to voltage converter used was previously developed by F.S. Alves in [3.10]. It is a discrete-time differential switch capacitor circuit (Figure 3.15 a)) designed to operate using a single supply (+3.3 V) and a common-mode input voltage (V_{CM} = +1.65V). This ensures that the readout circuit and MEMS sensor are centered at the same voltage.

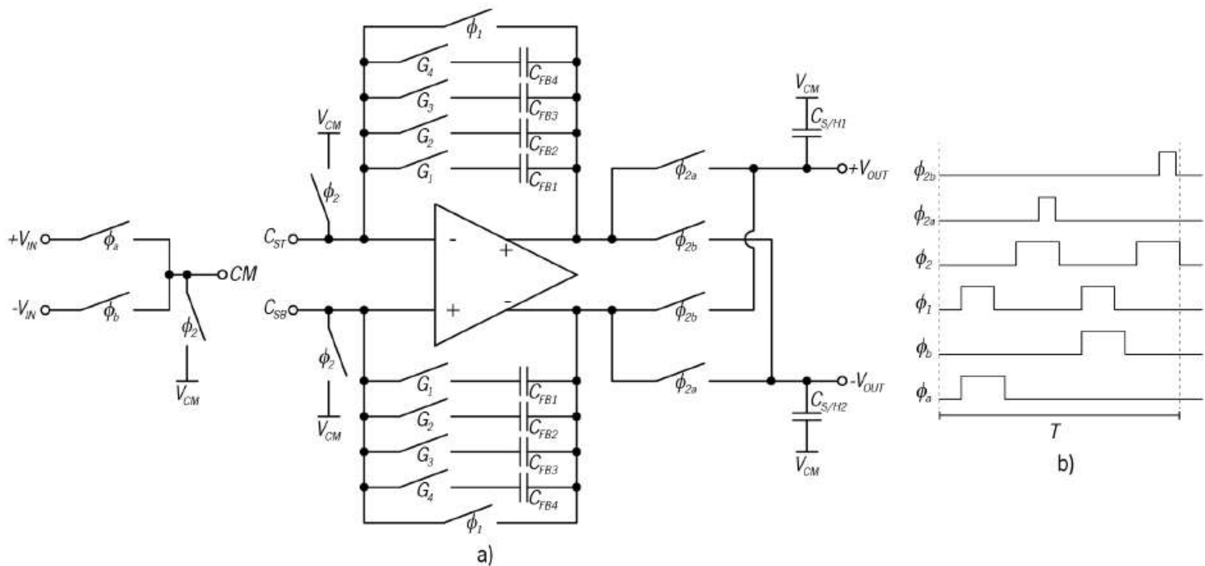

Figure 3.15: Fully differential switched capacitor capacitance to voltage converter [3.10]. a) Schematic; b) Control clock signals.

To provide flexibility, different converter gains can be selected through the feedback capacitors, and more than one capacitor can be selected at a time. The feedback capacitor values are represented in Table 3.2. Additionally, the amplitude of the input signals, $+V_{IN}$ and $-V_{IN}$, can also be selected from eight different

values, ranging from $V_{CM} \pm 110$ mV to $V_{CM} \pm 880$ mV, with a resolution of 110 mV. These parameters can be digitally selected using the I²C communication protocol of the C/V ASIC. It is important to notice that the capacitance to voltage converter differential output was shifted to a single-ended signal, realizing $V_{OUT} = +V_{OUT} - -V_{OUT}$.

Table 3.2: Capacitor values to define the capacitance to voltage converter gain.

Capacitor name	Value
C_{FB1}	250 fF
C_{FB2}	500 fF
C_{FB3}	1 pF
C_{FB4}	2 pF
$C_{S/H1}$	1 pF
$C_{S/H2}$	1 pF

The C/V ASIC was fabricated in the Austria Mikro Systeme (AMS) 0.35 µm complementary metal-oxide-semiconductor (CMOS) process [3.19], and it was later glued and wire bonded to a 24-pin ceramic dual-in-line package (DIP), as illustrated in Figure 3.16 b).

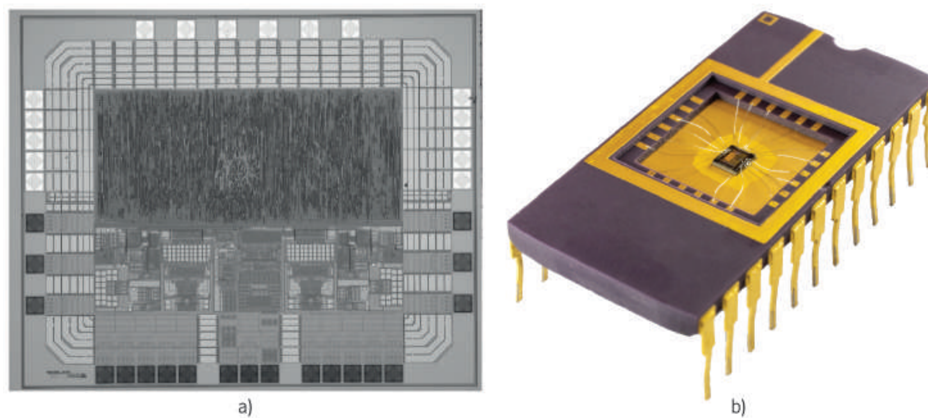

Figure 3.16: a) SEM picture of the fabricated ASIC. b) C/V ASIC in a DIP-24 chip carrier.

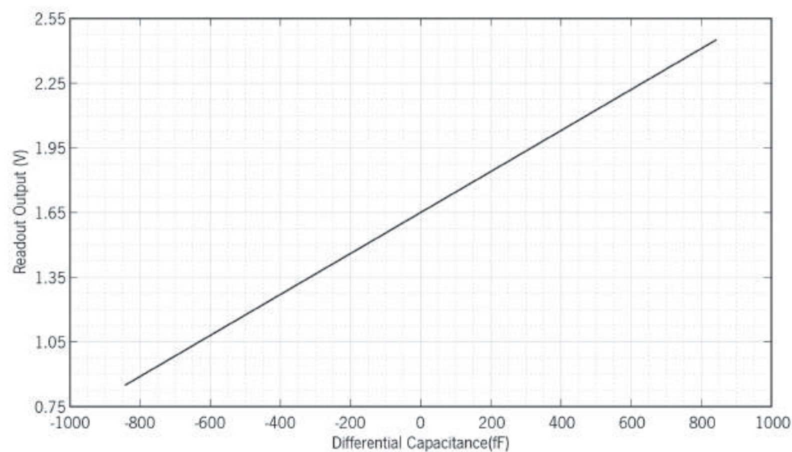

Figure 3.17: Capacitance to voltage converter output as a function of the sensed differential capacitance.

Due to the small capacitance change of the sensor, the feedback capacitor selected was C_{FB1}, resulting in a feedback capacitance of 250 fF, and V_{IN} was chosen to be $V_{CM} \pm 880$ mV, maximizing the output value range, without reaching signal saturation. Figure 3.17 depicts the resultant output voltage of the capacitance to voltage converter as a function of the sensed differential capacitance.

3.3.2. Signal acquisition

In this work, a mixed analog/digital approach using an electromechanical sigma-delta modulator with most components implemented in digital hardware is presented, meaning that all the required filtering blocks and noise shaping were digitally implemented in the FPGA. To enable this, the voltage signal proportional to the proof-mass displacement must be acquired into the digital domain. The selected approach was to use the Texas Instruments ADS5560, a high-performance 16-bit parallel ADC with sampling rates up to 40 MHz [3.20]. The ADC is based on switch capacitor technology and can be powered by a single 3.3 V supply. Additionally, it has a very high SNR for the MEMS signal baseband and includes a low-frequency noise suppression mode that improves the noise from DC to about 1 MHz. On the other hand, when the signal is captured by the ADC's sample and hold, it is sequentially converted by a series of small resolution stages, and at every clock edge the sample propagates through the pipeline, resulting in a data latency of 16 clock cycles. Its functional block diagram is depicted in Figure 3.18.

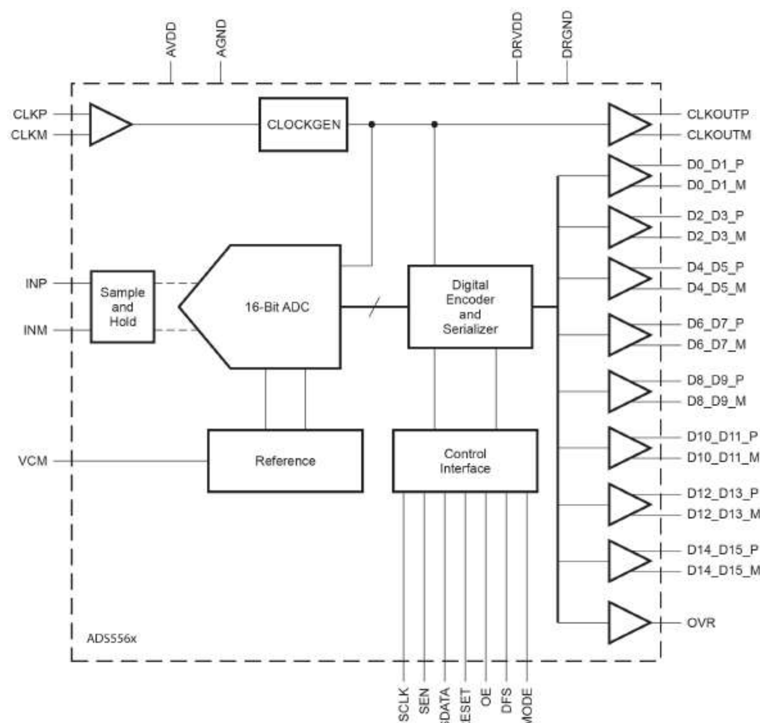

Figure 3.18: ADS5560 functional block diagram [3.20].

For optimum performance, the analog inputs must be driven differentially, improving the common-mode noise immunity and even-order harmonic rejection. To do so, the Texas Instruments THS4551 fully differential amplifier was used, which was designed for exceptional DC accuracy and low noise. It is well suited for driving high precision data acquisition systems with high SNR, such as the chosen ADC [3.21]. The amplifier was employed in a 500 kHz active multiple feedback filter, designed for F_o = 500 kHz and Q = 0.63, giving a linear phase response with the -3 dB frequency at 443 kHz (schematic in Figure 3.12). The 5 Ω resistors at the output pins and the 1 nF differential capacitor across the amplifier's input pins are not part of the filter design, and their function is to improve the loop-phase margin with minimal interaction with the active filter operation.

3.3.3. Electrostatic force voltage

An electromechanical sigma-delta modulator relies on an electrostatic force to provide the needed feedback to the MEMS sensor. Thus, actuation electrodes were added to the device, which need to be stimulated through an electrical voltage, realizing an electrostatic force given by (2.18). Since the MEMS element is referenced to V_{CM}, in order to achieve the desired electrostatic force, the actuation voltage must be calculated using (3.4), where V_{EF} is the effective electrostatic force voltage.

$$V_A = V_{EF} + V_{CM} \tag{3.4}$$

The voltage stimulus was provided by the LT6654, a precision voltage reference from Linear Technology (Analog Devices), which offers high accuracy (±0.05 %), low noise (1.6 ppm_{P-P}), and low temperature drift (10 ppm/°C Max) In this way, the noise due to the actuation voltage can be minimized. Thus, for a regulator output voltage of 5V, the effective actuation voltage is 3.35 V (5 V - 1.65 V), which according to (2.34), can counteract the acceleration force of approximately 18.7 g, fulfilling the desired requirements for measurement range and compatibility with ASIC voltages.

To enable actuation on both capacitors with the same voltage, the Analog Devices' ADG787 switches were used in the configuration shown in Figure 3.12. These have a low resistance of 2.5 Ω when in ON state and are suitable for up to 150 MHz switching [3.22]. They were connected in such a way that the electrostatic force is applied in one direction at a time, and the control signal is handled by the FPGA. The switches together with the voltage reference implement the one-bit DAC, needed for the electromechanical sigma-delta modulator with one-bit quantization.

3.4. FPFA programable logic

The desired operation of an electromechanical sigma-delta modulator greatly benefits from the programmable digital implementation of some blocks. To ensure high-frequency parallel execution between the different components, simple reconfiguration, and fast prototyping, these blocks were implemented in FPGA. The chosen platform was the Xilinx Zynq®-7000, and to facilitate the implementation, the ZedBoard development board (Figure 3.19) was selected. It features 85000 logic cells in the FPGA Programmable Logic, which are sufficient for this application, and a dual-core ARM Cortex™-A9 processor as the FPGA's Processing System that enables easy communication between the programmable hardware, the input/output peripherals fabric, and Gigabit Ethernet, to transfer data between the FPGA and a control and data logger station (in this case a computer running MATLAB) [3.23].

Figure 3.19: ZedBoard development board.

The typical blocks to implement digitally are the phase compensator, high-order loop filter, quantizer, and decimation filter. In this work, it were additionally implemented a digital low-pass filter, to further reduce the noise of the input signal, a digital interface to read the ADC data and remove the signal offset, the control signals needed for configuring the readout circuit and one-bit DAC, and a clock divider which provides different synchronous clock sources to the various blocks. The implemented programable hardware will communicate with the ARM processor present in the Zynq®-7000 chip through the advanced extensible interface (AXI) protocol, enabling on the fly configuration of all the loop parameters and gains. The resultant data will be handled by the processor and later sent to MATLAB, through TCP/IP, for further processing and evaluation. The block diagram of the implemented FPGA architecture can be seen in Figure 3.20, and the complete architecture implemented in Vivado Design Suite is presented in Annex C.

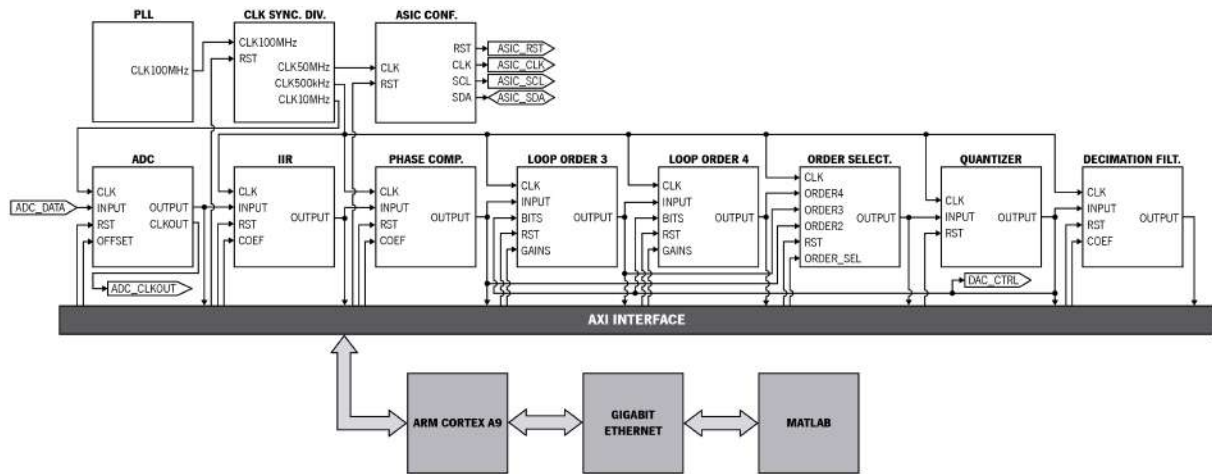

Figure 3.20: Block diagram of the implemented FPGA architecture.

3.4.1. Control and acquisition of the ADC data

A block responsible for reading the ADC data and providing the clock signal was implemented. The main operation consists of reading the 16-bit data from the ADC at every clock cycle and converting it to a 32-bit value, since all values will be stored in 32-bit registers. Additionally, an offset value (32-bit) is subtracted, which can be programmed by the ARM processor (FPGA PS). This feature enables offset correction of the acquired signal, which is of paramount importance for electromechanical sigma-delta modulators, since the offset can change between different MEMS devices. Due to the 16 clock cycles of latency, this block operates with a clock frequency of 10 MHz, twenty times larger than the 500 kHz frequency of the remaining digital blocks. In this way, the latency of the ADC can be neglected by the remaining blocks. In a later stage, the output of this module is converted to floating point using Xilinx® Floating-Point Operator core. From this point forward, all operations are performed using floating point arithmetic, thus reducing the quantization error when compared to integer arithmetic.

3.4.2. Low-pass filter

To reduce the noise of the input signal, a digital low-pass filter was implemented as part of the readout circuit. The chosen architecture was a discrete-time low-pass sixth-order infinite impulse response (IIR) filter using the direct form I, in order to optimize the arithmetic operations needed. The sixth-order is achieved by cascading three second-order sections, and the architecture of one second-order stage is shown in Figure 3.21, while the complete implementation in Vivado Design Suite is presented in Annex D. Each section implements the transfer function $H_{IIR}(z)$ accordingly to (3.5), which in the discrete-time domain translates to (3.6), where n symbolizes the current sample, $n\text{-}1$ the previous sample, and so on.

$$H_{IIR}(z) = g\,\frac{a_0.z^2 + a_1.z + a_2}{z^2 + b_1.z + b_2} \tag{3.5}$$

$$output_n = g \times \left(input_n.a_0 + input_{n-1}.a_1 + input_{n-2}.a_2 \right) - \left(output_{n-1}.b_1 + output_{n-2}.b_2 \right) \quad (3.6)$$

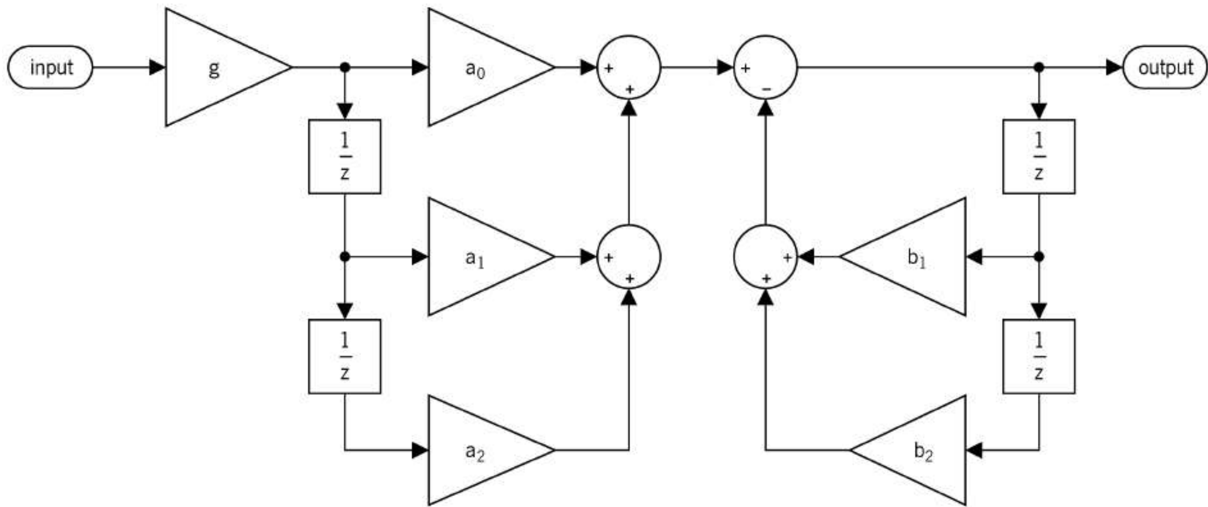

Figure 3.21: Second-order stage of the implemented discrete-time IIR filter.

The IIR filter was implemented so that the coefficients can be configured by the software application (PS), improving the flexibility of the system. Nonetheless, for this to work the cutoff frequency of the filter was set to 80 kHz, and the sampling frequency is 500 kHz. The resultant filter coefficients are presented in Table 3.3, and the filter's Bode plot is depicted in Figure 3.22.

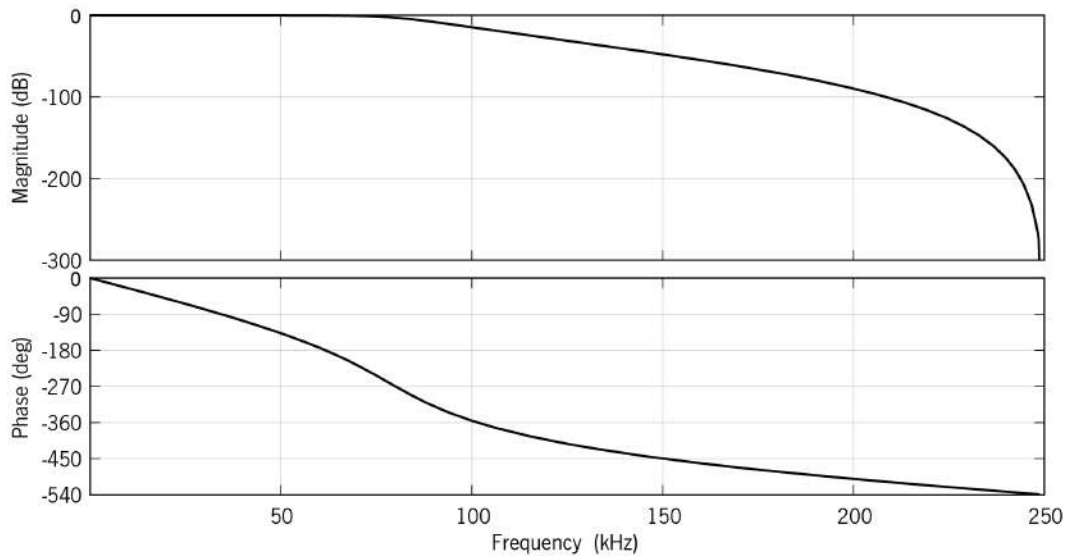

Figure 3.22: Bode plot of the implemented low-pass filter.

Table 3.3: Filter coefficients of the readout IIR filter for a cutoff frequency of 80 kHz.

Section	**g**	**a_0**	**a_1**	**a_2**	**b_1**	**b_2**
1	0.19046470366700072	1	2	1	-0.87946560136227936	0.64132441603028234
2	0.14532388387704243	1	2	1	-0.67102909077409623	0.25232462628226593
3	0.12783209539480656	1	2	1	-0.59026123205667735	0.10158961363590362

3.4.3. Phase compensator

As previously discussed, the MEMS element will introduce a phase delay in the readout signal. Additionally, the implemented low-pass filter will also add phase delay, as illustrated in Figure 3.22. To compensate the phase of the signal, ensure loop stability and improve the performance of the system, a phase compensator was implemented based on the approach proposed by Messner [3.24]. The compensator will apply the transfer function (2.30), which in the *z* domain is given by (3.7).

$$C(z) = \frac{a_0.z + a_1}{z + b_1} \tag{3.7}$$

Converting *C(z)* to the discrete-time domain, one gets (3.8).

$$output_n = input_n.a_0 + input_{n-1}.a_1 - output_{n-1}.b_1 \tag{3.8}$$

The phase compensator can be interpreted as a filter that introduces phase advance in the signal, and its block diagram is depicted in Figure 3.23, while the complete implementation in Vivado Design Suite is included in Annex E. Once again, the compensator was implemented in such way that its coefficients can be configured by the application running on the FPGA PS. Yet, for this work the phase compensator was configured to introduce 82 ° of phase advance at 42750 Hz (values obtained through experimental measurements), which translates to the coefficients shown in Table 3.4.The phase compensator's Bode plot is depicted in Figure 3.24.

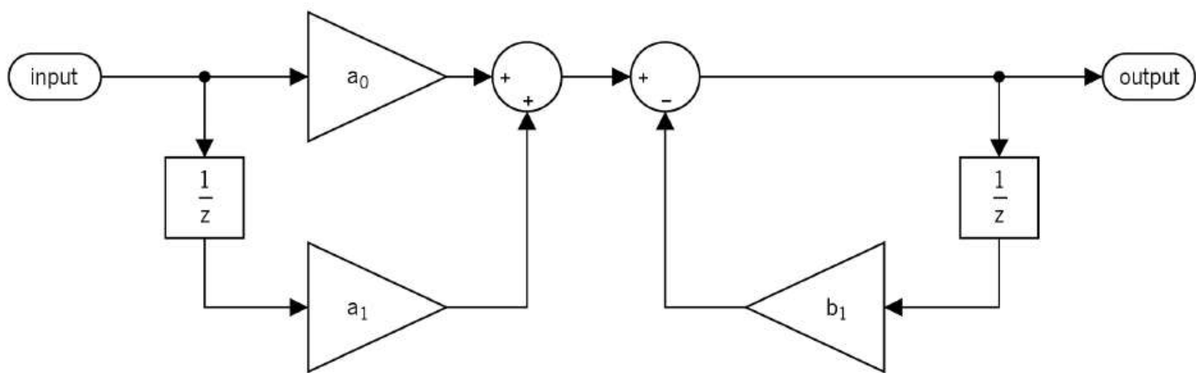

Figure 3.23: Implemented phase compensator.

Table 3.4: Phase compensator coefficients.

a_0	a_1	b_1
0.2104	-0.2027	0.5869

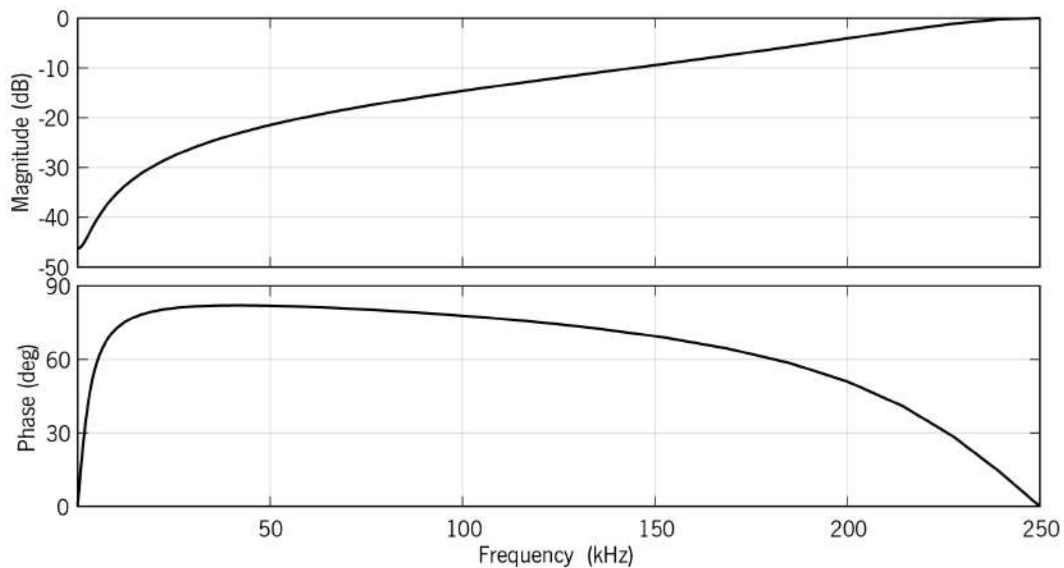

Figure 3.24: Bode plot of the implemented phase compensator.

3.4.4. Higher-order modulator loop

The proposed architecture of the electromechanical sigma-delta modulator, presented in Figure 3.1, allows for the selection of three different modulation orders (second-order, third-order, and fourth-order), improving the desired system flexibility. Since the second-order modulation quantizes the output signal of the phase compensator, two additional loops were implemented (one for third-order and one for fourth-order). These have two gains blocks, one in the feedback path and one in the forward path, and one discrete-time integrator, which provides the desired noise shaping. Moreover, an order selector was also implemented to support the selection of modulation order. This selector is a simple switch with three inputs and one output, controlled by a register that contains the order for the modulator. Once more, these blocks operate with a clock frequency of 500 kHz and were implemented using floating-point arithmetic to reduce the quantization error. The block diagram of the high-order loop is depicted in Figure 3.25, while the complete implementation of the third and fourth-order loops in the Vivado Design Suite is presented in Annex F.

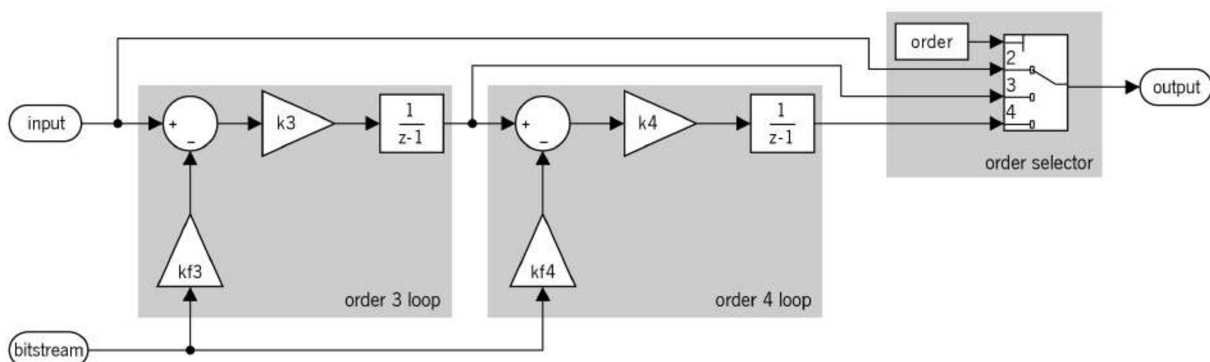

Figure 3.25: Block diagram of the high-order loop.

3.4.5. Quantizer

The block responsible for the one-bit quantization was implemented as a simple discrete-time comparator without hysteresis, working at 500 kHz clock signal. Basically, if the input value is higher than zero, the comparator outputs the value 1. Otherwise, it outputs the value -1. This is called bitstream and it plays a crucial role in the higher-order loop since it serves as input, changing the signal of the feedback gain. Additionally, the control signal for the actuation side of the one-bit DAC is also handled by the implemented quantizer.

3.4.6. Decimation filter

The decimation filter is composed by three sub-blocks: the multiplication of the bitstream by the desired resolution, the low-pass filter, and a decimator to reduce the bitstream frequency to the desired value. Regarding the first sub-block, the bitstream was multiplied by 2^{31}, converting the signal to 32-bits. After, the signal is filtered using a sixth-order IIR filter identical to the one presented in section 3.4.2. However, the desired cutoff frequency for this filter was set to 400 Hz, resulting in the 400 Hz bandwidth established by the requirements. Knowing that the sampling frequency is 500 kHz, the resultant filter coefficients are presented in Table 3.5, and filter's Bode plot is depicted in Figure 3.26.

Table 3.5: Filter coefficients of the decimation IIR filter for a cutoff frequency of 400 Hz.

Section	g	a_0	a_1	a_2	b_1	b_2
1	0.0000063083266305854044	1	2	1	-1.9973762254167329	0.99740145872325514
2	0.0000062941622305397051	1	2	1	-1.9928914170744696	0.9929165937233918
3	0.0000062860133362736024	1	2	1	-1.9903112704486381	0.99033641450198295

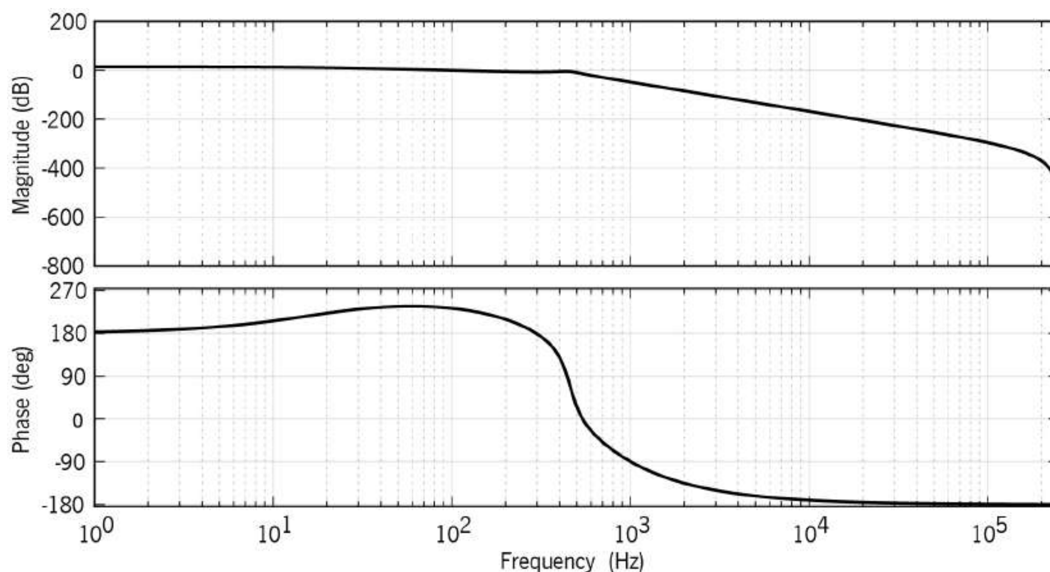

Figure 3.26: Bode plot of the implemented low-pass filter.

In the last sub-block, the signal must be decimated to the desired signal bandwidth. In this work, the output signal will have a 1000 Hz sampling frequency, which is more than two times larger than the signal bandwidth (400 Hz), complying with the Nyquist theorem. This results in a decimation factor of 500, which in other words means that the designed electromechanical sigma-delta modulator will have an oversampling ratio of 500. To achieve this, the decimation will be handled by the FPGA's ARM processor, and more details are presented in section 3.5.

3.5. FPGA processing system - software application

As previously mentioned, the chosen FPGA has an ARM processor, enabling communication between the designed hardware (PL) and the software application (PS). This allows for flexibility of the system, since some parameters can be configured by the FPGA PS, such as filter coefficients and loop gains, meaning that they can be configured at a software level without needing to synthesize the hardware. Additionally, this feature also enables an abstraction layer to the system, simplifying its use.

A real-time operating system (RTOS) was used to simplify application development, provide hardware abstraction for common peripherals and ensure that all timing requirements are fulfilled. Between the available open source operating systems, FreeRTOS was selected due to previous experience. FreeRTOS has a task scheduler that was used to guarantee that all tasks are executed on time. Moreover, FreeRTOS enables multitasking, greatly simplifying the software architecture design. A FreeRTOS porting to the Zynq®-7000 platform was already available [3.25].

To transfer data to a host PC, a TCP/IP protocol interface was implemented in the FPGA. A lightweight IP stack provided by Xilinx was selected (see application note available in [3.26]), which does not include all the TCP/IP stack but is well suited for this application, simplifying its use. In this context, the ARM processor will act as the server, while the client can be any device that connects to it to configure or acquire data (in this work a personal computer running MATLAB).

Using the multitasking features of the FreeRTOS, and streamlining the code architecture, two threads were developed. The first thread, named "main", is responsible for initializing the lightweight IP stack, create the communication server, and handle any network connection request. Additionally, the initialization and configuration of the system clocks and readout of the C/V converter ASIC are also held by this thread. When a new connection request is made, the thread "run" is created, which initializes the sigma-delta platform, configures the acquisition timer, interprets the received messages, and executes the commands attributed to each message.

There are three types of messages: *configuration*, which sets the higher-order loop gains, the modulation order, and the ADC offset; *stop*, that stops the acquisition timer and the electromechanical sigma-delta modulator operation (it opens both switches of the one-bit DAC); and *start*, which starts the operation of the electromechanical sigma-delta modulator (the switches of the one-bit DAC resume regular operation) and starts the acquisition timer.

The acquisition timer is configured to have a frequency of 1 kHz, and at every 1 ms acquires a sample from the decimation filter (using the FPGA internal AXI bus), thus effectively acquiring a sample at the desired signal decimation. The samples are packed and sent (TCP/IP) to the connected device. The flowcharts of both threads are presented in Figure 3.27.

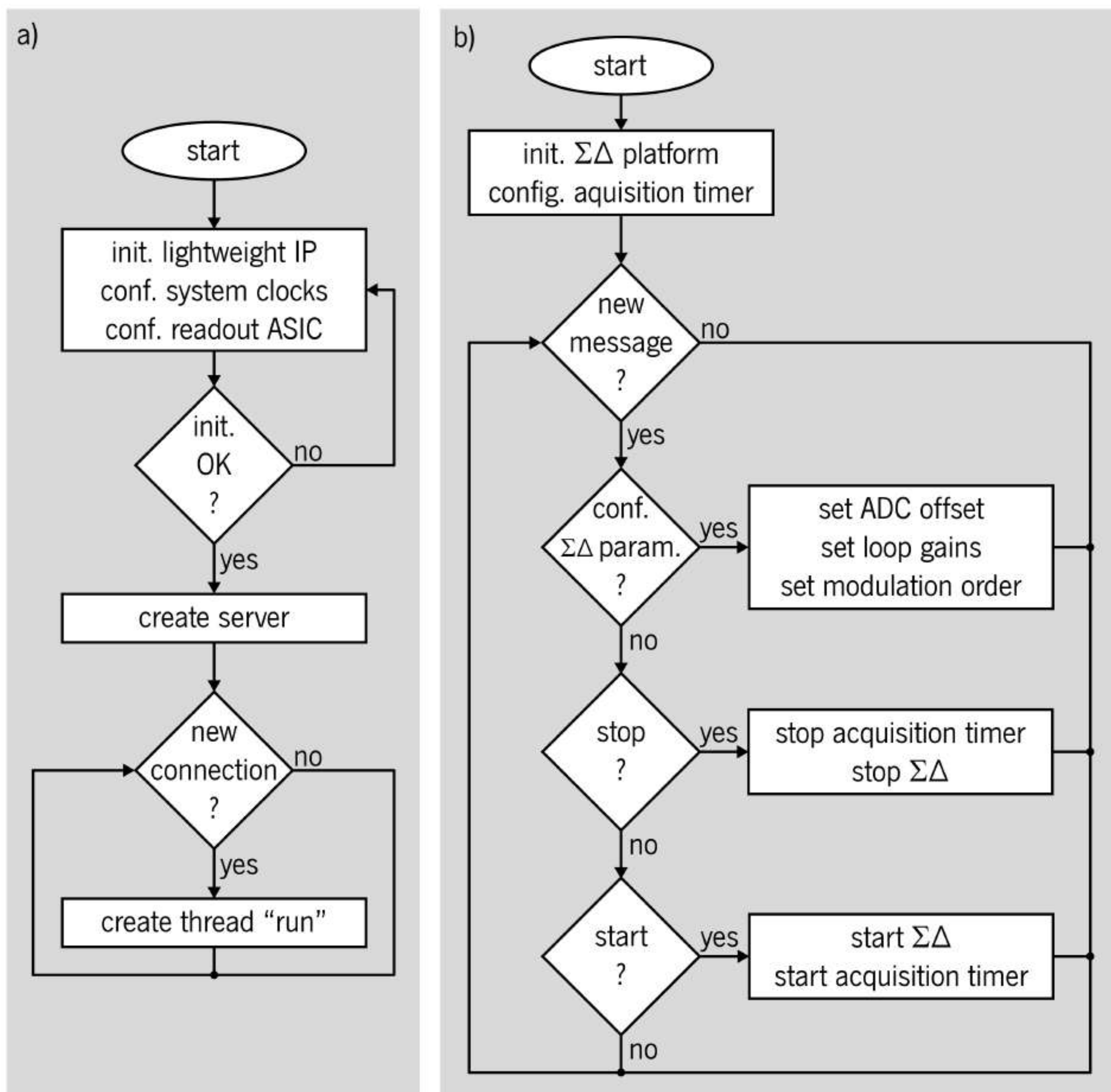

Figure 3.27: Software flowcharts. a) Thread "main"; b) Thread "run".

3.6. Conclusions

This chapter starts with the implemented simulation model, containing all the needed blocks. This served the purpose of validating the implemented FPGA hardware and software design and assess the performance of the electromechanical sigma-delta modulator. After, the implementation of the electromechanical sigma-delta modulator was described. First, the MEMS sensor design was explained, and its layout and characteristics were discussed. Details about the microfabrication process were also provided. After, the analog circuit, containing the readout and the 1-bit DAC, was described. The schematic of the capacitance to voltage converter, as well as the fully differential amplifier, used to implement the analog front end of the ADC, was presented and the 1-bit DAC architecture was described. A PCB that includes all these components was also presented. After, the digital blocks implemented in FPGA were explained, which are the low-pass filter, the phase compensator, the high-order loop, the 1-bit quantizer, and the decimation filter. Later, the software architecture running on the ARM processor was analyzed.

Although only the last system design and implementation are presented, since these are the ones that achieved better results, several architectures and implementations were simulated and some were also implemented. However, due to poor performance or system instability they were discarded.

References

[3.1] Y. H. Wang, L. Yin, D. L. Chen, L. Li, and X. W. Liu, "A method to reduce harmonic distortion of MEMS accelerometer," *Mod. Phys. Lett. B*, vol. 32, no. 21, 2018, doi: 10.1142/S0217984918502469.

[3.2] X. Li, J. Hu, and X. Liu, "A High-Performance Digital Interface Circuit for a High-Q Micro-Electromechanical System Accelerometer," *Micromachines*, vol. 9, no. 12, 2018, doi: 10.3390/mi9120675.

[3.3] H. Xu, X. Liu, and L. Yin, "A closed-loop ΣΔ interface for a high-Q micromechanical capacitive accelerometer with 200 ng/√Hz input noise density," *IEEE J. Solid-State Circuits*, vol. 50, no. 9, pp. 2101–2112, Sep. 2015, doi: 10.1109/JSSC.2015.2428278.

[3.4] F. Chen, W. Yuan, H. Chang, I. Zeimpekis, and M. Kraft, "Low noise vacuum MEMS closed-loop accelerometer using sixth-order multi-feedback loops and local resonator sigma delta modulator," in *IEEE 27th International Conference on Micro Electro Mechanical Systems (MEMS)*, 2014, pp. 761–764, doi: 10.1109/MEMSYS.2014.6765752.

[3.5] W. Henrion, L. DiSanza, M. Ip, S. Terry, and H. Jerman, "Wide dynamic range direct digital accelerometer," in *IEEE 4th Technical Digest. on Solid-State Sensor and Actuator Workshop*, 1990, pp. 153–157, doi: 10.1109/SOLSEN.1990.109842.

[3.6] P. Zwahlen, A.-M. Nguyen, Y. Dong, F. Rudolf, M. Pastre, and H. Schmid, “Navigation grade MEMS accelerometer,” in *IEEE 23rd International Conference on Micro Electro Mechanical Systems (MEMS)*, 2010, pp. 631–634, doi: 10.1109/MEMSYS.2010.5442327.

[3.7] P. Zwahlen *et al.*, “Breakthrough in high performance inertial navigation grade Sigma-Delta MEMS accelerometer,” in *IEEE/ION Position, Location and Navigation Symposium*, 2012, pp. 15–19, doi: 10.1109/PLANS.2012.6236858.

[3.8] Y. Dong, P. Zwahlen, A. M. Nguyen, R. Frosio, and F. Rudolf, “Ultra-high precision MEMS accelerometer,” in *16th International Solid-State Sensors, Actuators and Microsystems Conference*, 2011, pp. 695–698, doi: 10.1109/TRANSDUCERS.2011.5969218.

[3.9] R. Wilcock and M. Kraft, “Genetic Algorithm for the Design of Electro-Mechanical Sigma Delta Modulator MEMS Sensors,” *Sensors*, vol. 11, no. 12, pp. 9217–9232, Sep. 2011, doi: 10.3390/s111009217.

[3.10] F. S. Alves, “Auto-calibrated, thermal-compensated MEMS for smart inclinometers,” Universidade do Minho, 2017.

[3.11] R. A. Dias, L. Mol, R. F. Wolffenbuttel, E. Cretu, and L. A. Rocha, “Design of a Time-Based Micro-g Accelerometer,” *IEEE Sens. J.*, vol. 11, no. 8, pp. 1677–1683, Aug. 2011, doi: 10.1109/JSEN.2010.2103938.

[3.12] F. S. Alves, R. A. Dias, J. M. Cabral, J. Gaspar, and L. A. Rocha, “High-Resolution MEMS Inclinometer Based on Pull-In Voltage,” *J. Microelectromechanical Syst.*, vol. 24, no. 4, pp. 931–939, Aug. 2015, doi: 10.1109/JMEMS.2014.2359633.

[3.13] R. A. Dias, E. Cretu, R. Wolffenbuttel, and L. A. Rocha, “Pull-in-based μg-resolution accelerometer: Characterization and noise analysis,” *Sensors Actuators A Phys.*, vol. 172, no. 1, pp. 47–53, Dec. 2011, doi: 10.1016/j.sna.2011.01.027.

[3.14] C. S. Silva, R. A. Dias, J. C. Viana, A. J. Pontes, and L. A. Rocha, “Static and Dynamic Modeling of a 3-Axis Thermal Accelerometer,” *Procedia Eng.*, vol. 47, pp. 973–976, 2012, doi: 10.1016/j.proeng.2012.09.309.

[3.15] F. S. Alves, R. A. Dias, J. Cabral, L. A. Rocha, and J. Monteiro, “FPGA controlled MEMS inclinometer,” in *2013 IEEE International Symposium on Industrial Electronics*, 2013, pp. 1–4, doi: 10.1109/ISIE.2013.6563729.

[3.16] Robert Bosch GmbH, “Bosch MEMS sensor applications,” 2020. [Online]. Available: https://www.bosch.com/stories/bosch-mems-sensor-applications/. [Accessed: 19-Feb-2020].

[3.17] F. Laermer and A. Urban, “MEMS at Bosch – Si plasma etch success story, history, applications, and products,” *Plasma Process. Polym.*, vol. 16, no. 9, p. 1800207, Sep. 2019, doi: 10.1002/ppap.201800207.

[3.18] F. Laermer and A. Schilp, “Method of anisotropically etching silicon,” DE4241045C1, 1992.

[3.19] Austriamicrosystems, “0.35μm CMOS process (C35).” .

[3.20] Texas Instruments, "ADS556x 16-Bit, 40 and 80 MSPS ADCs With DDR LVDS and CMOS Outputs." ADS5560 datasheet, 2016.

[3.21] Texas Instruments, "THS4551 Low-Noise, Precision, 150-MHz, Fully Differential Amplifier." THS4551 datasheet, 2017.

[3.22] Analog Devices, "ADG 787 2.5 Ω CMOS Low Power Dual 2:1 Mux/Demux USB 1.1 Switch." ADG787 datasheet, 2006.

[3.23] AVNET, "ZedBoard Hardware User's Guide." 2014.

[3.24] W. Messner, "Formulas for asymmetric lead and lag compensators," in *2009 American Control Conference*, 2009, pp. 3769–3774, doi: 10.1109/ACC.2009.5160348.

[3.25] FreeRTOS, "Xilinx Zynq-7000 (dual core ARM Cortex-A9) SoC Port," 2016. [Online]. Available: https://www.freertos.org/RTOS-Xilinx-Zynq.html. [Accessed: 05-Mar-2020].

[3.26] A. Sarangi, S. MacMahon, and U. Cherukupaly, "LightWeight IP Application Examples." 2014.

4. Sensor characterization

In this chapter, the experimental characterization of the microfabricated devices is presented. Three similar devices were tested with the objective of assessing their performance, repeatability and susceptibility of the overall system to the tolerances of the fabrication process.

First, a mechanical characterization was performed, measuring the pull-in voltage, resonant frequency, and quality factor. This characterization highlighted a low variation between MEMS devices and a small variation to the theoretical and simulated design parameters.

The characterization of the accelerometer system was also performed. The experimental setups are explained, and several tests to evaluate the performance of the accelerometer were executed. The sensitivity and nonlinearity of all three devices were obtained, and the values were compared with simulated ones. Long term measurements were also performed, and the noise of the system was evaluated using Allan deviation measurements. The cross-axis sensitivity and temperature dependency of the sensor were also experimentally obtained. The frequency response of the system was characterized using a vibration exciter, and the bandwidth of the accelerometer was verified.

Aiming to improve the performance of the accelerometer and to validate the flexibility and configurability of the proposed architecture, the gains of the high-order sigma-delta modulator were optimized, reducing

the achieved noise level at the expense of a lower measurement range. This chapter concludes with a discussion about the obtained results.

4.1. Mechanical characterization of the MEMS accelerometer

The first characterization performed was related to the mechanical behavior of the MEMS itself. This way, in order to understand the dynamic behaviour of the mass-spring-damper system, the Bode plot of the three available sensors was plotted. Typically, the MEMS element is mechanically excited, and the displacement of the proof-mass is optically measured [4.1]. However, due to the accelerometer vacuum encapsulation, optical inspection is not possible. Thus, the sensor was electrically excited, and the response of the system was electrically measured using the implemented sensing electrodes. To electrically excite the MEMS element, a National Instruments data acquisition instrument (NI-DAQ USB-6363 BNC [4.2]) was used, also enabling de acquisition of the output signal of each device.

To obtain the resonant frequency and the quality factor of each sensor, a frequency sweep was performed, and the results are depicted in Figure 4.1. The magnitude and phase plots have the expected shape for a second-order mechanical system, and the measured values are presented in Table 4.1. Regarding the resonant frequency, the measured values have an error compared to the theoretical value inferior to 2.2 %, while the difference between devices is less than 0.1 %, suggesting very small fabrication process tolerances. The quality factor measurements have an error to the theoretical value inferior to 4.4 %, which is nearly the same between devices. While these are exceptional results (devices with an error below 5 %), the higher value can be explained by the difficulty in having the same cavity pressure on all devices.

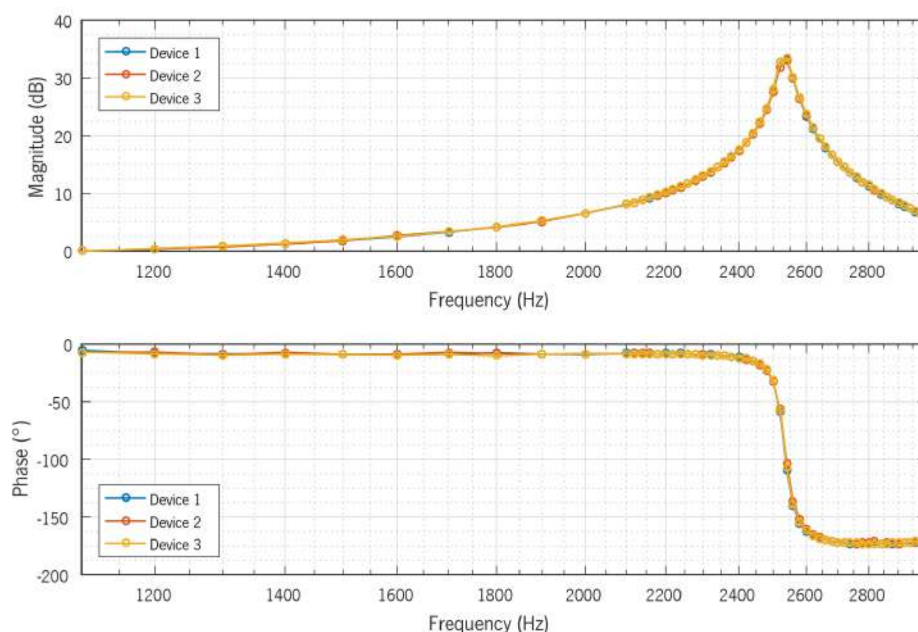

Figure 4.1: Bode plot of the three tested devices.

Table 4.1: Theoretical and experimental values of the resonant frequency and quality factor.

	Resonant frequency		**Quality factor**	
	Value	**Error**	**Value**	**Error**
Theoretical value	2591 Hz	-	58.6	-
Device 1	2535 Hz	2.2 %	58.3	0.5 %
Device 2	2537 Hz	2.1 %	56.0	4.4 %
Device 3	2536 Hz	2.1 %	58.6	0.0 %

Using the same setup, the pull-in voltage of the devices was also measured. To do this, the devices were actuated on both directions with an increasing voltage until the pull-in event was detected, measuring the pull-in voltage on both sides, as illustrated in Figure 4.2. After, the theoretical nominal pull-in voltage *(V_{pi})* was calculated using (4.1), where V_{pitop} is the pull-in voltage for the top side, and $V_{pibottom}$ is the pull-in voltage for the bottom side. The results are present in Table 4.2 and show an error deviation to the theoretical value and between devices inferior to 3.8 % and 0.3 %, respectively. Once again, these results suggest very small fabrication process tolerances.

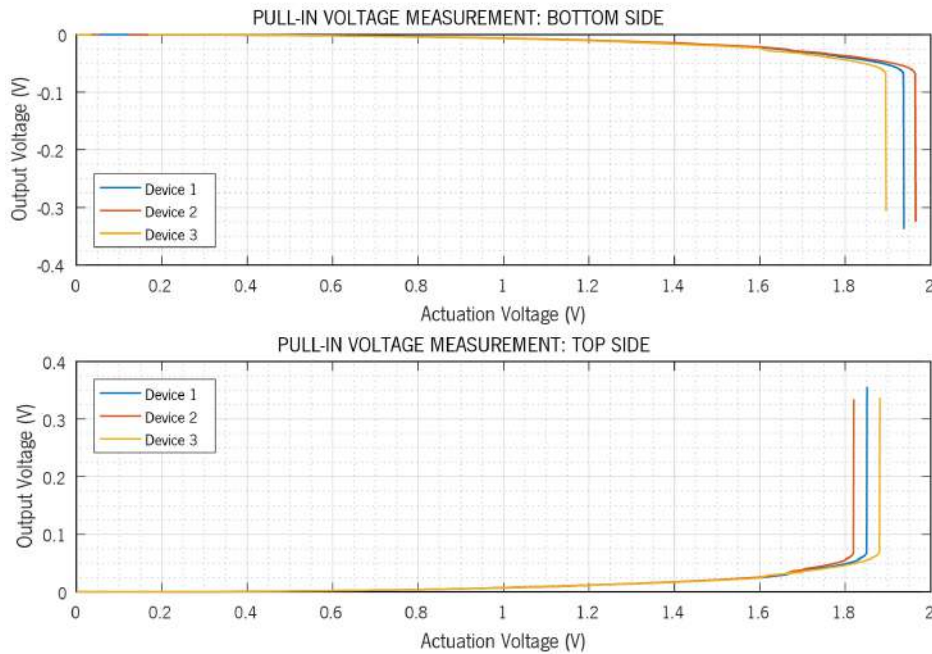

Figure 4.2: Pull-in voltage measurement.

$$V_{pi} = \frac{V_{pi_{top}} - V_{pi_{bottom}}}{2} \tag{4.1}$$

Table 4.2: Theoretical and experimentally measured nominal pull-in voltage.

	Pull-in voltage	
	Value	**Error**
Theoretical value	1.962 V	-
Device 1	1.893 V	3.5 %
Device 2	1.892 V	3.6 %
Device 3	1.888 V	3.8 %

4.2. Overall accelerometer system characterization

In this section, the characterization of the overall accelerometer system is presented. By accelerometer, it is meant the entire system, including the MEMS sensor, the analog readout (C/V ASIC) and one-bit DAC circuits, and the FPGA implemented digital blocks of the sigma-delta modulator accelerometer system.

The same three samples evaluated in the previous section were measured, and a battery of tests was performed, aiming to quantify the performance of the accelerometer. The obtained experimental data was then compared with the simulated values.

4.2.1. Experimental setups

In order to enable the measurement of the overall system performance, two experimental characterization setups were developed. The first setup, presented in Figure 4.3, was used to measure the sensitivity and nonlinearity of the proposed accelerometer. The manufactured PCB, containing the accelerometer sensor system, was mechanically coupled to a rotational precision motor, thus allowing to change the accelerometer angle relatively to the gravitational force. Therefore, by rotating the motor between +90 ° and -90 °, it is possible to achieve an excitation acceleration from +1 g to -1 g. The motor used was the PRMTZ8/M motorized rotation stage, controlled by a KDC101 K-Cube™ DC servo motor controller, both from Thorlabs, which have a rotation resolution of 0.0005 degrees [4.3].

The second experimental setup, depicted in Figure 4.4, was used to obtain the dynamic characterization of the sensor, extracting its frequency response, and consequently, its bandwidth. In this setup, the PCB was mechanically coupled to a vibration exciter from Brüel & Kjær (LDS V406), which is capable of achieving peak accelerations of 100 g and has a frequency range from 5 Hz to 9 kHz [4.4]. However, since the vibration exciter was coupled to a LDS Comet USB vibration controller, the maximum frequency was limited to 2400 Hz [4.5]. The signal input for the vibration controller was provided by a constant

charge line drive (CCLD) accelerometer from Brüel & Kjær (the Type 4534-B-001), which has a frequency range from 0.2 Hz to 12800 Hz and a noise level of 500 µg [4.6].

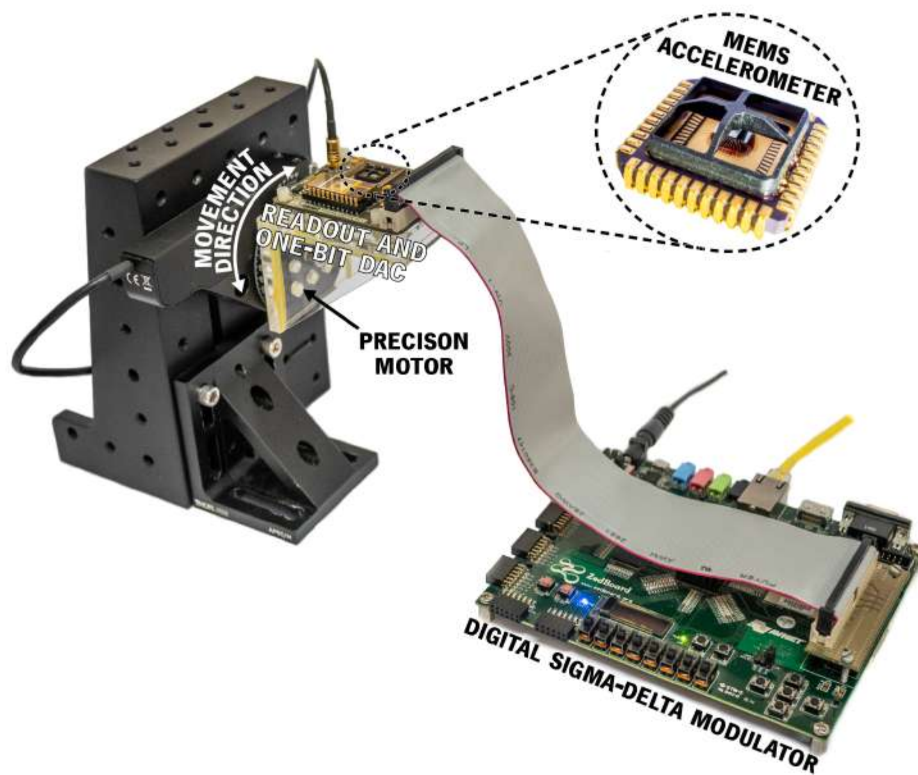

Figure 4.3: Experimental setup used to measure the sensitivity and nonlinearity of the accelerometer.

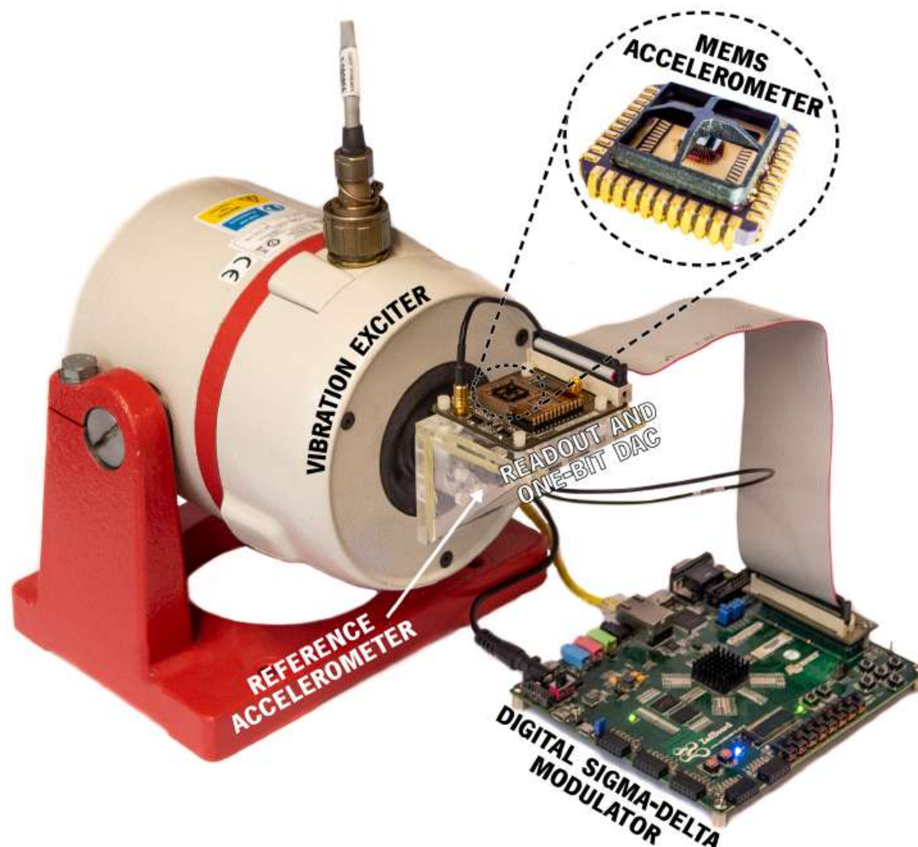

Figure 4.4: Experimental setup used to measure the frequency response of the accelerometer.

4.2.2. High-order loop gains

The implemented electromechanical sigma-delta modulator allows for a dynamic configuration of the loop parameters to achieve loop stability and improve the performance of the overall system. Typically, this process is performed through simulations [4.7], but the flexibility of this thesis' system allows an experimental fine-tuning at the final trim of the devices. Thus, using the setup presented in Figure 4.3, a sweep of the parameters was performed, measuring the sensitivity and standard deviation for each parameter set, aiming to experimentally reduce the overall sensor achievable noise.

First, the phase compensator was fine-tuned, in order to reduce the phase delay introduced by the MEMS element and the analog readout circuitry. The obtained results, depicted in Figure 4.5, lead to the introduction of a positive 82 degree shift of phase at 42750 Hz.

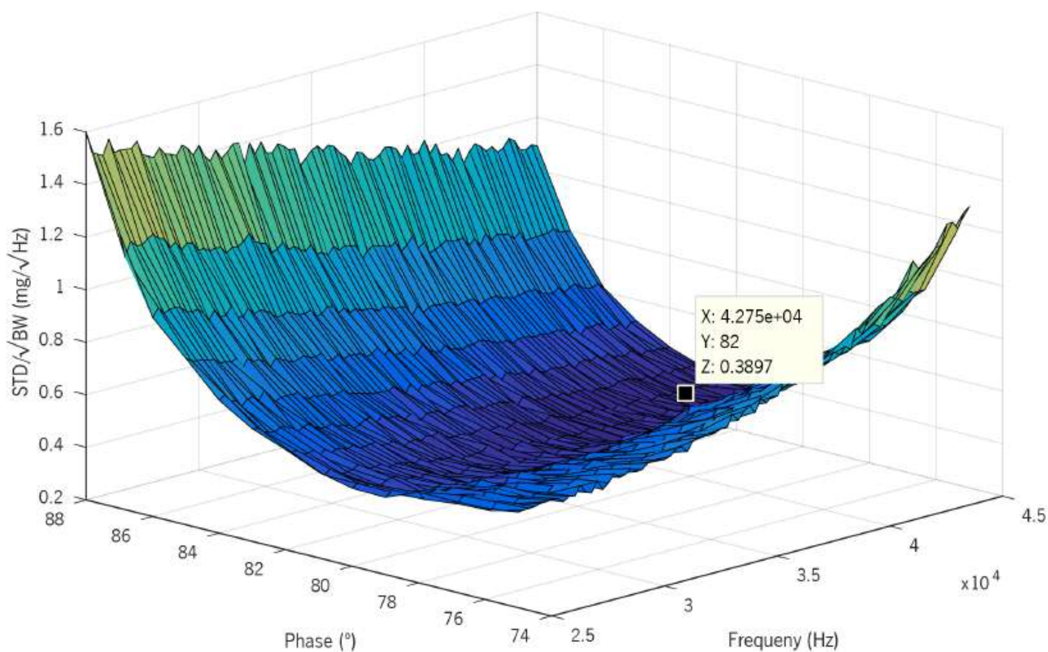

Figure 4.5: Optimization of phase compensator parameters.

The higher-order loop gains were also adjusted using the same gain sweep method. For the second-order typology, all the gains can be considered irrelevant since the MEMS accelerometer behaves as the second-order integrator. However, for higher orders, these must be tuned or the system may have degraded performance, or even become unstable. Thus, these gains were experimentally adjusted to k_{f3} = 12, k_3 = 0.1, k_{f4} = 7, and k_4 = 0.1.

4.2.3. Sensitivity and nonlinearity

The accelerometer was operated in open-loop and closed-loop topologies using the electromechanical sigma-delta modulator previously presented, and its sensitivity was experimentally measured using the setup illustrated in Figure 4.3 (previously simulated by using the developed simulation model presented in Chapter 3). The results, presented in Figure 4.6, show that the sensitivity increased drastically from open-loop to closed-loop, by a factor of over 900000, being 6.74 bits/g in open-loop and 26.76 bits/g using second-order modulation. Additionally, the sensitivity variation between devices is minimal. These results are corroborated by the simulation model, which was able to successfully predict the system behavior, with an error smaller than 7.4 %, in relation to experimental results.

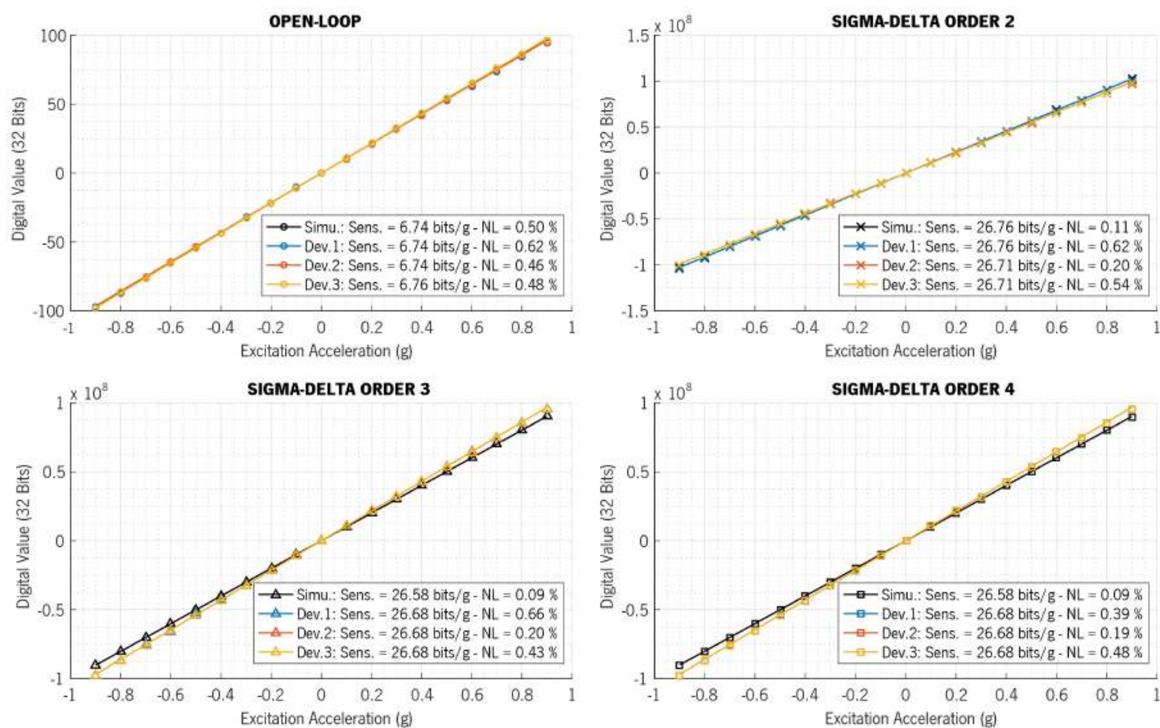

Figure 4.6: Experimental and simulated sensitivity and nonlinearity results.

Regarding the experimentally measured nonlinearity, the worst result obtained was a 0.66 % deviation from the linear fit, which is well below the desired maximum of 1 %. However, the simulated values indicate that this result should have been better, accomplishing a nonlinearity of approximately 0.1 % for the closed-loop operation. This difference is related to misalignments on the experimental setup, since the MEMS element is glued to the chip-carrier with an error of 1%, the chip-carrier socket is hand soldered to the PCB, and the PCB was coupled to the rotation motor using a manual process, leading to an increase of the perceived nonlinearity. In order to prove it, an attempt to manually align the setup was made for device number 2, which reduced the experimental nonlinearity from approximately 0.42 % to approximately 0.2 %.

4.2.4. Noise figure

The noise figure of the accelerometer was also evaluated. To do this, the output signal of the system was acquired during five hours, for each of the three devices and for each modulation order, and the Allan deviation was calculated for all cases. The obtained results are depicted in Figure 4.7.

The Allan variance, also known as two-sample variance, was originally developed by David W. Allan to measure the frequency stability of oscillators, clocks, and amplifiers. The Allan deviation, otherwise called sigma-tau, is the square root of the Allan variance and is now a commonly accepted method to benchmark the noise performance of MEMS inertial sensors [4.8], [4.9].

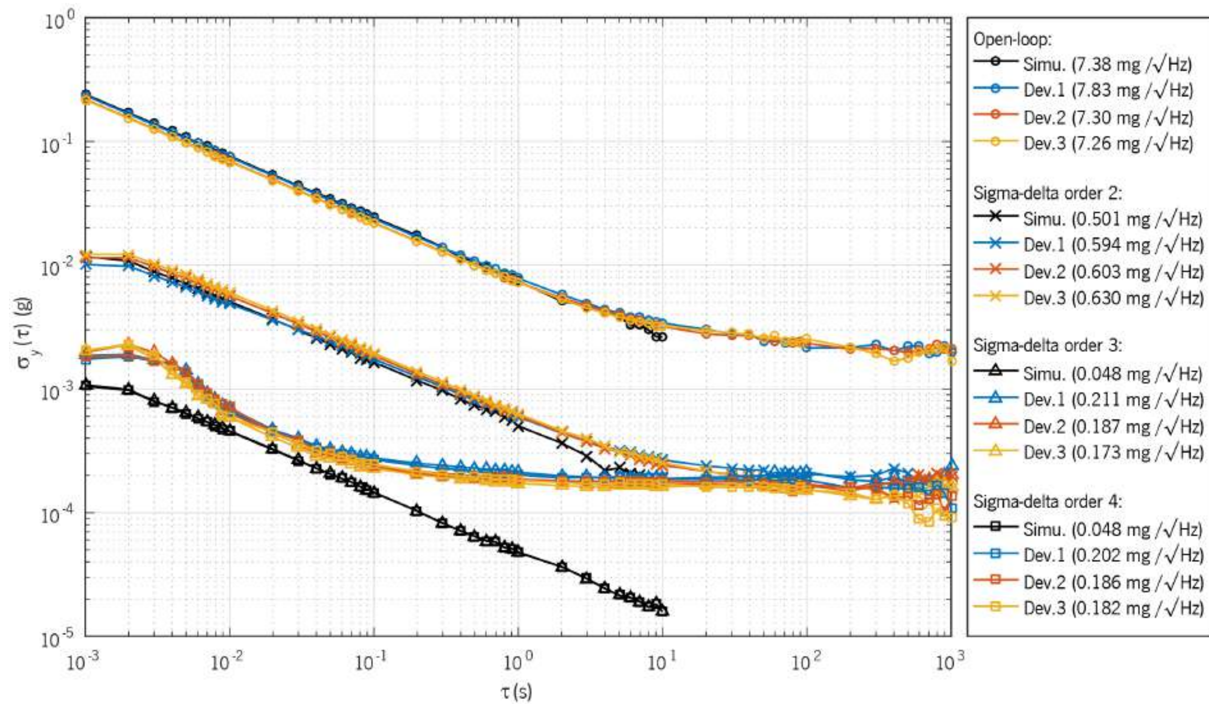

Figure 4.7: Experimental and simulated Allan deviation measurements.

As expected, the results show the better noise figures achieved by higher modulation orders. In open-loop operation, the best noise level achieved was 7.26 mg/√Hz. Nonetheless, using a second-order sigma-delta modulation, the noise figure decreases to approximately 600 μg/√Hz. Increasing the modulation order, to the third order configuration of the sigma-delta modulator, the noise figure decreases further, reaching 173 μg/√Hz for device number three. However, the fourth-order sigma-delta modulator resolves approximately the same noise level as third-order. This is attributed to the system reaching the limit of the low-frequency electrical noise. Additionally, the offset stability can also be deduced from the experimental measurements, and for open-loop is approximately 2 mg, while decreasing to 200 μg in closed-loop operation. Furthermore, these results were compared with simulation, and the developed

simulation model was able to reproduce the system behavior with some limitations, especially for low noise levels and at low frequencies. These limitations are due to the simplified readout analog circuit model implementation, which was executed as a simple capacitance to voltage gain with the addition of white noise only. From the results, one can infer that there is 1/f noise present on the system, introduced by the electronic circuitry that was not implemented on the simulation model.

To illustrate the difference between the signal obtained by operating the sensor in open-loop, in second-order, and in third-order modulator configuration (fourth-order is not illustrated because it yields similar results as third-order), a graphic with ten seconds of raw measurements for each configuration is presented in Figure 4.8. The figure demonstrates the difference, in terms of noise, between operation modes that could be difficult to perceive from the Allan deviation graphic.

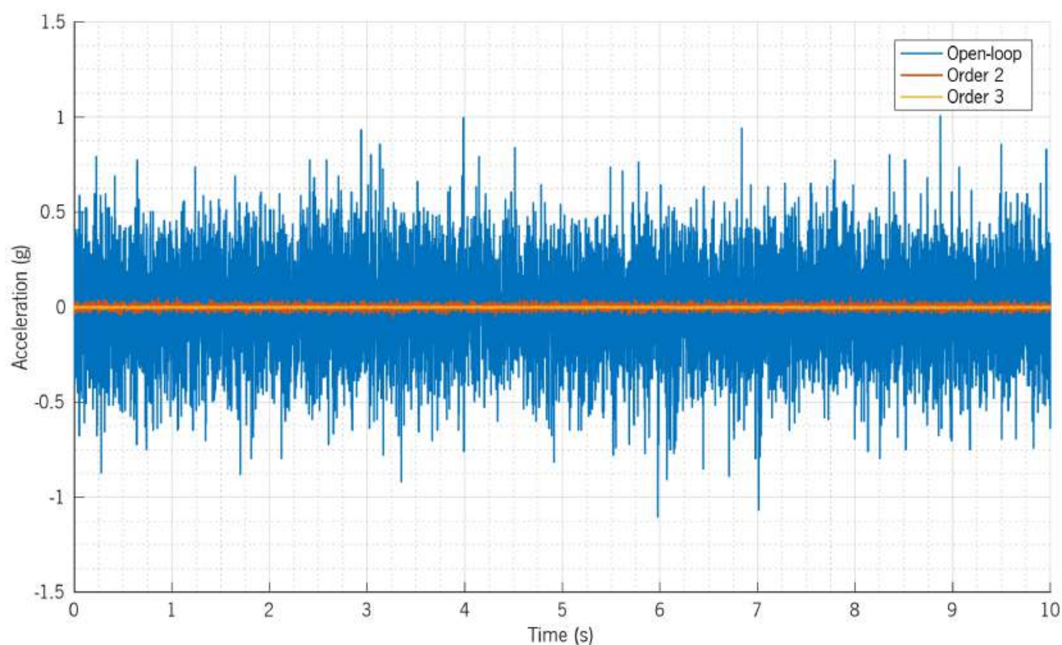

Figure 4.8: Comparison of the raw acceleration values between open-loop and closed-loop configurations.

4.2.5. Cross-axis sensitivity

The MEMS accelerometer was designed to be single axis, meaning that it would only be sensitive to accelerations in one direction. However, due to the mechanical properties of the MEMS spring, the proof-mass will also move when acceleration forces are applied in the other directions. To experimentally test this, the setup presented in Figure 4.3 was used, and the PCB was rotated 90 °, allowing for the accelerometer to be excited in the non-sensitive direction by the gravitational force. The obtained results are depicted in Figure 4.9.

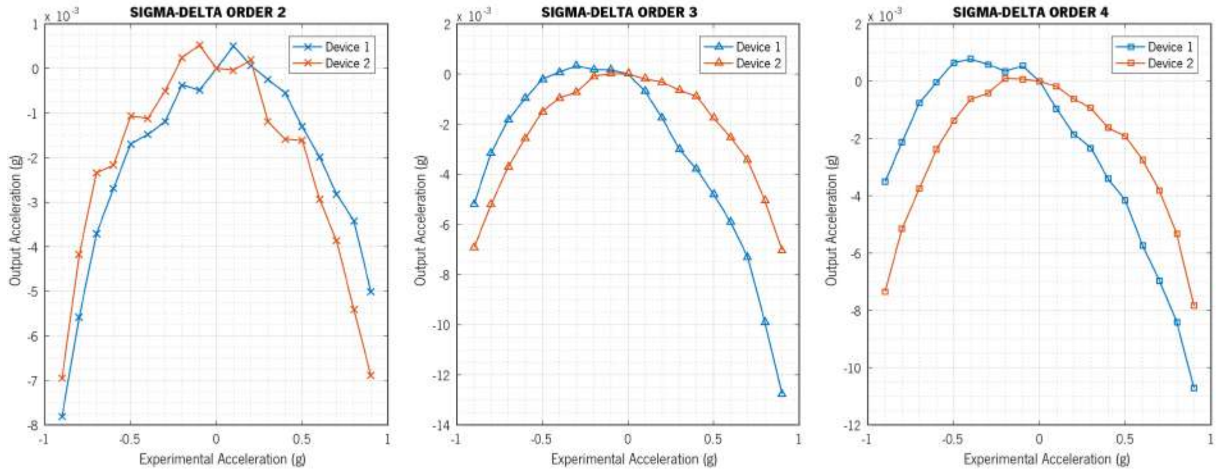

Figure 4.9: Experimental cross-axis sensitivity measurements.

Using equation (4.2), the cross-axis sensitivity of both devices was calculated for the three different modulation configurations. The results are presented in Table 4.3, where X-axis is the sensitive axis and Y-axis is the non-sensitive axis. A linear fit was applied to obtain the sensitivity on the Y-axis, and the accelerometer shows a cross-axis sensitivity inferior to approximately 0.4 %, for a measurement range of ± 0.9 g.

$$CrossAxisSensitivity(\%) = \frac{SensitivityYaxis}{SensitivityXaxis} \times 100 \tag{4.2}$$

Table 4.3: Cross-axis sensitivity calculations.

	Order 2		**Order 3**		**Order 4**	
	Device 1	**Device 2**	**Device 1**	**Device 2**	**Device 1**	**Device 2**
X-axis sensitivity	26.76 bits/g	26.76 bits/g	26.68 bits/g	26.68 bits/g	26.68 bits/g	26.68 bits/g
Y-axis sensitivity	16.95 bits/g	15.95 bits/g	18.69 bits/g	10.13 bits/g	18.72 bits/g	15.05 bits/g
Cross-axis sensitivity	0.111 %	-0.060 %	-0.392 %	0.001 %	-0.401 %	-0.031 %

4.2.6. Temperature dependency

As reported in section 2.3.2, capacitive MEMS elements exhibit a temperature dependency due to the silicon thermal expansion and the change in Young modulus with temperature. To experimentally test the temperature dependency of the developed accelerometer, the complete accelerometer system (MEMS element and analog circuit) was placed inside a temperature test chamber (ACS DY60 T), and temperature cycles were performed. Two behaviors were tested: the change in the signal offset, resulting in a temperature coefficient, and the sensitivity change with temperature.

In order to verify the temperature coefficient of the implemented accelerometer, the temperature of the chamber was increased to approximately 70 °C. Then, the test chamber was switched off, resulting in a slow decrease of temperature until it reached room temperature, which was approximately 27 °C. In this way, the vibrations due to the compressors required for temperature control were not present. In Figure 4.10, the experimental measurements performed for the three devices and all implemented modulation orders, for an acceleration of approximately 0 g, is depicted.

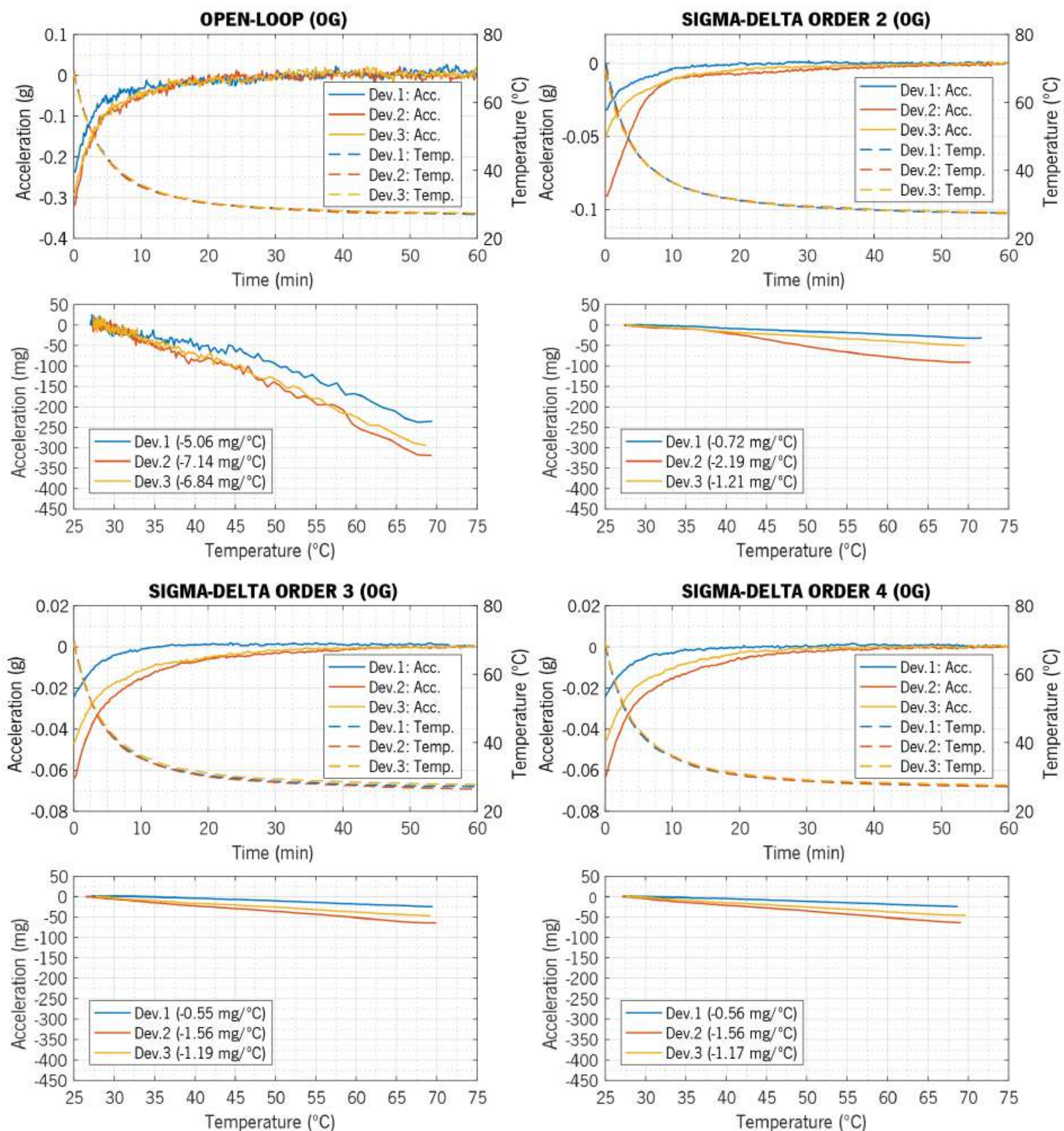

Figure 4.10: Temperature coefficient measurements for approximately 0 g acceleration.

The results show that the measured temperature dependency can be approximated to a linear temperature coefficient that can be easily calibrated. The temperature dependency dramatically reduces when switching from open-loop to closed-loop system operation. However, the measured temperature coefficient presents some variance between devices. The same measurements were performed, for an acceleration of approximately 1 g, to attest that the temperature coefficient is independent of the excitation acceleration. The obtained results, showed in Figure 4.11, present a similar tendency (except for second-order modulation), and the obtained temperature coefficients are similar to the ones of the 0 g test, mainly for the higher modulation orders.

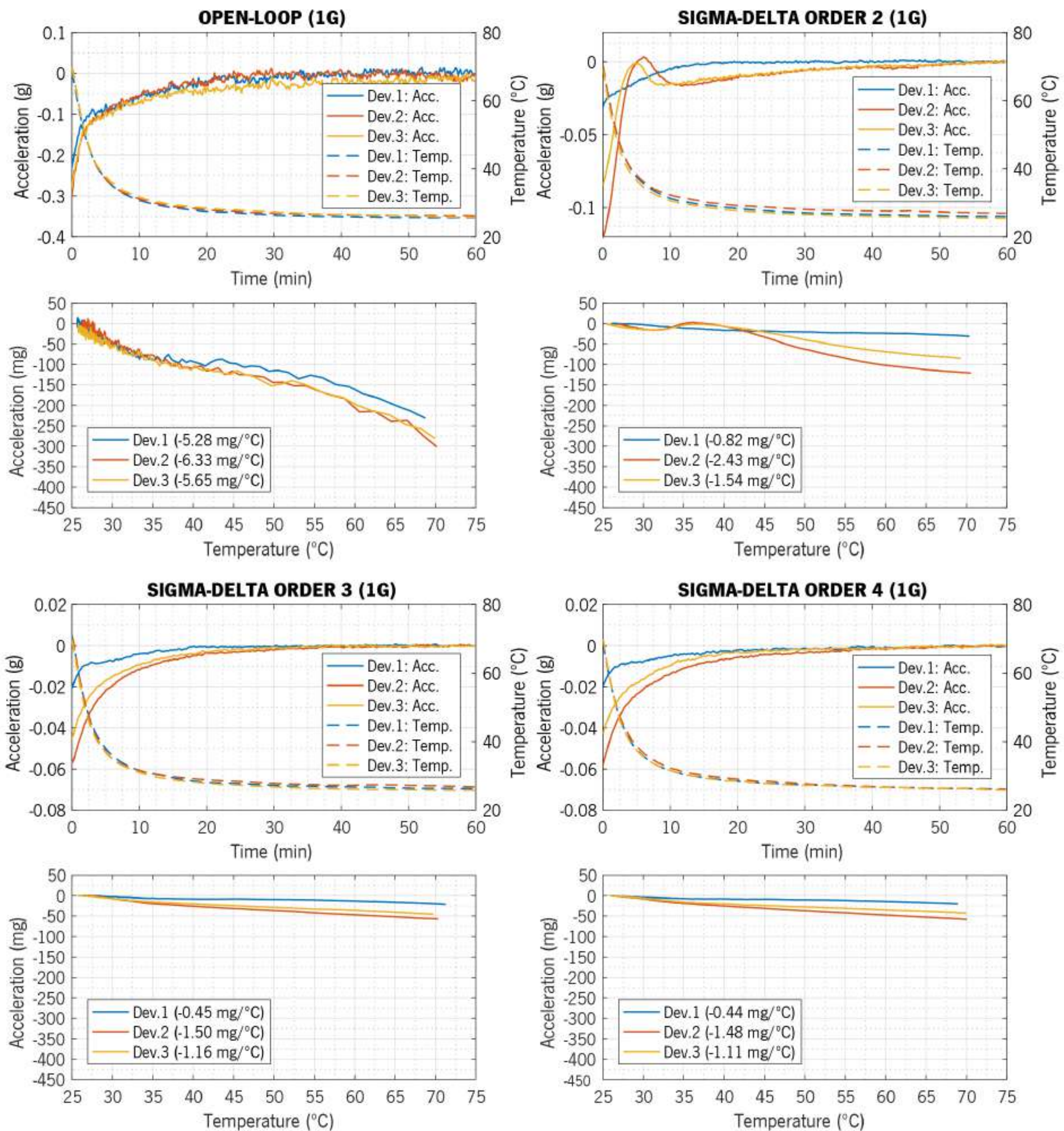

Figure 4.11: Temperature coefficient measurements for approximately 1 g acceleration.

To compensate for the temperature effects, the mean value of the temperature coefficients for each modulation order was calculated, resulting in a coefficient of -6.3 mg/°C for open-loop operation, -1.4 mg/°C for closed-loop second-order modulator, and -1.1 mg/°C for closed-loop third and fourth-order modulators. After, these values were used to compensate the obtained measurements, using the expression (4.3), were *acc* is the measured acceleration, α represents the temperature coefficient, and T symbolizes the temperature.

$$acc(T) = acc - (\alpha \times \Delta T) \tag{4.3}$$

Figure 4.12 depicts the comparison between the measurements with and without the compensation schema. Due to the sample variation, the proposed method is capable of significantly reducing the temperature effects on device 3, while at the same time invert the temperature coefficient for device 1. For a more effective compensation of the temperature effect, the measured temperature coefficient of each device can be used (since the behavior is linear, only two points need to be measured), leading to the elimination of the temperature effects. However, this means that calibration for each specific device must be performed, potentially leading to an increase in the production cost.

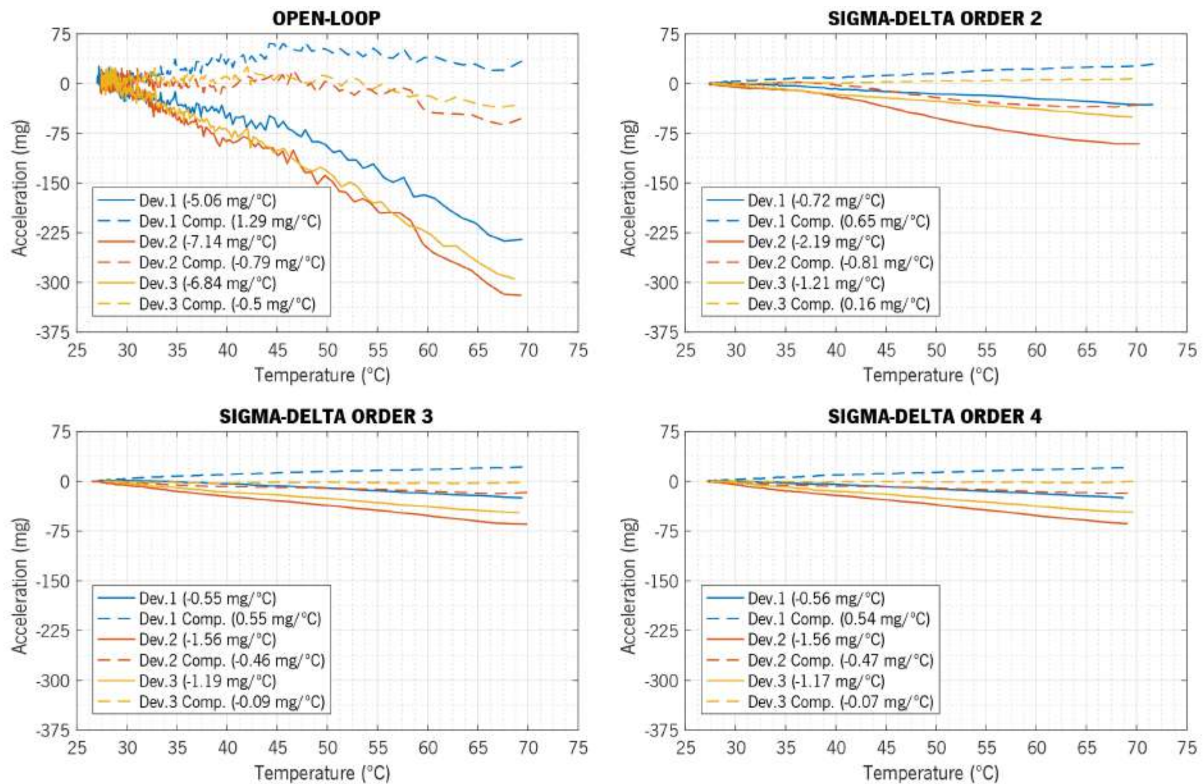

Figure 4.12: Compensation of the temperature effects.

The temperature dependency of the sensitivity of the accelerometer was also measured. To do this, the sensitivity was assessed for three different temperatures (approximately 13 °C, 27 °C, and 43 °C), and the results are presented in Table 4.4. From the obtained measurements, it is possible to conclude that the sensitivity does not change with temperature.

Table 4.4: Temperature dependency of the sensitivity of the accelerometer.

		13 °C	27 °C	43 °C
Open-loop	**Device 1**	6.76 bits/g	6.74 bits/g	6.75 bits/g
	Device 2	6.75 bits/g	6.75 bits/g	6.74 bits/g
	Device 3	6.76 bits/g	6.78 bits/g	6.82 bits/g
2nd order	**Device 1**	26.75 bits/g	26.77 bits/g	26.78 bits/g
	Device 2	26.72 bits/g	26.74 bits/g	26.72 bits/g
	Device 3	26.73 bits/g	26.75 bits/g	26.75 bits/g
3rd order	**Device 1**	26.68 bits/g	26.68 bits/g	26.68 bits/g
	Device 2	26.69 bits/g	26.68 bits/g	26.68 bits/g
	Device 3	26.68 bits/g	26.68 bits/g	26.68 bits/g
4th order	**Device 1**	26.68 bits/g	26.68 bits/g	26.68 bits/g
	Device 2	26.69 bits/g	26.68 bits/g	26.69 bits/g
	Device 3	26.68 bits/g	26.68 bits/g	26.68 bits/g

4.2.7. Frequency response

The frequency response of the accelerometer was measured using the setup presented in Figure 4.4. The experimental tests consisted on exciting the accelerometer system using a sinusoidal acceleration with ±5 g of amplitude for frequencies ranging from 100 Hz to 500 Hz. The experimental results of this test are depicted in Figure 4.13, and a comparison with the simulation values is performed.

From the results, it is possible to observe that the accelerometer system achieves the desired 400 Hz bandwidth for all configurations. Furthermore the ±5 g range target was also achieved. Moreover, the sensor presents a flat response on the signal interest band (until 400 Hz), meaning that the signal amplitude is not influenced by the excitation frequency.

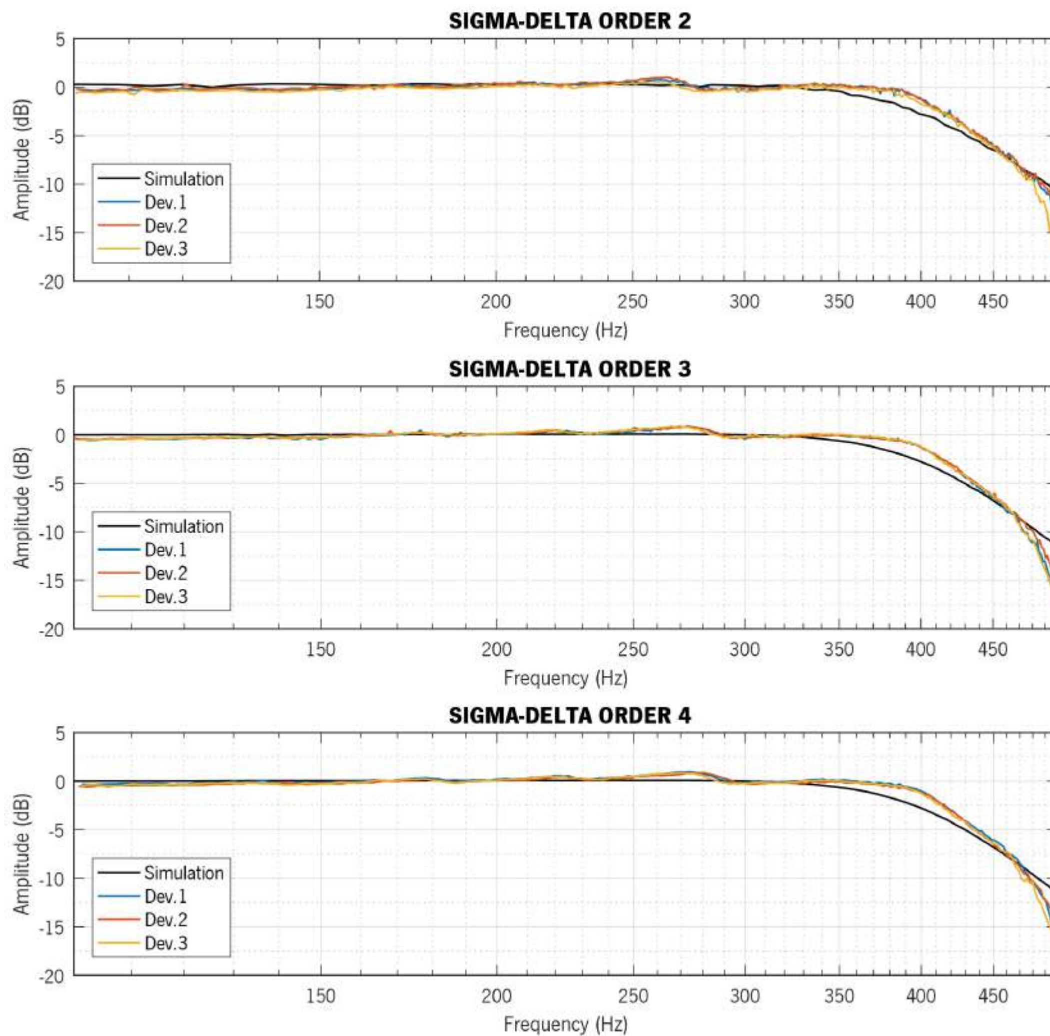

Figure 4.13: Frequency response of the accelerometer.

4.2.8. Vibration robustness

As previously stated, one of the target applications for this accelerometer system is in the automotive industry. For this market, the vibration robustness of the device is essential since the accelerometer will be subjected to external accelerations due to vehicle vibrations. The closed-loop control must be capable of handling these vibrations while maintaining the proper function of the device. Additionally, the third and fourth-order modulators introduce zeros and poles to the system transfer function, which potentially could lead to instability.

To ensure the stability of the system throughout the frequency range, the accelerometer system was excited using a sinusoidal acceleration with ±2 g of amplitude for frequencies ranging from 100 Hz to 2 kHz, limited by the shaker controller. The same conditions were also simulated, but for a frequency ranging from 100 Hz to 50 kHz. The test results are depicted in Figure 4.14.

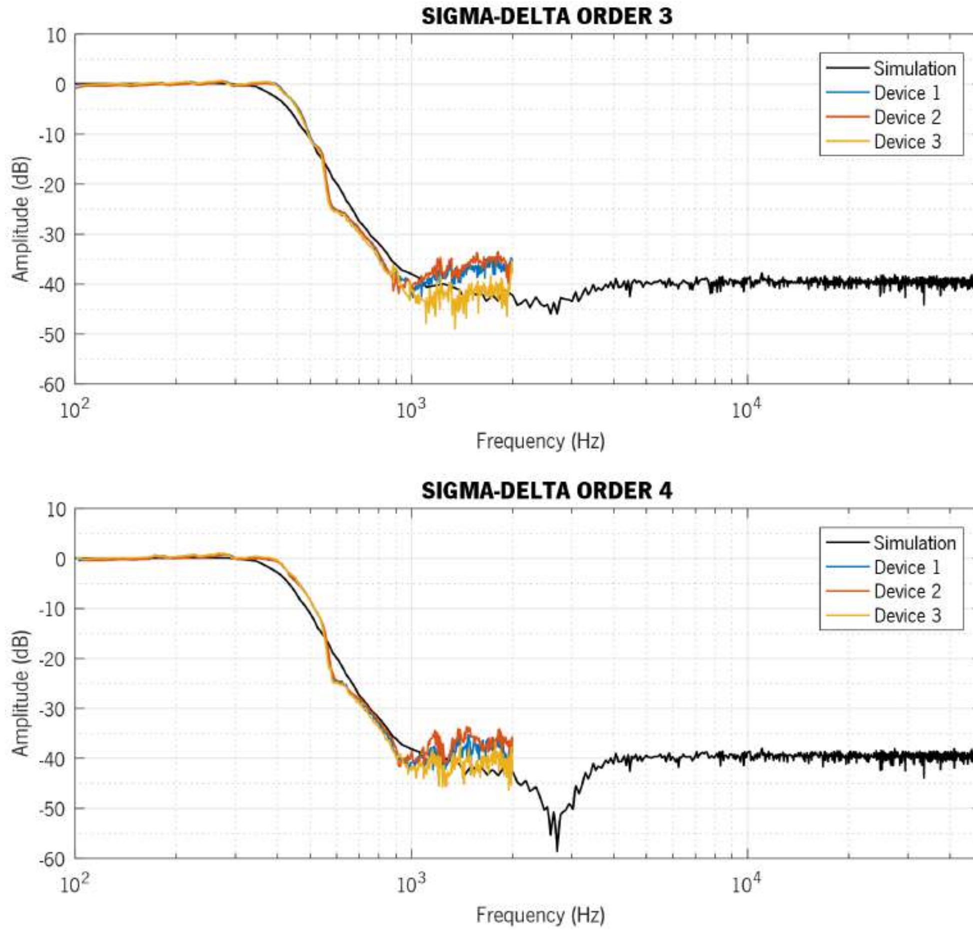

Figure 4.14: Experimental and simulated results of the vibration robustness test.

The results show a stable operation until the 2 kHz frequency mark, highlighting the capability of the sigma-delta modulator to cope with external accelerations. The simulation results are in accordance with the experimental data, and show a stable operation until 50 kHz, demonstrating the suitability of the device for automotive applications.

4.3. Low-noise optimization

Taking advantage of the flexibility and configurability of the implemented accelerometer system, the loop-gains were re-tuned in order to optimize the sensor to reach the lowest possible noise figure. The re-tuning process consisted of an experimental gain sweep, which aimed to optimize the noise figure of the accelerometer, without considering other performance characteristics. The loop-gains were adjusted to $k_{f3} = 27$, $k_3 = 0.3$, $k_{f4} = 87$, and $k_4 = 0.1$, while the phase compensator parameters remained the same. For this reason, the third and fourth-order modulators experiments were repeated for all three devices, and the measured Allan deviation is presented in Figure 4.15.

The results show a noise reduction for all devices, and once again, third and fourth-order modulators show approximately the same output. The best noise figure achieved was 123 μg/√Hz for device number 2, using a closed-loop third-order electromechanical sigma-delta modulator. Regarding the other performance characteristics of the accelerometer, all remained approximately the same, with the exception of measurement range, which decreased from ±5 g to approximately ±1.5 g.

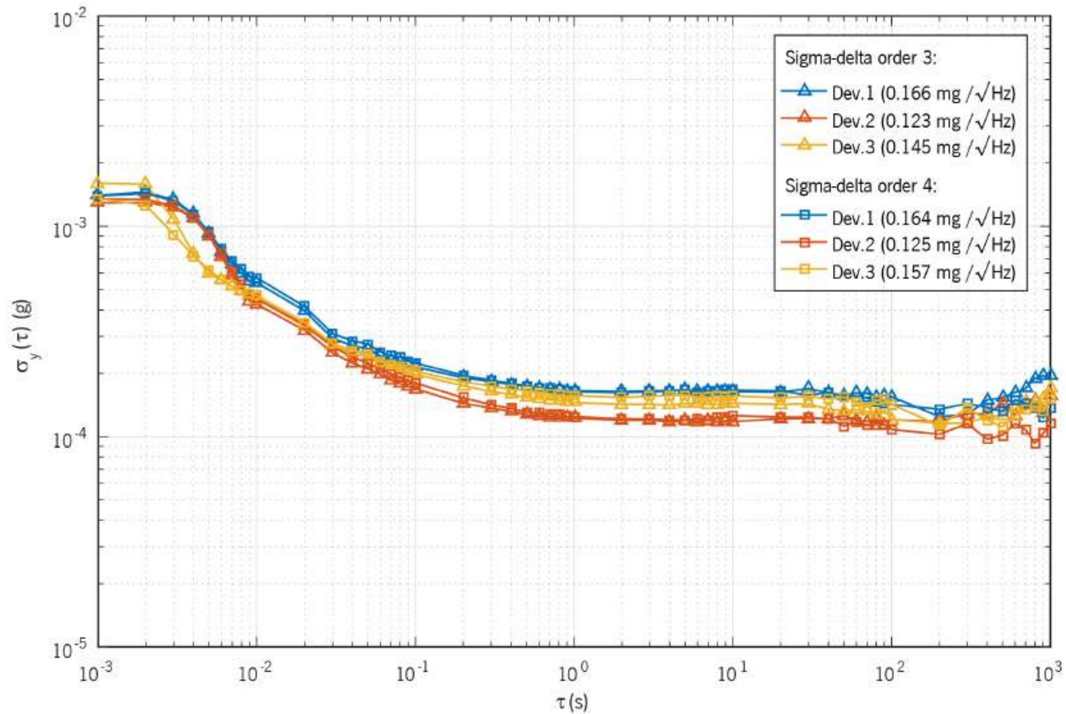

Figure 4.15: Allan deviation measurements for the low-noise optimization.

4.3.1. Long-term stability

To evaluate the long-term stability of the proposed system, the output signal was measured for 24 hours, on a low noise environment, with the device kept at approximately 0 g. This test was performed only for device number 2, configure in closed-loop as a third-order modulator, since it yields similar results as fourth-order without increasing the complexity of the system. In Figure 4.16, the obtained data is presented, showing the continuous plot of the acquired signal and the respective Allan deviation measurements.

The acquired data presents a standard deviation of 3.2 mg, while the Allan deviation measurements demonstrate that the bias instability of the accelerometer system is below 156 μg. Both results are valid for the 24 hours period of acquisition.

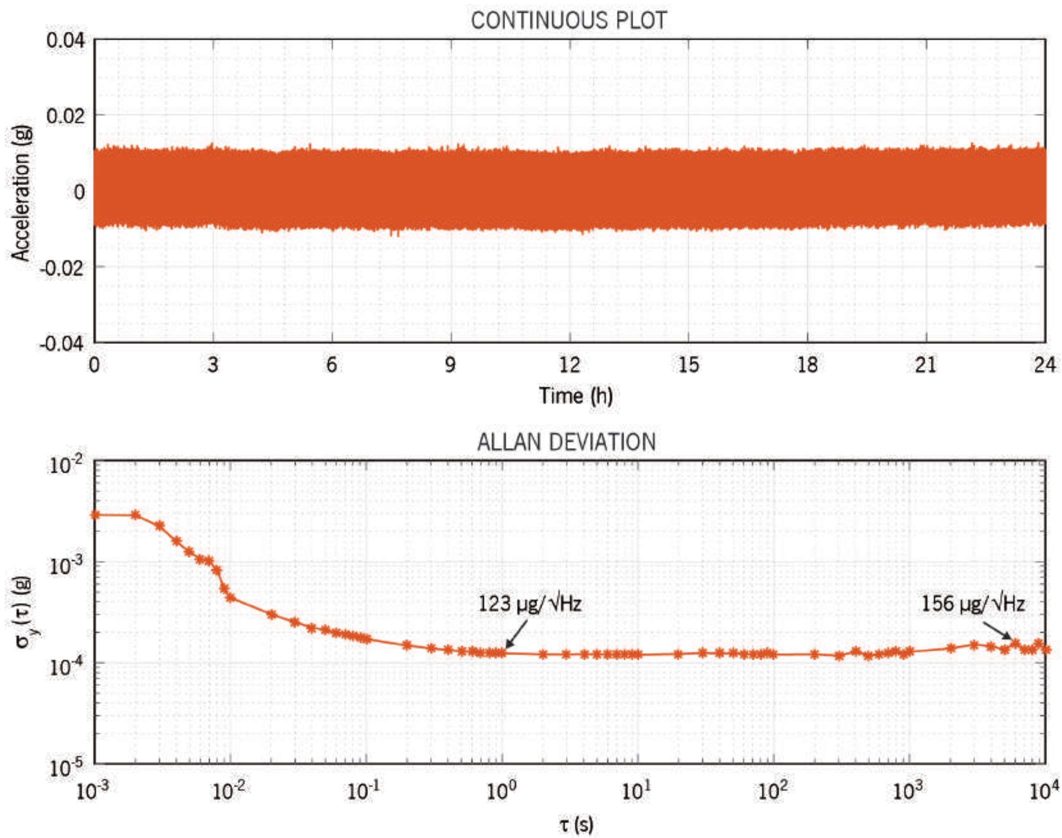

Figure 4.16: Long-term measurement results.

4.4. Conclusions

In this chapter, an in-depth characterization of the developed accelerometer system was presented. Several experimental tests were performed, and the results compared with simulation values obtained from the simulation model. The first experimental test was designed to obtain the mechanical characterization of three MEMS elements. The devices tested have parameters (resonant frequency, quality factor, and pull-in voltage) within 5% of the desired design parameters. Additionally, for the resonant frequency and pull-in voltage, the variation between devices is inferior to 0.3 %, suggesting very small microfabrication process tolerances.

The complete accelerometer system was assessed, including the MEMS sensor element, readout and actuation analog circuitry, and a FPGA with application software and digital hardware IPs. The sensitivity of the accelerometer system increased by a factor of over 900000, when switching from open-loop to closed-loop operation, and the simulation model was able to reproduce this behavior with an error of 7.4 %. The nonlinearity of the system was also experimentally measured, and 0.66 % was the worst case measured, which is well below the required 1 %. However, with manual alignment of the experimental setup, the nonlinearity was decreased to 0.2 %.

Arguably, one of the most important characteristics of an accelerometer is the noise figure. This characteristic was determined using Allan deviation measurements for all three fabricated devices and all system configurations: open-loop and 2nd-order, 3rd-order, and 4th-order modulators in closed-loop. The electromechanical sigma-delta modulator was able to reduce the approximately 7.3 mg/√Hz of the open-loop accelerometer, to approximately 600 μg/√Hz using a second-order modulator and to approximately 190 μg/√Hz using third and fourth-order modulators. As theoretically expected, the higher modulation orders yield lower noise in the signal bandwidth. Moreover, the simulation model was able to accurately predict the behavior of the system, although some limitations were found due to the simplified readout analog circuit model implementation.

The effects of the temperature were also studied, and once more, the closed-loop configuration improved the achieved results. The measured temperature coefficient presents a linear behavior, and a compensation mechanism was proposed, significantly reducing these effects. Furthermore, it was successfully demonstrated that, due to the differential MEMS readout design, and due to the use of a closed-loop approach, the sensitivity of the devices is not affected by temperature.

The frequency response of the accelerometer was evaluated, and a 400 Hz bandwidth was experimentally measured for a measurement range up to ±5 g. The vibration robustness of the device was also assessed for accelerations in the range of ±2 g. It was experimentally demonstrated that the device is stable to frequencies up to 2kHz, while the simulations show a stable behavior for frequencies below 50 kHz.

Finally, a low noise optimization was performed, achieving a noise figure of 123 μg/√Hz for device number 2, using a third-order modulator in a closed-loop configuration. This result was achieved without compromising any of the other performance parameters, with the exception of the measurement range, which decreased from ±5 g to approximately ±1.5 g. Moreover, the signal output of device number 2 was acquired for a period of 24 hours in the same configuration, demonstrating the long term stability of the developed system. A bias instability of less than 200 μg was obtain using Allan deviation on the measurements.

References

[4.1] N. Brito *et al.*, “Digital Platform for Wafer-Level MEMS Testing and Characterization Using Electrical Response,” *Sensors*, vol. 16, no. 9, p. 1553, Sep. 2016, doi: 10.3390/s16091553.

[4.2] National Instruments, “NI-DAQ USB-6363 Specifications.” 2018.

[4.3] Thorlabs, “PRMTZ8 Motorized Precision Rotation Stage User Guide.” 2018.

[4.4] Brüel & Kjær, “Permanent magnet shaker LDS V406,” 2020. [Online]. Available: https://www.bksv.com/en/products/shakers-and-exciters/LDS-shaker-systems/permanent-magnet-shakers/V406. [Accessed: 14-Mar-2020].

[4.5] Brüel & Kjær, “Comet USB vibration control system.” 2011.

[4.6] Brüel & Kjær, “Product Data: CCLD Accelerometers with TEDS Type 4533-B, 4533-B-001, 4533-B-002, and 4533-B-004 and Type 4534-B, 4534-B-001, 4534-B-002, and 4534-B-004.” 2013.

[4.7] R. Wilcock and M. Kraft, “Genetic Algorithm for the Design of Electro-Mechanical Sigma Delta Modulator MEMS Sensors,” *Sensors*, vol. 11, no. 12, pp. 9217–9232, Sep. 2011, doi: 10.3390/s111009217.

[4.8] P. Sherman, “Allan variance,” 2013. [4.Online]. Available: http://home.engineering.iastate.edu/~shermanp/AERE432/lectures/Rate Gyros/Allan variance.pdf.

[4.9] STMicroelectronics, “Noise analysis and identification in MEMS sensors, Allan, Time, Hadamard, Overlapping, Modified, Total variance.” 2016.

5. Conclusions and future work

In this thesis, the development and assessment of a vacuum encapsulated MEMS accelerometer using sigma-delta modulation was presented. The behavior of the MEMS element was analyzed, and a capacitive parallel-plate device was designed and microfabrcated. Moreover, the advantages of this approach were explained. The mechanical sensor was fabricated using Bosch's standard surface micromachining process, enabling integration with other sensors in the same die. To read the output signal and electrostatically actuate the device, required for the electromechanical sigma-delta modulation technique, these circuits were implemented in a PCB, using commercially available ICs and an in-house developed capacitance to voltage converter ASIC, providing system integration. The sigma-delta modulator loop was digitally implemented in an FPGA, aiming for flexibility and allowing the configurability of the loop architecture and respective gains in run time. A comprehensive characterization of the accelerometer was performed, assessing the fabrication parameters of the mechanical sensor and the performance of the developed accelerometer. The experimental results were also compared with the simulation values, validating the behavior of the system.

In this chapter, the main conclusions and contributions of this thesis are presented. Additionally, based on the acquired knowledge, proposals for future work are presented, aiming to improve the performance of the system and overcome the actual limitations.

5.1. Conclusions

The main conclusions to be drawn from the presented work were divided as follows:

1. **Design and modeling of the MEMS sensor:** A capacitive MEMS accelerometer was designed, consisting of a proof-mass suspended by two mechanical springs, with sensing and actuation electrodes in parallel-plate configuration. When the device is subjected to external accelerations, the proof-mass will move, and the resultant displacement can be sensed through the capacitance change in the electrodes.

   Due to the small dimensions required for the sensing element, the maximum proof-mass value is quite limited, as well as the achievable spring constant. Simulations based on finite element analysis were performed to ensure the proper behavior of the sensor, and to guarantee that the mechanical spring is compliant on the sensing axis while being sufficiently rigid on the other.

2. **Simulation model:** A comprehensive simulation model of the entire system was designed, including the MEMS element, the readout circuit, the phase compensator, the high-order loop, the decimation filter, and the one-bit DAC. The model was implemented in Simulink and it proved capable of accurately predict the behavior of the system regarding sensitivity, nonlinearity, noise figure, and frequency response.

3. **Readout and actuation circuits:** A PCB containing the readout and actuation circuits was designed and developed. The readout circuit uses an in-house capacitance to voltage converter ASIC and a commercially available ADC, providing a digital representation of the output signal of the MEMS sensor. The actuation circuit, implemented as a one-bit DAC, uses a commercially available voltage reference and analog switches, enabling the electrostatic force feedback. This way, no specialized laboratory equipment is required, providing a higher system integration. Moreover, the implemented circuitry can be migrated into an ASIC, since the utilized voltage levels are easily realized using CMOS technology.

4. **Sigma-delta modulation loop:** The closed-loop architecture of the system was digitally implemented in an FPGA, making available a second, third, and fourth-order electromechanical sigma-delta modulators. The modulation order and all high-order gains can be configured in run time, enabling reconfigurability of the system and improving its flexibility. Additional filtering blocks were also digitally implemented, aiming to improve the performance of the system.

5. **Performance of the accelerometer:** The designed accelerometer was fabricated, and three devices were characterized and compared.

    a. **Mechanical characterization:** The resonant frequency, quality factor, and pull-in voltage of the devices were experimentally measured, and they were within 5 % of the design parameters. Additionally, for the resonant frequency and pull-in voltage, the variation between devices was inferior to 0.3 %, which suggests small fabrication process tolerances.

    b. **Sensitivity:** The sensitivity of the sensor was measured for open-loop operation and second, third, and fourth-order modulation, showing an increase of over 900000 times. This highlights the performance benefits of the selected closed-loop technique.

    c. **Nonlinearity:** The achieved nonlinearity of the system was 0.66 % for the worst case scenario, complying with the desired 1 %. Moreover, with the manual alignment of the measurement setup, a nonlinearity of 0.2 % was achieved.

    d. **Noise figure:** Allan deviation measurements were made to assess the noise figure of the accelerometer. For the standard measurement range of at least ±5 g, the electromechanical sigma-delta modulator was able to reduce the approximately 7.3 mg/√Hz noise figure of the open-loop accelerometer, to approximately 190 µg/√Hz using third and fourth-order modulators. Additionally, the offset stability was also improved, from approximately 2 mg in open-loop, to about 200 µg for closed-loop.

       A noise optimization was also made, achieving a minimum noise figure of 123 µg/√Hz for a measurement range of ± 1.5 g, using third and fourth-order sigma-delta modulation. The offset stability was also improved to 156 µg, using the same modulation orders.

    e. **Cross-axis sensitivity:** The cross-axis sensitivity of the accelerometer was evaluated for two devices using second, third, and fourth-order sigma-delta modulators. The obtained results indicate a cross-axis sensitivity inferior to 0.4 %.

    f. **Temperature dependency:** The complete accelerometer system was put inside a temperature test chamber in order to evaluate its temperature dependency. Regarding the temperature coefficient, the tested accelerometers show a linear behavior that

decreases substantially from open-loop to closed-loop operation. Additionally, a common temperature compensation mechanism was proposed, which decreases the sensor response over temperature. Moreover, the susceptibility of the system's sensitivity to temperature was also assessed, and no correlation was found.

g. **Frequency response:** The dynamic response of the system was evaluated for a sinusoidal acceleration with ±5 g of amplitude. The obtained results show that the accelerometer is stable under such stimuli and a bandwidth of 400 Hz was experimentally measured.

h. **Vibration robustness:** The vibration robustness of the device was assessed for accelerations up to ±2 g, as desired in the automotive industry. It was experimentally demonstrated that the accelerometer has a stable operation to frequencies up to 2 kHz, while the simulations show a stable behavior for frequencies up tp 50 kHz.

Table 5.1: Comparison of the research objectives with the achieved performance.

Parameter	Research objective	Achieved
Encapsulation pressure	140 Pa	140 Pa
Core size	≤ 400 μm ×400 μm	364 μm ×400 μm
Voltage level	≤ 3.3 V	3.3 V
Temperature range	[-40, +125] °C	[+27, +70] °C measured
Offset stability in the temperature range	≤ 20 mg	≤ 257 mg (no compensation) ≤ 91 mg (common compensation) ≈ 0 (individual compensation)
Measurement range	≥ ±5 g	≥ ±5 g
Bandwidth	≥ 400 Hz	400 Hz
Noise level	100 μg/√Hz	190 μg/√Hz (123 μg/√Hz with optimization)
Nonlinearity	≤ 1 %	≤ 0.66 % (≤ 0.2 % with alignment)
Vibration robustness	400 Hz to 50 kHz	400 Hz to 2 kHz measured 400 Hz to 50 kHz simulated

When comparing the achieved performance with the objectives of the thesis (Table 5.1), it is clear that the majority of the research objectives were successfully achieved. Nonetheless, one of the objectives was not completely fulfilled, namely the noise level. The best noise level figure achieved was 123 μg/√Hz, which is close, but still superior than the desired 100 μg/√Hz. However, suggestions to improve this figure of merit are provided in the future work section. Additionally, the complete temperature range was not measured. Nevertheless, with the use of automotive grade electronic components, the desired temperature range is obtainable. Regarding the stability of the offset within the temperature range, the device with the worst temperature coefficient (with a third-order modulator) presents the following performance: 257 mg when no temperature compensation is applied, 91 mg when applying the same correction factor for all devices, and the temperature effects are virtually eliminated when applying the correct temperature coefficient for each individual device. The remaining performance characteristics were fully achieved.

6. **Comparison to the state-of-the-art:** To compare the obtained results with the state-of-the-art found in the literature, two figures of merit (FOM) are proposed, relating the achieved noise level with the bandwidth and sensor size (Table 5.2). These characteristics were chosen since device size and bandwidth are closely related to the noise level. On the one hand, a device with a large proof-mass intrinsically has lower thermal-mechanical Brownian noise, improving its overall noise performance. Additionally, with a large footprint sensor, larger capacitances are easier to achieve, improving the device sensitivity and consequently, the signal-to-noise ratio. On the other hand, a lower bandwidth signal allows for more restricted filtering and higher integration times, which also leads to the realization of lower noise levels.

   The proposed FOMs (expression (6.1) and (6.2)) multiply the noise level achieved by the device size (either volume of the proof-mass for FOM1 or mass of the proof-mass for FOM2) and divide the result by the achieved bandwidth. Since bigger size and lower bandwidth realize lower noise, a smaller result (in both FOM) translates to better relative performance. According to both figures of merit, the performance of the presented accelerometer stands out from the ones found in the literature, while using a less complex third-order modulator.

$$FOM\,1 = \frac{Volume \times NoiseFigure}{Bandwidth} \tag{6.1}$$

$$FOM\,2 = \frac{Mass \times NoiseFigure}{Bandwidth} \tag{6.2}$$

Table 5.2: Comparison of this work to the state-of-the-art.

Work	Proof-mass	Noise figure (μg/√Hz)	Bandwidth (Hz)	Dynamic range (g)	EMΣΔM order	FOM1 (mm^3.ng/Hz$^{1.5}$)	FOM2 (nKg.μg/Hz$^{1.5}$)
Henrion et al. (1990) [5.1]	1630 μg 0.5 mm^3	10	200	0.1	2nd	25	81.5
Chen et al. (2014) [5.2]	1620 μg 1.4 mm^3	1.2	500	± 6.0	6th	3.36	3.89
Wang et al. (2018) [5.3]	14300 μg -	0.2	300	± 1.5	5th	-	9.53
Li et al. (2018) [5.4]	620 μg -	0.48	300	± 1.0	6th	-	0.99
Colibrys S.A [5.5]–[5.7]	- 1.5 mm^3	1.7	300	15	5th	8.5	-
This work	2.83 μg 0.0028 mm^3	173 123	400	± 5.0 ± 1.5	3rd	1.21 0.86	1.22 0.87

Additionally, when comparing the accelerometer developed in this thesis with the ones presented on the literature, the size difference is colossal. In Table 5.3 are presented the sizes of the proof-mass of each research work, as well as the normalized values. It is shown that the smaller proof-mass of the literature is 219 times bigger than the proof-mass of the proposed accelerometer. Additionally, the device with the best noise performance has a proof-mass 5053 times bigger. The implemented accelerometer system was able to achieve a performance level suitable for the proposed application, while keeping a small footprint. This size reduction will enable great cost reductions since several more devices can be fabricated in the same silicon area.

Table 5.3: Device size comparison.

Work	Proof-mass size	Proof-mass size normalized
Henrion et al. (1990) [5.1]	1630 μg 0.5 mm^3	576 179
Chen et al. (2014) [5.2]	1620 μg 1.4 mm^3	572 500
Wang et al. (2018) [5.3]	14300 μg -	5053 -
Li et al. (2018) [5.4]	620 μg -	219 -
Colibrys S.A [5.5]–[5.7]	- 1.5 mm^3	- 536
This work	2.83 μg 0.0028 mm^3	1 1

5.2. Future work

Considering the acquired know-how through the development of this thesis, as well as the obtained results, some improvement opportunities were identified, aiming to increase the performance of the presented accelerometer.

Due to the timing frame of the research work and timing requirements related to the fabrication of the MEMS device, the design of the mechanical sensor was one of the first tasks performed. At the time, the developed simulation model of the electromechanical sigma-delta modulator was significantly less refined, which lead the design of a MEMS accelerometer not 100 % optimized for sigma-delta modulation. Using the more comprehensive simulation model currently available, the mechanical sensor can be further optimized regarding two parameters: the ratio between the length of the plates of the capacitor and the area of the proof-mass, and the ratio between the number of sensing electrodes and actuation electrodes.

Considering the desired footprint of 400×400 μm^2 of the device core, and the device layout, composed by one central proof-mass with capacitor electrodes on both sides, the tradeoff between the length of the capacitor electrodes and the area of the proof-mass arises. On the one hand, large capacitors are desired, since they result in larger capacitance changes, improving the sensitivity of the device. On the other hand, a large proof-mass is also advantageous since it results in bigger displacements, also improving the sensitivity of the device. However, in order to realize big capacitances, the proof-mass must be reduced, and increasing the proof-mass results in smaller capacitor electrodes. A balance between these two factors must be achieved, and using the now more comprehensive simulation model could result in a better tradeoff.

Also limited by the desired device footprint, there is a limited number of possible capacitor electrodes. Considering that these electrodes must be divided into sensing and actuation electrodes, another tradeoff arises. On the one hand, the number of sensing electrodes needs to be maximized, realizing bigger sensing capacitances and increasing the sensitivity. On the other hand, the number of actuation electrodes must also be maximized, which increases the electrostatic force applied to the MEMS element. This results in improved dynamic range and linearity of the sensor. Once again, the optimization of this tradeoff based on the improved simulation model could be advantageous and result in better sensor performance.

With the objective of further increasing the performance of the accelerometer, mainly by reducing noise, it is possible to increase the integration level of the system. To achieve this, an ASIC including all the

implemented circuitry can be designed, improving the signal integrity and reducing the electrical noise. Additionally, the capacitance to voltage converter can also be optimized for the capacitance values of the designed MEMS element.

Another integration step to reduce the noise of the system is related to the packaging. Currently, the MEMS element is wire bonded to one package, the capacitance to voltage converter is wire bonded to another package, and the remaining electronics are soldered to the PCB. Several precautions were taken to reduce the parasitic capacitances, mainly between the MEMS sensor and the capacitance to voltage converter. However, packaging the MEMS element and the previously described ASIC into one single chip carrier will result in a drastic reduction of parasitic capacitances, further improving the signal quality and reducing the achievable noise.

Considering that the previously described measures were able to reduce the electrical noise in such a way that it does not limit the noise figure of the accelerometer system, new sigma-delta modulator architectures can be further investigated. The simplest way of increasing the noise shaping and realize better performance is to increase the modulation order. Thus, more single order loops can be cascaded, implementing higher-order modulators. Additionally, different loop architectures can also be explored, including feedforward and different feedback paths, aiming to further improve the noise shaping without increasing modulation order.

References

[5.1] W. Henrion, L. DiSanza, M. Ip, S. Terry, and H. Jerman, "Wide dynamic range direct digital accelerometer," in *IEEE 4th Technical Digest. on Solid-State Sensor and Actuator Workshop*, 1990, pp. 153–157, doi: 10.1109/SOLSEN.1990.109842.

[5.2] F. Chen, W. Yuan, H. Chang, I. Zeimpekis, and M. Kraft, "Low noise vacuum MEMS closed-loop accelerometer using sixth-order multi-feedback loops and local resonator sigma delta modulator," in *IEEE 27th International Conference on Micro Electro Mechanical Systems (MEMS)*, 2014, pp. 761–764, doi: 10.1109/MEMSYS.2014.6765752.

[5.3] Y. H. Wang, L. Yin, D. L. Chen, L. Li, and X. W. Liu, "A method to reduce harmonic distortion of MEMS accelerometer," *Mod. Phys. Lett. B*, vol. 32, no. 21, 2018, doi: 10.1142/S0217984918502469.

[5.4] X. Li, J. Hu, and X. Liu, "A High-Performance Digital Interface Circuit for a High-Q Micro-Electromechanical System Accelerometer," *Micromachines*, vol. 9, no. 12, 2018, doi: 10.3390/mi9120675.

[5.5] P. Zwahlen, A.-M. Nguyen, Y. Dong, F. Rudolf, M. Pastre, and H. Schmid, "Navigation grade MEMS accelerometer," in *IEEE 23rd International Conference on Micro Electro Mechanical Systems (MEMS)*, 2010, pp. 631–634, doi: 10.1109/MEMSYS.2010.5442327.

[5.6] Y. Dong, P. Zwahlen, A. M. Nguyen, R. Frosio, and F. Rudolf, "Ultra-high precision MEMS accelerometer," in *16th International Solid-State Sensors, Actuators and Microsystems Conference*, 2011, pp. 695–698, doi: 10.1109/TRANSDUCERS.2011.5969218.

[5.7] P. Zwahlen *et al.*, "Breakthrough in high performance inertial navigation grade Sigma-Delta MEMS accelerometer," in *IEEE/ION Position, Location and Navigation Symposium*, 2012, pp. 15–19, doi: 10.1109/PLANS.2012.6236858.

Annex A: Analog circuit schematics

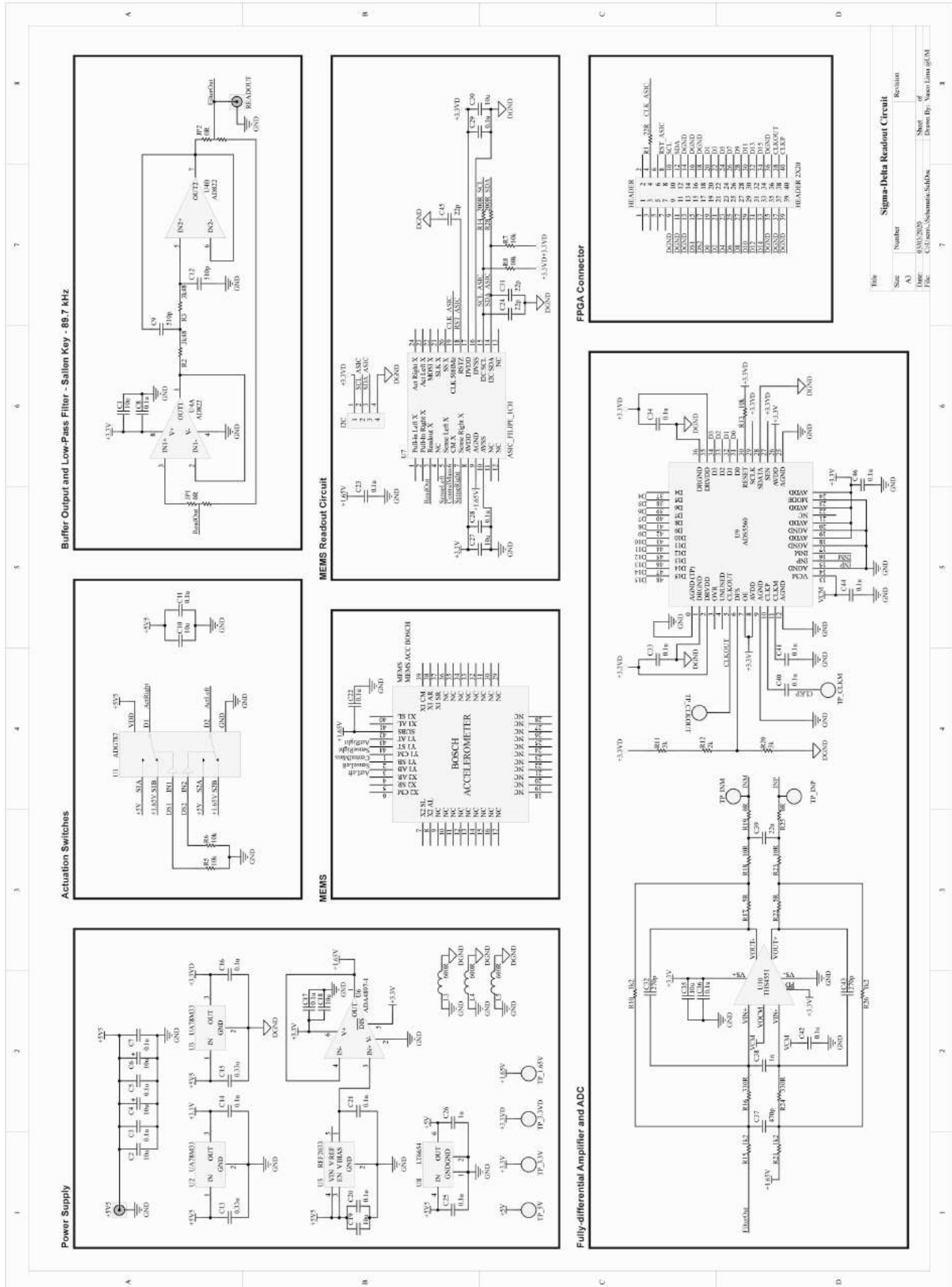

Annex B: Analog circuit PCB layers

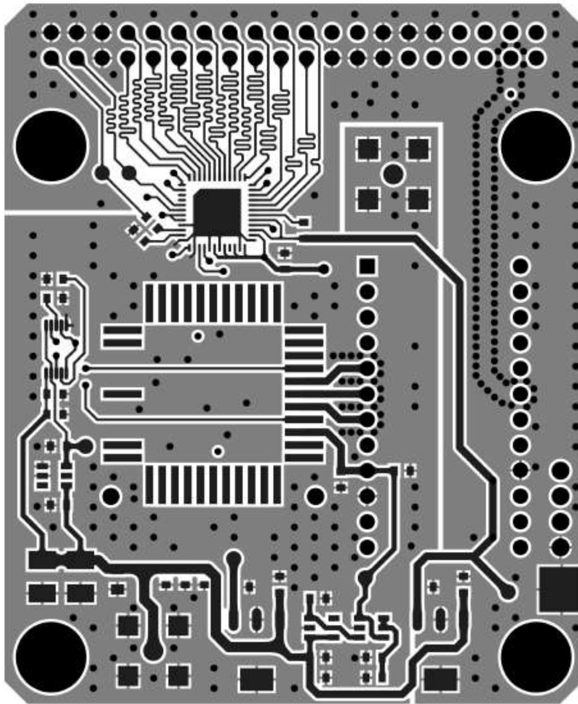

Top layer

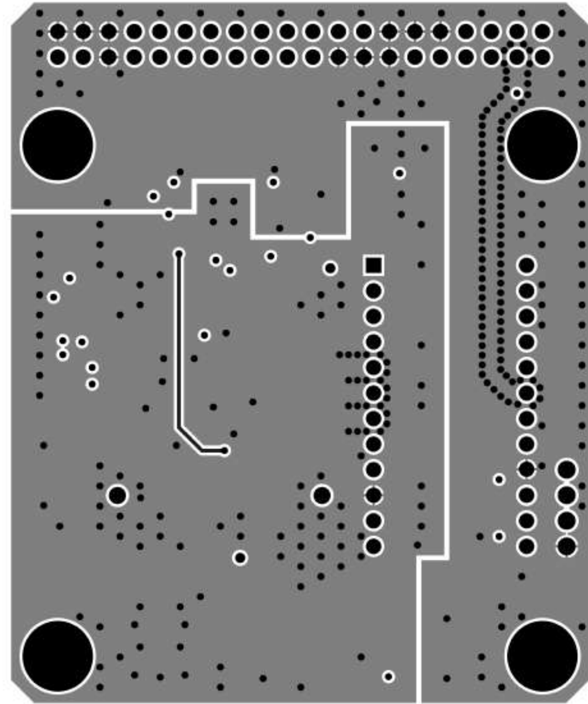

Mid layer 1

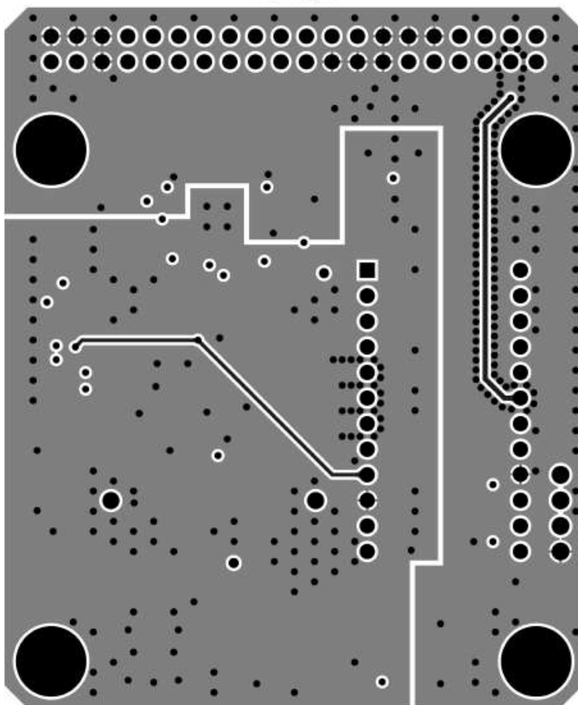

Mid layer 2

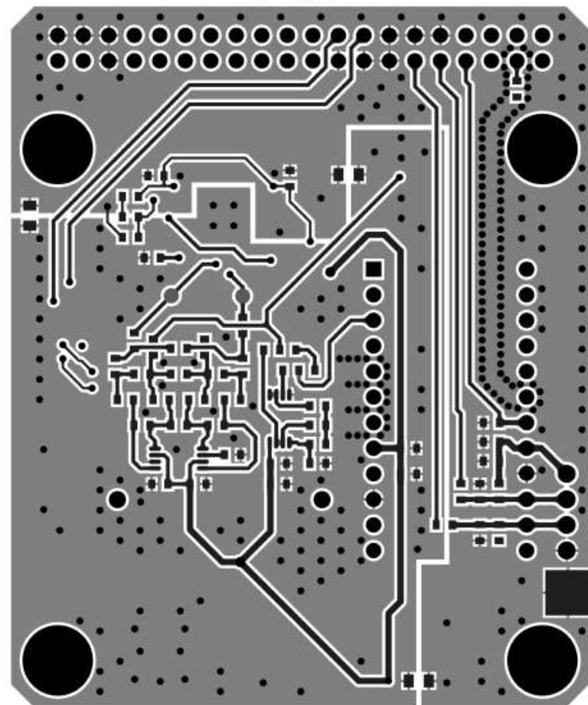

Bottom layer

Annex C: FPGA block diagram

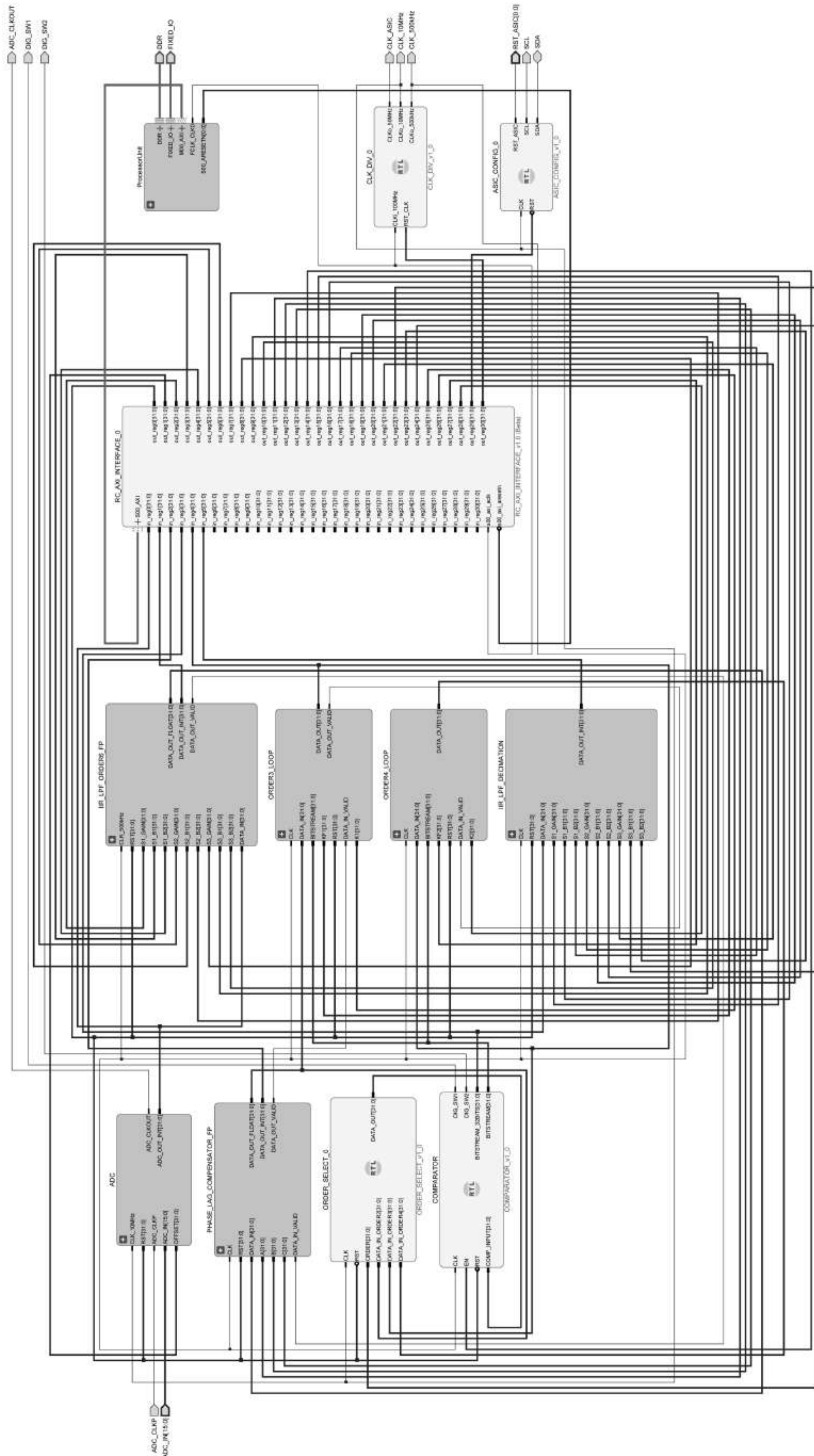

Annex D: IIR block diagram

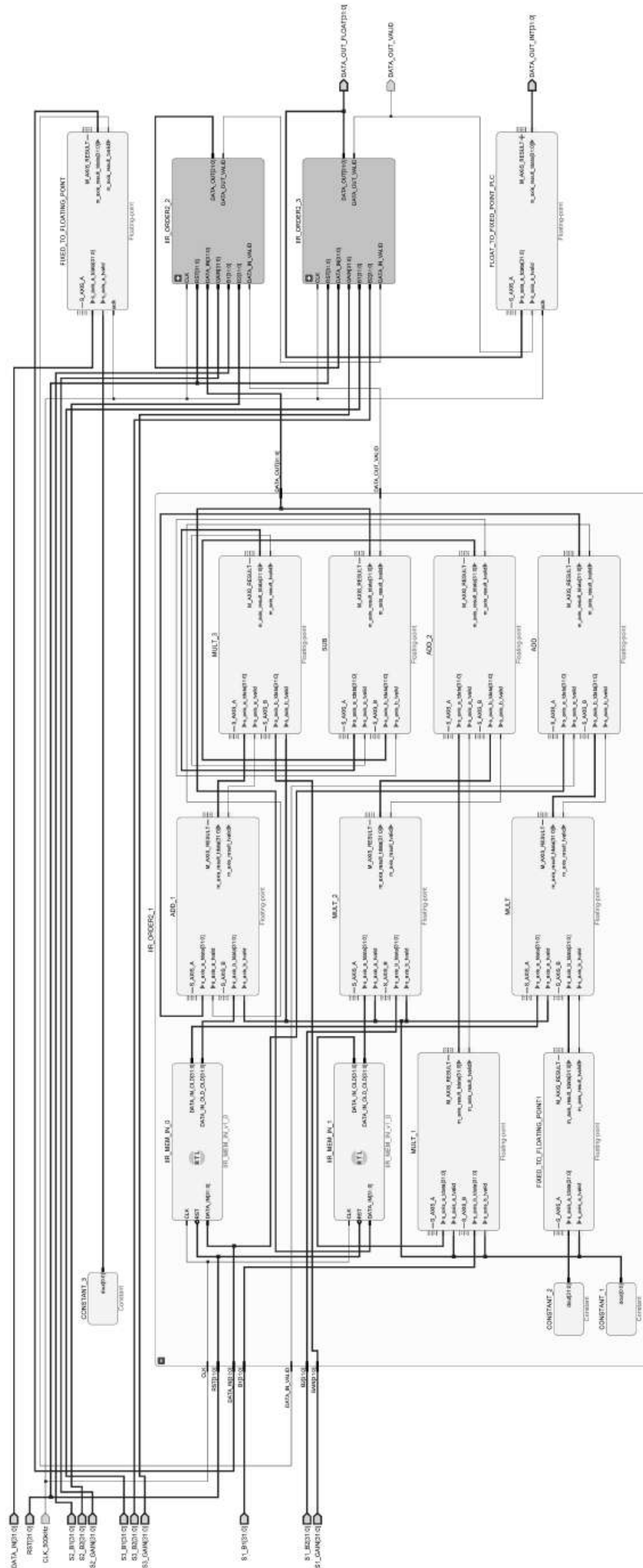

Annex E: Phase compensator block diagram

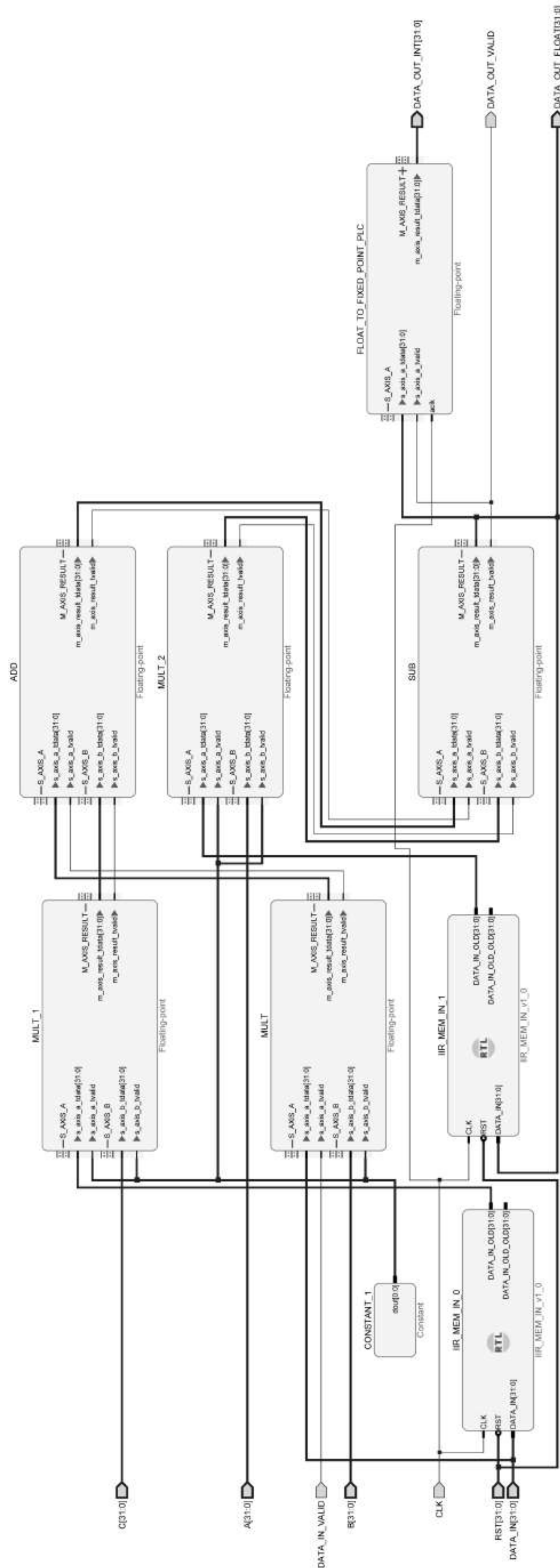

Annex F: High-order loop block diagram

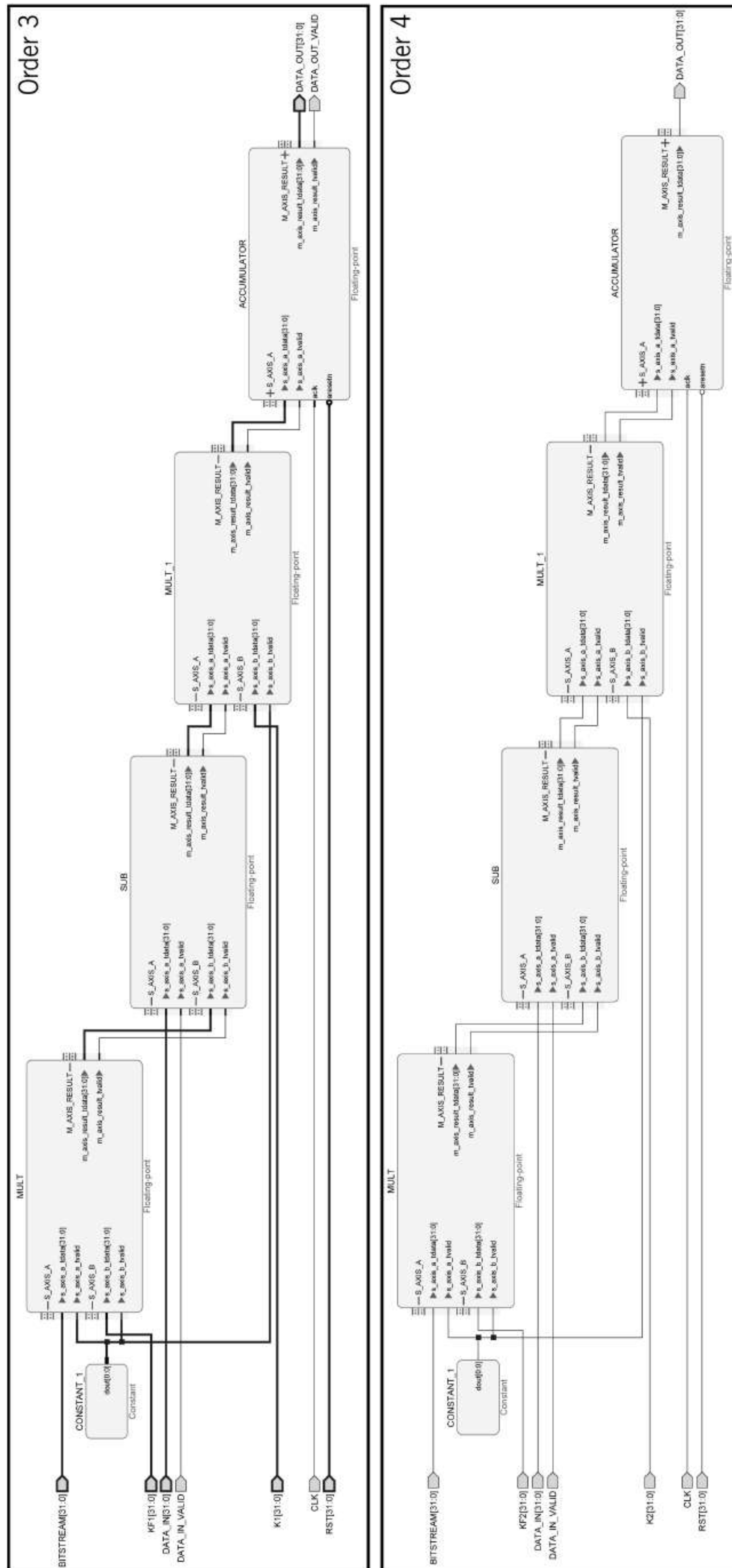

LIST OF PUBLICATIONS

Journal publications

1. **V. Lima**, N. Brito, J. Cabral, J. Monteiro, J. Gaspar, and L. A. Rocha, “Digital platform for Sigma-Delta accelerometer assessment and test,” Microsystem Technologies, vol. 24, no. 5, pp. 2265–2276, May 2018. http://doi.org/10.1007/s00542-018-3736-2

2. E. Esteves Moreira, **V. Lima**, F. S. Alves, J. Cabral, J. Gaspar, and L. A. Rocha, “Full-gap tracking system for parallel plate electrostatic actuators using closed-loop control,” Sensors and Actuators A: Physical, vol. 244, pp. 174–183, Jun. 2016. http://doi.org/10.1016/j.sna.2016.04.002

Conference proceedings

1. **V. Lima**, J. Cabral, B. Kuhlmann, J. Gaspar, and L. A. Rocha, “Small-size MEMS Accelerometer Encapsulated in Vacuum Using Sigma-Delta Modulation,” IEEE International Symposium on Inertial Sensors and Systems (INERTIAL), 2020. https://doi.org/10.1109/INERTIAL48129.2020.9090096

2. **V. Lima**, J. Cabral, B. Kuhlmann, and L. A. Rocha, “Low-Pressure Small MEMS Accelerometer Using Sigma-Delta Modulation,” Proceedings, vol. 2, no. 13, p. 1029, Nov. 2018. http://doi.org/10.3390/proceedings2131029

3. **V. Lima**, N. Brito, F. S. Alves, J. Cabral, J. Gaspar, and L. A. L. A. Rocha, “Performance Comparison of Sigma-delta Modulator Architectures for MEMS Accelerometers Using a Fully-Digital Approach,” Procedia Engineering, vol. 168, no. C, pp. 814–817, 2016. http://doi.org/10.1016/j.proeng.2016.11.280

4. N. Brito, **V. Lima**, F.S. Alves, J. Cabral, J. Gaspar, J. Monteiro, and L. A. Rocha, “Embedded Platform for Generic High-order Sigma-delta Accelerometers Testing,” Procedia Engineering, vol. 168, pp. 954–957, 2016. http://doi.org/10.1016/j.proeng.2016.11.314

Conference presentations

1. **V. Lima**, N. Brito, J. Cabral, J. Monteiro, J. Gaspar, and L. A. Rocha, “Short-Keynote: Digital platform for Sigma-Delta accelerometer assessment and test,” Jornadas sobre sistemas reconfiguráveis (REC), 2018, Guimarães, Portugal. (Oral presentation)

ABOUT THE AUTHOR

Vasco António Lourenço Lima was born in Ponte de Lima, Portugal in 1989. He received his M.Sc. degree in Electronic Engineering from University of Minho, Guimarães, Portugal, in 2013. After graduation he was a researcher in collaborative projects between the University of Minho, Guimarães, Portugal, and Bosch Car Multimedia, Braga, Portugal. In 2016 he started pursuing his Ph.D. degree in Advanced Engineering Systems for Industry, in the same university where he graduated, in partnership with Bosch Car Multimedia, Braga, Portugal, and Bosch Automotive Electronics, Reutlingen, Germany. In the past year he has been a visitor researcher at the International Iberian Nanotechnology Laboratory, Braga, Portugal, and an Invited Assistant Professor at the Polytechnic Institute of Cávado and Ave, Braga, Portugal. His research focus has been on the design, instrumentation and characterization of MEMS sensor and actuators.